UNDERSTANDING THE ELECTRON STORAGE CAPACITY OF

PYROGENIC BLACK CARBON: ORIGIN, REDOX REVERSIBILITY,

SPATIAL DISTRIBUTION, AND ENVIRONMENTAL APPLICATIONS

by

Danhui Xin

A dissertation submitted to the Faculty of the University of Delaware in partial fulfillment of the requirements for the degree of Doctor of Philosophy in Civil Engineering

Summer 2021

UNDERSTANDING THE ELECTRON STORAGE CAPACITY OF

PYROGENIC BLACK CARBON: ORIGIN, REDOX REVERSIBILITY,

SPATIAL DISTRIBUTION, AND ENVIRONMENTAL APPLICATIONS

by

Danhui Xin

Approved: _____
Jack A. Puleo, Ph.D.
Chair of the Department of Civil and Environmental Engineering

Approved: _____
Levi T. Thompson, Ph.D.
Dean of the College of Engineering

Approved: _____
Louis F. Rossi, Ph.D.
Vice Provost for Graduate and Professional Education and
Dean of the Graduate College

I certify that I have read this dissertation and that in my opinion it meets the academic and professional standard required by the University as a dissertation for the degree of Doctor of Philosophy.

Signed: _____

Pei C. Chiu, Ph.D.
Professor in charge of dissertation

I certify that I have read this dissertation and that in my opinion it meets the academic and professional standard required by the University as a dissertation for the degree of Doctor of Philosophy.

Signed: _____

Yu-Ping Chin, Ph.D.
Member of dissertation committee

I certify that I have read this dissertation and that in my opinion it meets the academic and professional standard required by the University as a dissertation for the degree of Doctor of Philosophy.

Signed: _____

Dominic M. Di Toro, Ph.D.
Member of dissertation committee

I certify that I have read this dissertation and that in my opinion it meets the academic and professional standard required by the University as a dissertation for the degree of Doctor of Philosophy.

Signed: _____

Paul T. Imhoff, Ph.D.
Member of dissertation committee

I certify that I have read this dissertation and that in my opinion it meets the academic and professional standard required by the University as a dissertation for the degree of Doctor of Philosophy.

Signed: _____

Andrew Wozniak, Ph.D.
Member of dissertation committee

ACKNOWLEDGMENTS

I have always thought that the journey of graduate school is my lonely fight through seemingly endless obstacles. Yes, it was! However, on reflection, it is no exaggeration to say my dissertation would not be the same, or not exist at all, without so many people's help. I am relieved that I have a chance to express my most sincere gratitude to people who paved the way for me.

I must thank my advisor, Professor Pei C. Chiu, for first seeing potential in me and then patiently guiding me all the way through my Ph.D. His extraordinary talent, sincere attitude to science, and endeavor to educate young minds have always been an inspiration to me. Thank you for working hard and being an academic role model for me. I am also grateful to the most supportive dissertation committee, Professors Yu-Ping Chin, Dominic M. Di Toro, Paul T. Imhoff, and Andrew Wozniak. I was absolutely fortunate to rely on your intellectual input and professional guidance.

Many thanks to my collaborators, Drs. Toufiq M. Reza and Nepu Saha, for providing me an opportunity to work on two publications together. The work I have done with you turned out to be the one I am most proud of during my Ph.D. My thanks also go to my coauthors, Minghan Xian, Thomas Barkley, and Jeffrey Hudson. What an enjoyable experience working with you!

At UD, I was privileged to be a DENIN fellow, one of the most exciting and rewarding experiences I had. Specifically, I would like to thank Jeanette Miller for always encouraging me and being there for support. I am also grateful to all DENIN

fellows. So many events we have run together, and every time, I felt we could do much greater things together.

I also want to thank Dr. Yuhan Yu, Michael Davison, and Christine Reoli, who played major roles in completing my Ph.D. Inside the lab, Dr. Yuhan Yu offered his help every time I felt helpless and hopeless. Your help was so timely and effective that I can't thank you enough. Outside the lab, Michael Davison and Christine Reoli were there all the time from the first day of my Ph.D., providing their support.

I spent at least half of my working hours in the lab, days and nights, so I am grateful to my supportive and cheerful lab mates: Minghan Xian, Steven Lobo II, Leslie Ope, Camila Babativa, and Julián Girón. You made my days.

I also want to say thank you to a list of people: Jimmy Murillo, Kevin Hickey, Paula Cardenas, Elijah Akanbi, Juan Camilo, Julián Girón, and Samia Rahman. You were my colleagues, pacesetters, friends, and family here. You are truly amazing human beings! All the laughs I shared with you remained as, at least a couple of, under-eye wrinkles in me, but it was totally worth it.

I am also thankful to my dear roommates and friends: Tingting, Weila, Wan-Chun, Inyoung, and Taozhu for supporting and entertaining me.

Finally, I would like to thank my mom, dad, my boyfriend Haoyi, and all other immediate families for their steady support and endless patience. Special thanks to my mom for raising me to be a healthy person through your unconditional love.

Many thanks to everyone I know and everything I've encountered in my life!

TABLE OF CONTENTS

LIST OF TABLES

LIST OF FIGURES

xvi

ABSTRACT

Plant-based black carbon is produced globally at a rate of >100 million tons per year through both natural and anthropogenic processes. Electron storage capacity (ESC) is a novel property of black carbon, which determines its capacity to store electrons and reversibly exchange electrons with chemical and microbial agents in its surroundings. Research in recent years has shown that the ESC of plant-based black carbon is considerable, on the order of a few mmol per gram. This suggests that black carbon, which is ubiquitous in soils and sediments, may represent an enormous but previously unrecognized electron reservoir, influencing biogeochemical processes in terrestrial and aquatic environments. In addition, the discovery and understanding of ESC may greatly expand the applications of biochar—a class of man-made black carbon that has received significant interest in recent years for its potential environmental benefits. This is because the ESC may enable biochar to serve as a reactive medium to support the redox transformation of contaminants in natural and engineered systems.

Despite the potential impact of black carbon on biogeochemistry and environmental remediation, prior work on its ESC is very limited. It was hence necessary to develop an improved understanding of the ESC. To this end, this dissertation presents an effort to understand the ESC of black carbon in terms of its origin, redox reversibility, spatial distribution, and environmental applications. Chemical methods were developed to quantify the ESC of black carbon, evaluate its redox reversibility, and characterize its spatial distribution. Based on a chemical redox

titration method with Ti(III) citrate and dissolved O_2, the ESC of plant-based black carbon ranged from 0.2−7 mmol/g, which was highly reversible over multiple redox cycles. Using a silver tagging method, a sizable fraction of ESC was shown to reside in the interior of black carbon particles, which explains partial microbial accessibility of the ESC and the pore diffusion-limited rate observed in the reactions involving the ESC of black carbon. Furthermore, by comparing the ESC of biopolymers and their corresponding chars, the origin of ESC was identified. The results show that the ESC of black carbon is not derived from its source biomass but created during pyrolysis, suggesting ESC is a common property of black carbon produced through pyrolysis of all lignocellulosic biomass. Finally, fully reduced (i.e., ESC-saturated) biochars were applied to abiotically transform insensitive munitions compounds, demonstrating the potential utility of biochar for removing organic pollutants through its ESC.

This dissertation represents a major step towards understanding the ESC of black carbon. Findings from this dissertation will help explain black carbon-mediated redox processes, lead to new remediation strategies, and shed light on the impacts of black carbon on the cycling of carbon and other elements. The methods developed in this dissertation will be essential tools for further investigation of the ESC of black carbon and evaluating its impacts.

Chapter 1

SIGNIFICANCE, SCOPE, AND STRUCTURE

As an integral part of the global carbon cycle, pyrogenic black carbon (hereafter referred to as black carbon) is produced through both natural and anthropogenic processes including wildfires, deforestation, and incomplete fossil fuel combustion. Each year, 117–389 million tons of black carbon is produced through biomass burning, representing 70–94% of total black carbon production [1]. The majority of black carbon produced from biomass burning (114–383 million tons) is incorporated into subsurface environments, which constitutes a soil stock of 200 trillion tons, contributing to 14% of total organic carbon in soils [1, 2].

Biochar is a class of man-made black carbon produced through pyrolysis of surplus biomass (wood chips, switchgrass, etc.) under oxygen-limited conditions. With the promise of addressing global challenges associated with food and climate, biochar has received widespread interest in recent years [3, 4]. In 2014, Klüpfel et al. [5] discovered that plant-derived biochar possesses a considerable electron storage capacity (ESC) (also known as electron exchange capacity (EEC)). The ESC determines the capacity of biochar to store electrons and reversibly exchange (accept/donate) electrons with chemical and microbial agents in its surroundings. Using mediated electrochemical analysis (MEA), the ESC of plant-derived biochar was as high as 2 mmol/g, which is on par with that of natural organic matter. Two years later, Saquing et al. [6] demonstrated that biochar can support acetate oxidation and nitrate reduction by *Geobacter metallireducens*, where biochar served as the sole

electron acceptor and donor, respectively. The microbially accessible ESC was determined to be 0.86 mmol e⁻/g by both acetate oxidation and nitrate reduction.

These prior findings support that other pyrogenic black carbon, which is produced through a similar process as for biochar, may also possess significant ESC. If this is the case, given the ubiquity in soils and sediments, black carbon may represent an enormous but previously unrecognized electron reservoir, influencing biogeochemical processes, including carbon sequestration, greenhouse gas production, and contaminant fate, in terrestrial and aquatic environments. In addition, the discovery and understanding of ESC may greatly expand environmental applications of biochar, where it can serve as not only a passive sorbent but a reactive medium that supports redox transformation of contaminants in natural and engineered systems.

Because scientists are just becoming aware of the ESC [5-7], there is very limited prior work. Therefore, it is necessary to develop an improved understanding of the ESC for assessing the role of black carbon in biogeochemistry and developing effective biochar-based remediation strategies. To this end, this dissertation aims at understanding the ESC of pyrogenic black carbon from its origin, redox reversibility, spatial distribution, and environmental implications. To achieve the goal, the dissertation will be guided by five key questions: (1) How can ESC be quantified? (2) Is ESC reversible? (3) Where is ESC spatially located in a black carbon particle? (4) What is the origin of ESC? (5) Can the ESC of biochar support contaminant transformation? These scientific questions will be sequentially answered in next Chapters 2–5.

In Chapter 2, the first two questions— (1) How can ESC be quantified? (2) Is ESC reversible? —are addressed. Chemical redox titration (CRT) methods are

developed to quantify the ESC of black carbon, which is then repeated over multiple redox cycles to assess the extent to which the ESC of black carbon is reversible. An accurate and reliable method for measuring the ESC is the prerequisite of investigating the property. CRT method is currently the only method that can quantify the ESC of porous black carbon in its entirety, which has been validated by comparing it to the existing MEA method and surveying more than 20 black carbon samples in this work and by others [8, 9]. The CRT method quantifies the electrons transferred between a black carbon sample and a redox titrant, i.e., a soluble, non-sorbing chemical reductant or oxidant, based on titrant consumption. For method development, using Soil Reef biochar (SRB) as a model black carbon, the results show that the consumption of Ti(III) citrate was proportional to the mass of DO-oxidized SRB used, resulting in an ESC of ca. 4 mmol/g for SRB. For the DO–Ti(III) citrate pair, the ESC obtained over three redox cycles was constant at ca. 3 mmol/g, demonstrating the ESC of SRB is highly reversible. Pore diffusion of Ti(III) citrate within biochar particles was determined to be the rate-limiting step, which controlled the timescale of redox equilibrium.

MEA is the other method, in fact, an established [5] and more widely used method [10-14], for measuring the ESC of black carbon. When the CRT and MEA methods are compared on the same SRB, the results show that (1) the ESC of biochar measured by MEA is particle size-dependent, whereas the ESC measured by CRT is not, and (2) ESC results obtained by MEA are likely underestimated as the method captured only a fraction of the ESC that is measurable by CRT. Given that ESC is a property of black carbon, the method should quantify the property in its entirety and yield a consistent and reproducible value that is independent of particle size.Therefore,

the CRT method is more suitable for measuring the ESC of black carbon and other porous materials. For method validation, the CRT method with DO and Ti(III) citrate was applied to survey more than 20 black carbon samples, including commercial biochar, lab-produced biochar, granular activated carbon, hydrochar, pyrolyzed hydrochar, chars generated from wildfire, and graphite. Except for hydrochar and graphene, all plant-based black carbon samples possessed significant and highly reversible ESC, ranging from 0.2−7 mmol/g.

In Chapter 3, the spatial distribution of the ESC on and inside a black carbon particle is imaged using electron microscopy. A method for tagging and visualizing the ESC on and within a black carbon particle is presented. The method consists of three steps: (1) A black carbon sample was first reduced (i.e., ESC-saturated) using dithionite (reduction potential E_h= −0.43 V vs. SHE at pH 6.4). (2) Ag^+ was then allowed to diffuse into the pores of reduced black carbon at a constant pH to react with the stored electrons, producing Ag^0 nanoparticles (nAg) *in situ* where ESC was located. (3) As ESC marker, nAg were visualized by electron microscopy to obtain the spatial distribution of ESC in intact and sectioned black carbon particles. For the model SRB, up to 2.5 mmol Ag^+ per gram biochar (corresponding to 62% of its ESC) was reduced to nAg. While abundant and dense nAg were observed on the biochar surface, ubiquitous and well-dispersed nAg were found in the interior of biochar. Based on electron microscopy images, we calculated an area density of 8.43×10^6 $Ag^0/\mu m^2$ on the surface and a volume density of 3.98×10^7 $Ag^0/\mu m^3$ in the interior. The calculation and visual confirmation of the significant ESC in the interior of SRB explain the slow, pore diffusion-limited reactions of SRB and the incomplete accessibility of its ESC to *G. metallireducens* in previous studies [6]. Conversely, the

higher nAg density at or near the surface than in the bulk of SRB is consistent with the rapid reactions at the beginning of CRT measurements.

In Chapter 4, the origin of the ESC of black carbon is identified. Studies have shown that ESC is common for biochars derived from plant biomass, but it is unclear which plant component(s) contributes to ESC. The ESC of biochar may originate from the source plant biomass if the biomass itself possesses ESC that can survive pyrolysis. Alternatively, ESC may be generated during pyrolysis. Identifying the origin of ESC is necessary to understand how ESC is controlled by biomass composition and/or pyrolysis conditions. Lignocellulosic biomass (i.e., plant-based biomass) is essentially composed of three biopolymers: cellulose, hemicellulose, and lignin, along with variable amounts of extractives and minerals [15]. One approach to determine the origin of black carbon ESC is to compare the ESC of the feedstocks, including three biopolymers and wood, and biochars prepared from these biopolymers, their mixture, and wood, through pyrolysis at 350–650 °C. The results show that, of the three biopolymers, lignin was the only biopolymer that possessed ESC, which was largely destroyed during pyrolysis at 350 °C. After pyrolysis at ≥450 °C, the three biopolymers, their mixture, and wood all yielded biochars that possessed a highly reversible ESC of 1–2 mmol/g. This indicates that pyrolysis created reversible ESC of biochar from lignocellulosic biomass, presumably by converting oxygen-containing moieties of the biopolymers into (hydro)quinones in biochar. A comparison between wood and biopolymer biochars suggests that the biopolymers contributed additively to ESC creation. Furthermore, the fact that the ESC of biochar is created during pyrolysis suggests that black carbon that is produced from lignocellulosic biomass thermally through wildfires and deforestation may also possess ESC.

Chapter 5 demonstrates the application of biochar for transforming organic pollutants through its ESC, in which munitions constituents (MCs) including 3-nitro-1,2,4-triazol-5-one (NTO), nitroguanidine (NQ), 2,4-dinitroanisole (DNAN), hexahydro-1,3,5-trinitro-1,3,5-triazinane (RDX) were used as model pollutants. It was hypothesized that biochar can be a rechargeable electron donor to support abiotic transformations of MCs through its ESC. To test the hypothesis, parallel experiments were performed using the dithionite-reduced (ESC-saturated) biochars for the abiotic reduction of MCs and the DO-oxidized (ESC-vacant) biochars for non-reactive sorption control. The results show that, while NTO removed by the oxidized biochar was minimal, NTO removed by the reduced biochar was significant and 3-amino-1,2,4-triazol-5-one (ATO) was formed concomitantly, confirming that NTO was abiotically reduced to ATO by biochar through its ESC. A complete mass balance and electron balance revealed that (1) the amount of ATO formed by the reduced biochar was relatively constant at 85–100 μmol/g in the pH range of 6–10, (2) the fraction of ESC reactive toward NTO was ca. 30% of that toward ferricyanide, and (3) the ESC was rechargeable for NTO reduction over three redox cycles. When the reactivity of the reduced biochar was tested for other MCs including NQ, DNAN, and RDX, the reduced biochar was able to abiotically reduce DNAN and RDX but not NQ. These results not only verify the hypothesis but also demonstrate that biochar can be an effective material for removing MCs through concurrent reduction and sorption. The results also suggest biochar-based remediation strategies may be developed for DoD sites and the potential of biochar for transforming pollutants that are redox-labile.

Finally, in Chapter 6, the directions for future research on investigating the ESC of black carbon and assessing its environmental impacts are discussed. Research

that would advance the understanding of black carbon ESC includes (1) evaluating the potential of biochar to sequester redox-labile metals and radionuclides through ESC, (2) unraveling the E_h distribution of ESC, (3) surveying black carbon as a global electron reservoir, and (4) investigating the role of ESC in microbial processes.

The dissertation will be a contribution to our understanding of ESC of pyrogenic black carbon. Findings from this dissertation will help explain black carbon-mediated redox processes, provide the basis for designing biochar ESC-based remediation systems, and shed light on the impact of black carbon on the cycling of carbon and other elements. The methods developed in this dissertation will be essential tools for further investigation of the ESC of black carbon and evaluating its impacts.

Chapter 2

**CHEMICAL REDOX TITRATION METHODS FOR QUANTIFYING THE
ELECTRON STORAGE CAPACITY AND ITS REVERSIBILITY OF
PYROGENIC BLACK CARBON**

1.1   Introduction

Once considered a nonreactive geosorbent [16, 17], black carbon is now recognized as a spectrum of reactive carbonaceous materials, such as graphite [7, 18-21], activated carbon [20, 22], soot [21], and biochar [6, 10, 23-26], which can mediate abiotic and microbial redox transformation of environmental contaminants. [21, 27-32] It is imperative that we understand the redox properties of black carbon and the mechanism through which it mediates redox reactions. This is not only for understanding and predicting the environmental fate of pollutants, but also for developing effective remediation strategies, e.g., using engineered black carbon such as biochar to enhance contaminant (bio)degradation in treatment systems.

At least two mechanisms have been shown to be potentially involved in black carbon-mediated redox transformation, one through conduction, and the other through storage of electrons. [31] The first mechanism was shown in the early 2000s [7, 18, 21, 30] and is important for graphitic carbons such as graphite and soot. This

mechanism may also operate for black carbon formed at below graphitization temperature (e.g., 500 °C) but still contains nanoscale graphene domains. [32] The second mechanism was demonstrated more recently by Klüepfel et al. [5] through mediated electrochemical analysis (MEA). The authors showed that wood- and grass-derived biochars possessed up to 2 mmol/g of electron accepting and donating capacities (EAC and EDC). These two mechanisms differ fundamentally: In the conduction mechanism, oxidation of a reductant and reduction of an adsorbed contaminant occurs concomitantly via electron conduction through graphitic domains in black carbon; in the storage mechanism, in contrast, black carbon is reduced or oxidized first and the stored electrons or electron vacancies, respectively, are subsequently accessed for redox transformation. [6]

The electron storage capacity (ESC) is a property of black carbon that determines its capacity to store electrons and reversibly exchange (donate or accept) electrons with chemical and microbial agents in its surroundings via redox reactions. The finding that the same amount of electrons (ca. 0.86 mmol/g) were deposited to, and later retrieved from, Soil Reef biochar (SRB) by *Geobacter metallireducens* GS-15 for the oxidation of acetate and reduction of nitrate, respectively, suggests that black carbon such as biochar may possess a certain ESC that can be accessed reversibly by microorganisms. [6] However, the total ESC of the biochar is unknown, and thus it is unclear what fraction of its ESC was microbially accessible. This information is critical for estimating the capacity of black carbon, as an electron acceptor and donor, to support microbial oxidation and reduction of contaminants, respectively. Therefore, it is necessary to develop robust methods to measure the ESC

of black carbon in order to determine its redox properties and behavior, and to predict its capacity to support contaminant degradation.

MEA is the established method for EAC/EDC analysis. As a sensitive and elegant technique, MEA quantifies the electrons transferred between a sample and the working electrode based on the current resulting from the electron transfer carried out by a redox mediator [33]. MEA utilizes redox mediators of suitable potentials to facilitate electron transfer between a working electrode and a small (<1 mg) redox-active sample, such as humic acid [34-36], iron mineral [33, 37-40], and biochar [5, 11-14, 41]. However, biochar made in large quantities for field applications can be heterogeneous, and methods that can handle larger sample sizes are necessary to obtain a representative ESC. Instead of electrical current, electron transfer may be quantified by light absorption, since many oxidants and reductants, including many mediators used in MEA [33], can be quantified spectrophotometrically when they undergo oxidation or reduction. This may provide a direct and simple, albeit less sensitive, [42] alternative to assess the EAC and EDC (and hence ESC) of black carbon.

In theory, ESC is the sum of EAC and EDC if the capacity is fully reversible. The ESC of black carbon is presumably distributed over a range of redox potential, similar to that for humic acids (ca. –0.35 to 0.15 V vs SHE at pH 7.0). [34] Therefore, EAC and EDC can both vary depending on the redox state of biochar, but their sum, i.e., ESC, should be constant for a given redox potential range if all functional groups involved react reversibly. However, this has not been demonstrated, as no EAC and EDC measurements were conducted over multiple redox cycles on the same samples. In addition, without bringing black carbon to a reference state before each analysis [5,

43], any measured EAC/EDC would reflect the redox state and electron content of the sample at the time of measurement and would vary with storage, exposure to air, and moisture, etc. Finally, the timescale to achieve redox equilibrium for biochar, and hence the accuracy of EAC/EDC measurement, is unknown, as the rate-limiting step has not been identified.

This Chapter is designed to (1) develop new chemical redox titration (CRT) methods to measure the ESC of black carbon and compare it with the existing MEA method, (2) evaluate the reversibility of the ESC, (3) determine the rate-limiting step and timescale for ESC measurement, and (4) estimate the microbially accessible fraction of the ESC. We chose a wood-derived SRB as model black carbon because it has been field-tested to improve nitrate removal from stormwater [44] and its microbially accessible ESC has been determined. For the CRT method, we employed pairs of chemical reductants (Ti(III) citrate and dithionite) and oxidants (ferricyanide and dissolved O_2 (DO)) of different potentials to assess ESC and its reversibility. These chemicals were selected because they are sufficiently reducing [45, 46] or oxidizing [47, 48] relative to the reported potentials for humic acids. [34] Except for O_2, these chemicals can be quantified by spectrophotometric and/or potential measurement and are anionic and thus would sorb minimally to SRB. For method comparison, we measured the ESC of SRB with different particle sizes using the CRT method with Ti(III) citrate and DO as titrants and the MEA method with ABTS and diquat as mediators. For method validation, the CRT method with Ti(III) citrate and DO was applied to 20 black carbon samples, including commercial biochar, lab-produced biochar, granular activated carbon, hydrochar, pyrolyzed hydrochar, chars

generated from wildfire, and graphite. Finally, we compared our ESC data against ESC reported in the literature.

1.2   Materials and Methods

1.2.1   Chemicals

Titanium(III) chloride (20% w/v in 2 N HCl), titanium(IV) chloride (0.09M in 20% HCl), sodium citrate (99%), 1,4-benzoquinone (99%), potassium ferricyanide (99+%), potassium ferrocyanide (98.5%), monobasic (98+%) and dibasic (≥99%) sodium phosphate and sodium 2,6-dichlorophenol-indophenol (DCPIP, 98%) were acquired from ACROS Organics (Morris Plains, NJ). Sodium dithionite (>85%) was purchased from Alfa Aesar (Haverhill, MA). Potassium chloride (KCl, >99.0%) was obtained from Fisher Scientific (Pittsburgh, PA). 2,2-Azino-bis(3-ethylbenzothiazoline-6-sulfonic acid) diammonium salt (ABTS, 98%) and 1,1'-ethylene-2,2'-bipyridinium dibromide monohydrate (diquat, 95%) were purchased from Sigma-Aldrich (St. Louis, MO). All chemicals were used as received.

1.2.2   Biochar

SRB (The Biochar Company, PA) was produced through pyrolysis of Southern Yellow wood chips at 550 °C. This commercial biochar was used in field-scale bioretention cells and infiltration strips in Delaware and Virginia to enhance nitrate removal from stormwater [44, 49]. In addition, SRB has been shown to possess a microbially accessible ESC. We used SRB from the same batch as that used by Saquing et al. to allow direct comparison [6]. Some properties of SRB are listed in Table 2.1, along with the content of acid-extractable redox-active metals (Fe, Mn, Co, and Ni). SRB samples of two size fractions (<100 and 250–500 μm) were sieved, air-

oxidized in aerated deionized water for 72 h, vacuum-filtered, and dried before use. The <100 μm size fraction was used for most experiments because of its shorter equilibration times. Moisture contents of SRB samples were determined by drying at 105 °C. All reported EAC, EDC, and ESC values are based on the dry weight.

Table 2.1Physical properties and redox-active metal contents of SRB

	Value	Unit	Method
Porosity	0.57^a	—	mercury intrusion porosimetry
Skeletal Density	1.816^b	g/cm^3	
BET Surface Area	158 ± 3^c	m^2/g	N_2 adsorption
Fe	2348.0 ± 120^c	mg/kg	1:500 w/v in 2% HNO_3, 24 h
Mn	473.2 ± 14^c	mg/kg	1:500 w/v in 2% HNO_3, 24 h
Co	0.8 ± 0.2^c	mg/kg	1:500 w/v in 2% HNO_3, 24 h
Ni	2.1 ± 0.3^c	mg/kg	1:500 w/v in 2% HNO_3, 24 h

[a] Value from Yi [50].
[b] Value from Saquing et al. [6].
[c] Measured in this work. Acid-extractable metals are reported as mean ± one standard deviation.

1.2.3   EAC and EDC measurements.

All EAC and EDC were measured in an anaerobic glove box (2.0±0.5% H_2 in N_2, P_{O_2}<25 ppm, Coy, MI). Ti(III) citrate and ferricyanide were quantified directly by absorbance, whereas the electron content of the dithionite solution was measured indirectly with DCPIP (described below). The wavelengths and extinction coefficients used to quantify Ti(III), ferricyanide, DCPIP, and benzoquinone are given in Table 2.2. Absorbance was measured with a Vernier LabQuest 2 UV-vis spectrophotometer (Vernier, OR).

Table 2.2   Wavelengths and extinction coefficients of the oxidants and reductants

	Extinction coefficient $(M^{-1}cm^{-1})^a$	Wavelength (nm)	R^2
1,4-Benzoquinone	32.4 ± 0.7	400 nm	0.999
Ti(III) citrate	91.5 ± 3	400 nm	0.996
DCPIP	$18,600 \pm 660$	603 nm	0.996
$[Fe(III)(CN)_6]^{3-}$	1160 ± 27	420 nm	0.999

[a] Measured in this work and reported as mean ± one standard deviation.

1.2.4   EAC measurement using Ti(III) citrate

Because we observed variations in Ti(III) concentration among different commercial sources and between batches of the same product, Ti(III) citrate concentration in each stock solution was first standardized by benzoquinone of high purity (Figure 2.1).
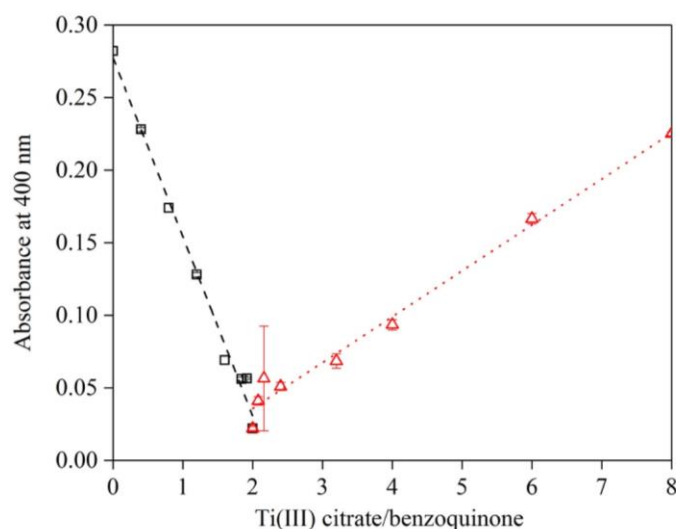
Figure 2.1   Calibration of Ti(III) in 100 mM citrate buffer using 1,4-benzoquinone at pH 6.4. Note that the two regression lines intercept at approximately 2, the stoichiometric ratio, where the solution absorbance was at a minimum, and the Ti(III) concentration could be determined accordingly. Error bars represent one standard deviation.

Each EAC measurement was performed in duplicates, and reactors without SRB were used as controls for all experiments. A known mass of pre-oxidized SRB was added to 0.50 L of 10 mM Ti(III) in 100 mM sodium citrate at pH 6.4±0.2, the third pK_a of citric acid. The anionic citrate buffer (50 mM each being doubly and triply negatively charged) was used to prevent the sorption of Ti(III) citrate. Preliminary tests showed that aqueous Ti(III) concentration was constant for 24 h in the presence of dithionite-reduced SRB. In addition, the total Ti concentration in the solution remained constant as Ti(III) citrate was consumed following the addition of oxidized SRB (Figure 2.2). This confirms that neither Ti(III) nor Ti(IV) sorbed to biochar during EAC measurement, and hence Ti(III) consumption could be attributed to oxidation by SRB. Reactors were placed on an orbital shaker at 100 rpm. At

different elapsed times, 6.6-mL samples were collected and passed through a 0.22-μm

PVDF syringe filter for Ti(III) analysis.
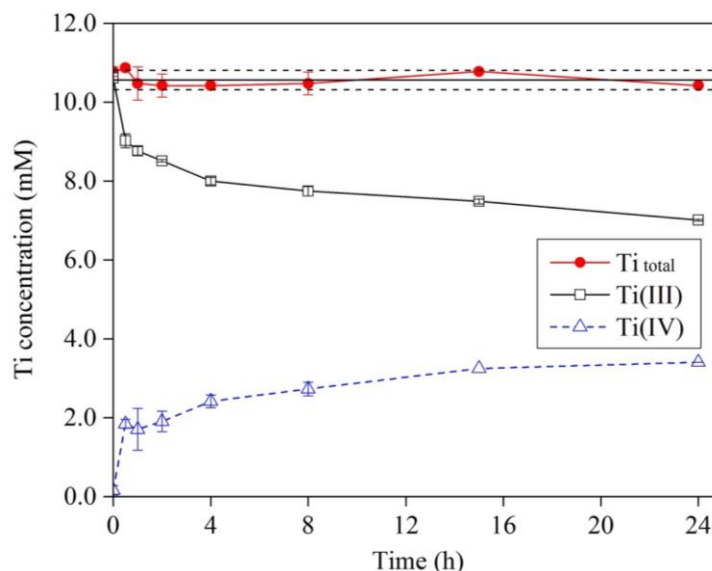
Figure 2.2   Titanium mass balance during reduction of air-oxidized SRB (0.49 g) in
500 mL of Ti(III) citrate. Total titanium (Ti(III) + Ti(IV)) and Ti(III)
citrate concentrations were measured by ICP-MS and UV-vis
spectrophotometry, respectively. The horizontal solid and dashed lines
represent the average total Ti concentration $\pm$ one standard deviation
(10.56 ± 0.25 mM). Ti(IV) concentrations were obtained from
differences between total Ti and Ti(III) concentrations. Error bars
represent one standard deviation.

The electrons transferred to SRB from Ti(III) was calculated based on electron

balance using Equation 2.1.

$$\text{e}^- \text{ transferred (mmol)} = C_1 \times V_1 - C_n \times (V_1 - nV_i) - \sum_{i=1}^{n}(C_i \times V_i) \tag{2.1}$$

where C_1 and V_1 are the initial Ti(III) concentration and solution volume, respectively,

n is the total number of samples, C_n is the final Ti(III) concentration at equilibrium,

and C_i and V_i are the Ti(III) concentration and volume of the ith sample, respectively. That is, the amount of electrons accepted by SRB was taken to be the difference between the initial and final electron contents of the Ti(III) citrate solution minus the electrons contained in all the samples withdrawn, which collectively accounted for <10% of the initial electron content of the Ti(III) solution. SRB was taken to be at equilibrium with the solution when the change in EAC calculated from Equation 2.1 between two consecutive samples was <3%.

1.2.5 EDC measurement using ferricyanide

Each EDC measurement using ferricyanide was performed in duplicates, and reactors without SRB were included as controls. The EDC of Ti(III)-reduced SRB was measured in 0.25 L of 10 mM ferricyanide in 20 mM phosphate buffer (pH 7.0±0.4). Reactors were shaken at 100 rpm, and 2.5-mL samples were taken at different times, filtered, and 10-fold diluted for ferricyanide measurement. The amount of electrons transferred from Ti(III)-reduced SRB (to Fe(III)) was calculated using Equation 2.1. The anionic phosphate buffer was used to prevent ferricyanide adsorption. Preliminary tests showed that ferricyanide was stable in solution and did not sorb to air-oxidized SRB for 24 h, thus precluding sorption as a loss mechanism.

1.2.6 EAC measurement using dithionite/DCPIP

We measured the EAC of SRB using dithionite as a reductant for two reasons. First, dithionite is a strong and one of the most widely investigated reductants for environmental applications. [51, 52] Second, dithionite was used to reduce SRB which could then provide 0.87 mmol e$^-$/g for microbial nitrate reduction. [6] We developed a method using DCPIP to quantify the electron content of the dithionite solution, instead

of measuring dithionite itself. This was necessary because (1) the purity of commercial dithionite is low (~85%), (2) dithionite is unstable in solution, and dissociates to sulfoxyl radical ($\cdot SO_2^-$) through homolysis and disproportionates to thiosulfate and sulfite [52], and (3) unlike Ti(III) and Fe(III), which transfers one electron, the number of electrons transferred per dithionite (where S redox state = +3) depends on the products formed; e.g., thiosulfate (+2), sulfite (+4), or sulfate (+6). Dithionite and its daughter reductants can be oxidized (Figure 2.3) by DCPIP (Standard reduction potential, E_h^o = +0.25 V at pH 7.0), [33] which can be measured spectrophotometrically. As SRB was reduced in dithionite solution, solution electron content was measured based on changes in DCPIP absorbance at 603 nm over time, and the EAC of SRB was calculated from the initial and final (i.e., equilibrium) solution electron contents.
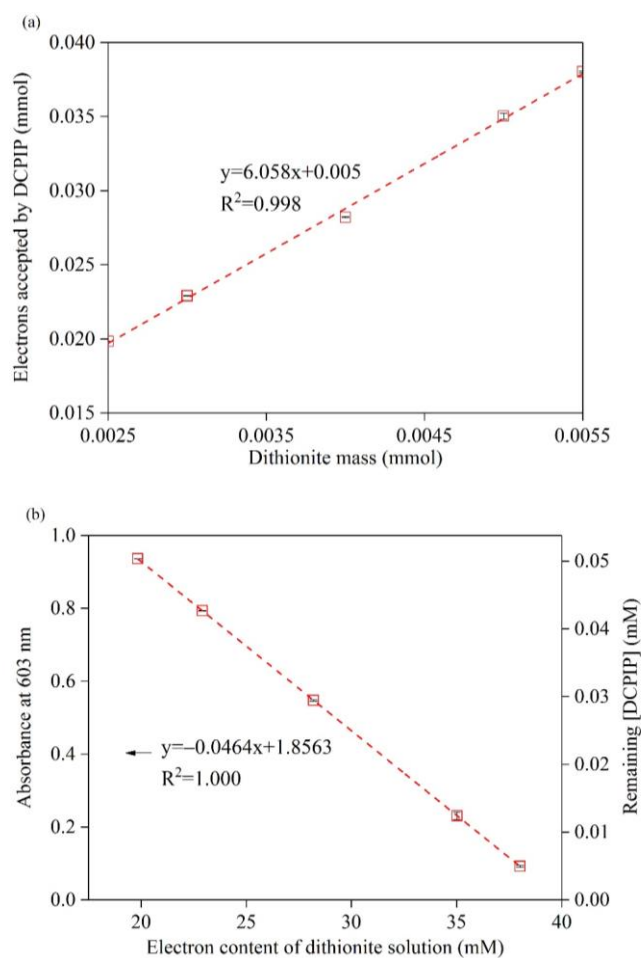
Figure 2.3   (a) Titration of dithionite samples using DCPIP. The observed
DCPIP:dithionite mole ratio was 3:1. The slope indicates ca. 6 moles of
electrons were transferred to DCPIP from each mole of dithionite. (b)
Calibration curve for the electron content of dithionite solution in 50 mM
citrate buffer (pH 6.4) based on DCPIP absorbance at 603 nm. Error bars
represent one standard deviation.

Each EAC measurement was performed in triplicates, and reactors without

SRB were included as controls. A known mass of air-oxidized SRB was added to 0.20

L of 5 mM dithionite solution in 50 mM citrate buffer (pH 6.4±0.2). Reactors were

shaken at 100 rpm and at different times 1-mL samples were removed, filtered, and

analyzed with DCPIP. Briefly, 2 mL of 10 mM DCPIP was mixed with 1-mL dithionite sample, diluted to 10 mL, allowed to react for 1 h, and 20-fold diluted for DCPIP analysis. EAC was calculated using Equation 2.1.

1.2.7 ESC Reversibility Tests

Reversibility of ESC was evaluated over repeated cycles using Ti(III) citrate or dithionite as a reductant and ferricyanide or DO as an oxidant. The methods for EAC and EDC measurements were the same as those described above. All samples were processed in an anaerobic glove box except when they were to be air-oxidized next. SRB oxidation by DO was performed in 200 mL continuously aerated deionized water for 72 h. After each oxidation or reduction step, the SRB sample was collected on a glass microfiber filter, rinsed thoroughly with deionized water, vacuum-dried, and transferred to a desiccator for 24 h. This resulted in the moisture content of $2.2\pm1.5\%$. Samples were weighed and divided into triplicates for the next EAC or EDC analysis. SRB mass loss (<10% between consecutive measurements) was accounted for in all EAC/EDC calculations.

1.2.8 Redox Potential Measurement

Redox potentials of Ti(III) citrate, dithionite, and ferricyanide solutions were measured using an Orion ORP electrode (Fisher Scientific, Pittsburgh, PA) and an Oakton pH 11 series pH/mV/°C meter (Oakton Instruments, Vernon Hills, IL). The ORP electrode combines a Pt working electrode and an Ag/AgCl reference electrode and was calibrated periodically against the Zobell solution (YSI, OH). All reported potentials are vs. SHE.

1.2.9 Comparison of CRT and MEA

SRB sifted to the size range of 250−500 µm was used directly or after grinding to <53 µm. The CRT method with Ti(III) citrate and DO developed in this Chapter, and the MEA method with ABTS and diquat as mediators were used for quantifying the ESC of SRB.

MEA experiments were performed in an anaerobic glove box (Plas Labs, Lansing, MI). The EDC and EAC were determined using mediated electrochemical oxidation and reduction (MEO and MER), respectively. We used ABTS (ABTS/ ABTS·+, E_h = +0.68 V vs. SHE) and diquat (diquat·+/diquat^{2+}, E_h = −0.36 V vs. SHE) as MEO and MER redox mediators, respectively. [34] A 40-mL glassy carbon cylinder (HTW, Thierhaupten, Germany) served as the working electrode as well as a reaction vessel. A separate coiled platinum wire was applied as the counter electrode (Bioanalytical Systems, West Lafayette, IN) housed within a porous glass frit (Ace Glass, Vineland, NJ). Electrochemical potentials were controlled by a potentiostat (DropSens µStat 400, Metrohm, Herisau, Switzerland) and controlled from outside the glovebox by a Bluetooth connection. Reduction potential (E_h) was measured against the Ag/AgCl reference electrode and reported against SHE. The glassy carbon cylinder and porous glass frit, containing 36 mL of 100 mM KCl and 100 mM phosphate buffer at pH 7, were equilibrated to a predetermined reduction potential (+0.61 V in MEO and −0.49 V in MER). To initiate the experiment, a 1-mL mediator (~10 mM ABTS or diquat^{2+}) was spiked into the cell and the oxidative or reductive current peaks were recorded. After a constant background current was established, 500 µL of 1 g/L DO-oxidized SRB suspensions (500 µg) were spiked into the cell in sequence, resulting in current peaks. Each sample was spiked at least twice and the average and range of results from duplicates were reported. The MEO and MER

current peaks were integrated over time to obtain the electrons transferred per gram of samples (Equation 2.2).

$$e^- \text{ transferred (mmol e}^-/\text{g)} = 1000 \times (\int \frac{I}{F} dt) / m \qquad (2.2)$$

where F is Faraday constant (96485 A·s/mol), I is MEO/MER current (A), t is time (s), and m is sample mass (g).

We also measured total Ti (Ti(III)+Ti(IV)) concentration in the solution by inductively coupled plasma mass spectrometry (ICP-MS, ELAN DRC II, Perkin-Elmer, Waltham, MA) following ESC measurement (ca. 210 h) using CRT method. The total Ti concentration in reactors containing 250–500 µm biochar, <53 µm biochar, and no biochar were 11.11±0.27, 11.38±0.05, and 11.19±0.20 mM, respectively, confirming the sorption of Ti(III) and Ti(IV) citrate to SRB was negligible and thus any decrease in Ti(III) concentration can be attributed to oxidation by biochar.

1.2.10 Black carbon samples assessed using the CRT method

A high-purity graphite powder, five commercial biochars (CB1 to CB5) produced from pine wood at different pyrolysis temperatures (450-950 °C), two aged SRB samples that had been applied to soil in a greenhouse stormwater treatment study for 2 years ("Aged SRB-G") [53] and soil in a field demonstration study for 3 years ("Aged SRB-F") [54], and two wood char samples collected from Newbury Park and Simi Valley in January, 2020, following the California wildfire in October, 2019, were analyzed for ESC using the CRT method with Ti(III) citrate and DO. Aged SRB particles were separated from soils using forceps, rinsed with deionized water at 1:50 mass ratio for 24 h at 100 rpm to remove soil minerals attached to the SRB particles,

22

and dried in a vacuum oven at 65 °C. [53] More details about these chars are provided in Table 2.3 and Figure 2.4.

Table 2.3   Information of black carbon samples assessed by CRT with Ti(III) citrate and DO

	Vendor/Sampling Location	Pyrolysis Temperature (°C)	Comments
Graphite	Alfa Aesar (Haverhill, MA)	–	Purity 99.9999%
SRB	The Biochar Company (PA)	550	
CB 1	–	450	Donation from CA
CB 2	Biochar Engineering Corporation (CO)	600	A biochar sample used in the study by Gomez-Eyles et al.[55]
CB 3	Organic Soil Science Biochar (CA)	750	Fast pyrolysis
CB 4	Oregon Biochar Solutions (OR)	900	Fast pyrolysis
CB 5	Oregon Biochar Solutions (OR)	950	Fast pyrolysis
Wildfire Char 1	34°09'07.7"N 118°57'06.3"W (Newbury Park, CA)	–	Fire started on Oct. 10, 2019, char sampled in Jan. 2020 [56]
Wildfire Char 2	34°15'17.8"N 118°48'58.9"W (Simi Valley, CA)	–	Fire started on Oct. 30, 2019, char sampled in Jan. 2020 [56]

CB stands for commercial biochar. All CBs are derived from pine wood. All biochars were ground to have a particle size <53 μm before ESC measurement by CRT.
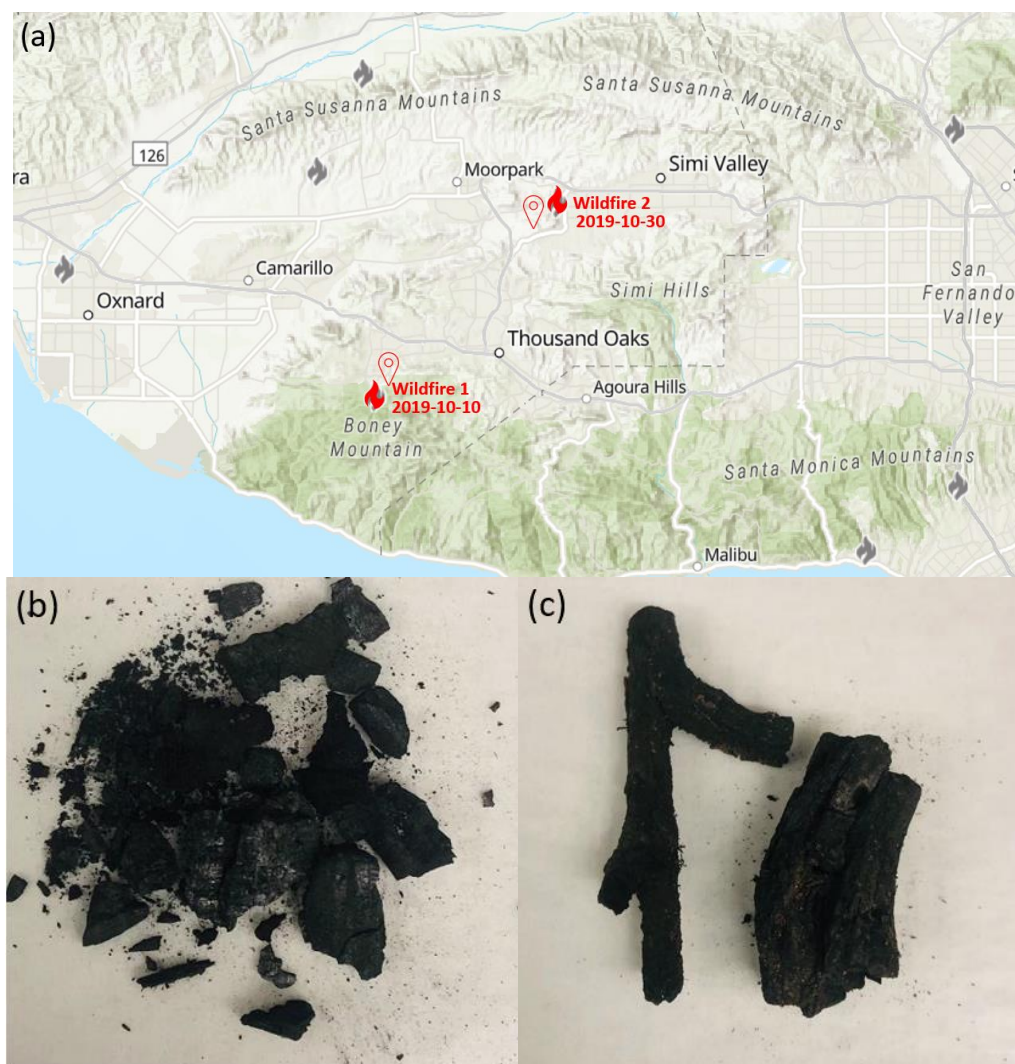
Figure 2.4   (a) Locations of fire events and their start time, and sampling. (b) Image of Wildfire Char 1 (c) Image of Wildfire Char 2

Unless noted otherwise, each sample was ground at 4000 rpm for 3 min using a Beadbug3 bead homogenizer with 3 mm zirconium beads filled in a tube (Benchmark Scientific Inc., Sayreville, NJ) and sifted to <53 μm. Each sample was oxidized individually with DO in continuously aerated deionized water to drain stored

electrons, i.e., to bring the EDC to zero with respect to DO. The oxidized chars were vacuum-filtered, dried, and stored in a desiccator before use.

1.3 Results and Discussion

1.3.1 Biochar EAC measured with Ti(III)

As shown in Figure 2.5, Ti(III) citrate remained stable for days in the glove box without biochar. We further confirmed that the concentration of Ti(III) in citrate solution stayed constant for a month (720 h) in an anaerobic glove box. When a given mass of air-oxidized SRB was added, Ti(III) was consumed rapidly within the first few hours and the consumption slowed but continued for 1–2 days. As discussed above, this was due to Ti(III) oxidation by, rather than sorption to, SRB. After equilibrium, the amount of Ti(III) consumed was proportional to the SRB mass used (Figure 2.5(b)) and an EAC of 3.83±0.22 mmol e⁻/g was obtained from the slope. This suggests, after air oxidation for >72 h, 100-µm SRB possessed a constant capacity to accept ~3.8 mmol of electrons per gram from Ti(III) citrate. The potential of Ti(III) citrate solution at equilibrium was –0.36±0.01 V.
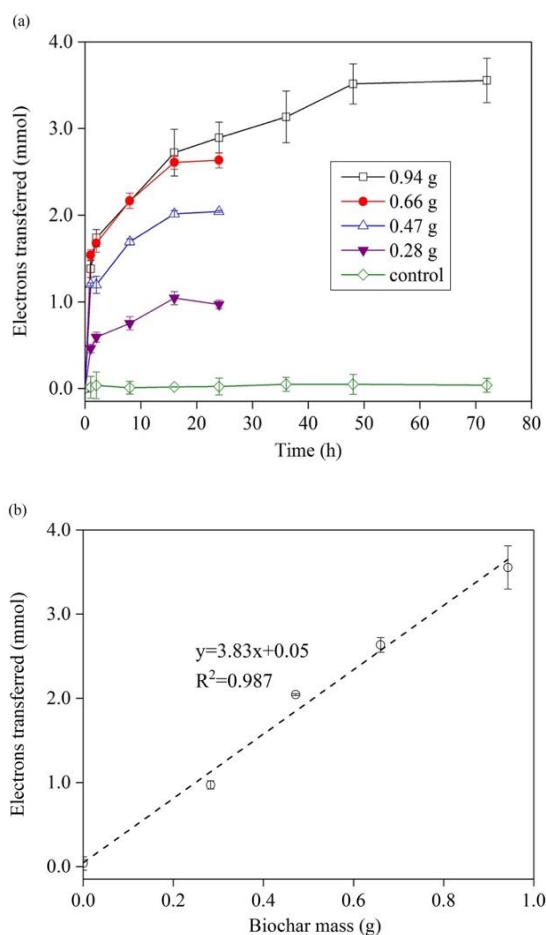
Figure 2.5   Reduction of air-oxidized SRB by Ti(III) citrate as a function of time (a) and of SRB mass at equilibrium (b). Measurements were based on Ti(III) citrate absorbance at 400 nm. Error bars represent one standard deviation.

1.3.2   Rate-limiting step in the reduction of SRB by Ti(III) citrate

The time for equilibration was on the order of a day (Figure 2.5(a)), suggesting a slow rate-limiting step. To be oxidized Ti(III) citrate needed to travel from solution to SRB particle surface, diffuse through pores toward particle interior, and react with a reducible functional group in the interior. Using the method described by Arnold et al. [57] we obtained an aqueous-phase mass transfer rate constant (k_{MT}) of 3.4E-3 s^{-1}.

This corresponds to a half-life of 3.4 min, suggesting mass transfer in bulk solution was not rate-limiting. The EAC of biochar and humic acids has been attributed to quinone functions in their structures. [5, 34, 35] When we used benzoquinone to standardize Ti(III) citrate, the reaction was rapid, as indicated by instant changes in color and UV-vis spectra. This suggests Ti(III) oxidation by the quinones in biochar was also rapid. This leaves pore diffusion as the most probable rate-limiting step.

We estimated the pore diffusion rate constant of Ti(III) citrate in SRB particles using a shrinking unreacted core-shell model as described by Wen (Equation 2.3), [58] where ε is SRB porosity (0.57) [50], C_{Ti} is Ti(III) citrate concentration in pore fluid, $D_{e,Ti}$ is the effective pore diffusivity of Ti(III) citrate, R is SRB particle radius, and r_c is the radius of unreacted core.

$$\varepsilon \frac{\partial C_{Ti}}{\partial t} = D_{e,Ti}(\frac{\partial^2 C_{Ti}}{\partial r^2} + \frac{2}{r}\frac{\partial C_{Ti}}{\partial r}) \qquad (r_c < r < R) \qquad (2.3)$$

We assumed that, as Ti(III) citrate diffused inward through the pores, driven by a concentration gradient along the r, its concentration dropped to zero at the reaction front (the core-shell interface), where Ti(III) was consumed instantly (e.g., by quinones). As the reaction front advanced inward, the unreacted core shrank with time and disappeared completely at $t = t^*$. If we further assumed that quinones were uniformly distributed spatially in SRB particles, the time needed to achieve a given fractional conversion x (= t/t^*) can be calculated for a pore diffusion-controlled process:

$$t = \frac{\gamma R^2 C_{q0}}{6 D_{e,Ti} C_{Ti}}[1 - 3(1 - x)^{\frac{2}{3}} + 2(1 - x)] \qquad (2.4)$$

where γ is reaction stoichiometry (2 for Ti(III) per quinone), R is particle radius (50 μm), and C_{q0} and C_{Ti} are the solid-phase quinone and aqueous-phase Ti(III) citrate concentration, respectively. We then fitted the experimental data to Equation 2.4.

As shown in Figure 2.6, the pore diffusion model fits the 100-μm SRB data well, and gives a pore diffusivity ($D_{e,Ti}$) of 3.6±0.2 E-12 m^2/s, a quinone density of 1.1 mmol per cm^3 envelop volume of air-oxidized SRB, and a reaction completion time (t^*) of 19 h. To confirm this result, we ran another EAC analysis under identical conditions using larger SRB particles, 250–500 μm. This would have resulted in a slight increase or no change in equilibration time if the pore diffusion was not the rate-limiting. However, it took $\geq$5 d for the system to reach equilibrium (Figure 2.6). For 250-μm SRB particles, we obtained fitted $D_{e,Ti}$ of 4.1±0.1 E-12 m^2/s and t^* of 5.2 d, in good agreement with the data. This result suggests pore diffusion in SRB particles was slow, ~1% of the rate in solution (2.8E-10 m^2/s for Ti(III) citrate). While we cannot discern whether the low diffusivity was due to tortuosity, sorption, or other retardation mechanisms, Figure 2.2 suggests that sorption of Ti(III) citrate during pore diffusion was minimal. This result also suggests that redox titration of SRB, and possibly of other porous black carbons, would be controlled by pore diffusion and therefore reaction time for EAC (and EDC) measurements should be selected accordingly.
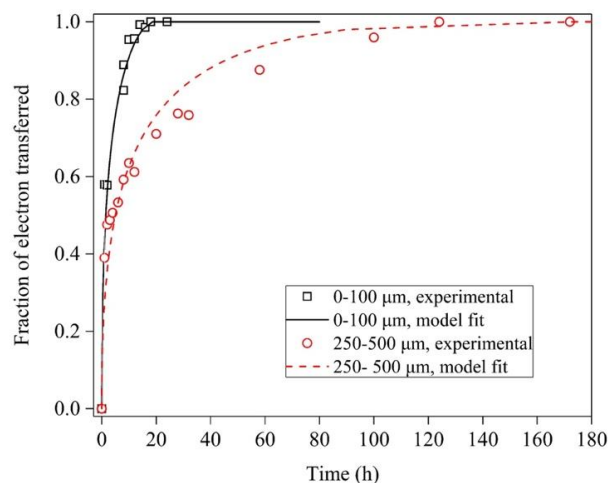
Figure 2.6   Experimental data fitted to the shrinking unreacted core-shell model for the reduction of <100 µm and 250–500 µm SRB particles by Ti(III) citrate. The fraction of electron transferred is the fractional conversion x ($= t/t^*$), as defined in the text.

1.3.3   Biochar EDC measured with Fe(III)-cyanide

Ferricyanide was stable in the glove box but consumed rapidly when Ti(III)-reduced SRB was added (Figure 2.7(a)). As noted earlier, the changes in absorbance and redox potential were due to $[Fe(III)(CN)_6]^{3-}$ reduction by, rather than sorption to, SRB. This was verified by an independent test where no observable sorption of 10 mM $[Fe(III)(CN)_6]^{3-}$ to air-oxidized SRB occurred in 20 mM phosphate solution at pH 7.0 for 24 h, as measured by both the absorbance at 420 nm and E_h. The amount of ferricyanide reacted increased with SRB mass and equilibrium was reached within a day for <100 µm SRB (Figure 2.7(a)) presumably also controlled by pore diffusion. During experiment, the potential decreased from 0.54 to 0.42 V, concomitant with the decreasing absorbance at 420 nm. The ferricyanide concentrations based on absorbance and calculated from E_h and the Nernst equation were almost identical

(Figure 2.8). The EDC of Ti(III)-reduced SRB was 2.03±0.07 and 2.07±0.09 mmol

e^{-}/g, respectively, based on absorbance and E$_h$ (Figure 2.7(b)).
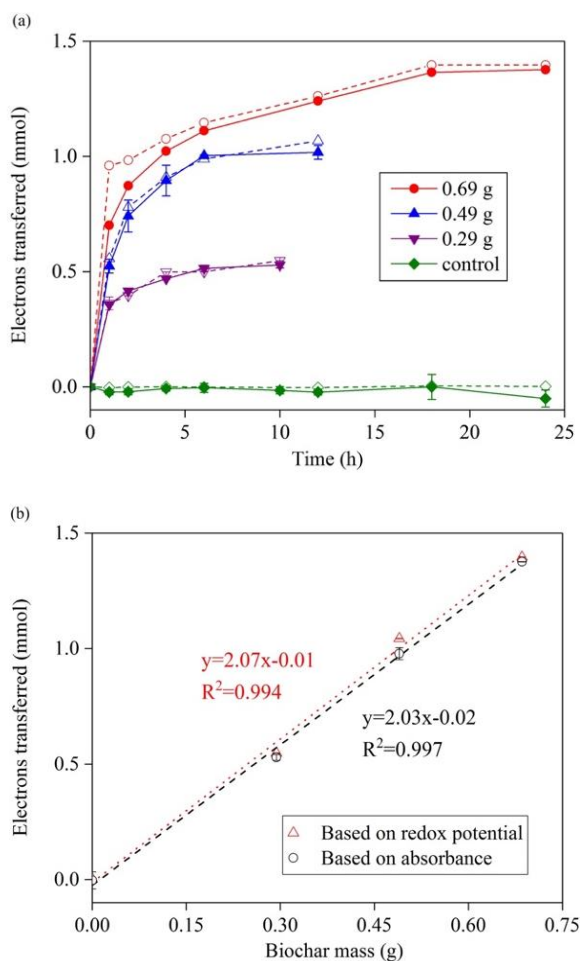
Figure 2.7   (a) Oxidation of Ti(III) citrate-reduced SRB by ferricyanide over time.
Solid lines and filled symbols represent absorbance measurement at 420
nm and dashed lines with open symbols represent redox potential
measurement. (b) Oxidation of Ti(III)-reduced SRB by ferricyanide as a
function of SRB mass at equilibrium. Error bars represent one standard
deviation.
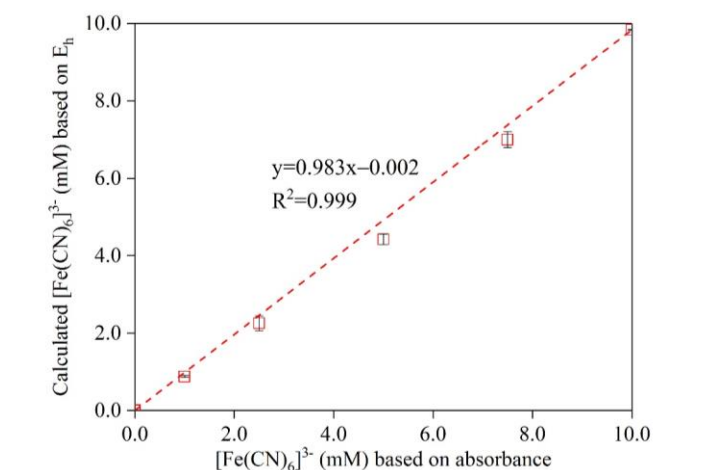
Figure 2.8 $[Fe(III)(CN)_6]^{3-}$ concentrations calculated using measured potentials (E_h) and Nernst equation (Equation 2.5) vs. that obtained from the absorbance at 420 nm. Error bars represent one standard deviation.

$$\text{ferricyanide concentration (mM)} = \frac{10^{[1+\frac{(E_h-0.43)}{0.059}]}}{10^{\frac{(E_h-0.43)}{0.059}}+1} \tag{2.5}$$

The EDC measured with ferricyanide/Ti(III) citrate was markedly lower than the EAC obtained with DO/Ti(III) citrate. This suggests some redox-active functions in SRB were either oxidized by DO (+0.80 V at pH 7, P_{O_2}= 0.21 atm) but not ferricyanide (+0.43 V) or were reduced irreversibly by Ti(III). We also considered the possibility that redox-active metals such as Fe(III) and Mn(IV) in SRB might be released into solution during reduction by Ti(III), contributing to the observed EAC but not EDC. However, this was ruled out by nitric acid extraction data (1 g SRB in 0.5L 2% HNO_3 for 24 h, Table 2.1), which shows these metals combined could not have affected EAC/EDC by more than 0.05 mmol/g. To investigate the reason for the different EAC and EDC, and to assess the redox reversibility of SRB, we performed

repeated redox cycles on the same SRB samples using different oxidant-reductant pairs.

1.3.4 Reversibility of biochar ESC

A virgin SRB sample was first air-oxidized and reduced by Ti(III) citrate (cycle 1), subjected to two cycles of ferricyanide oxidation and Ti(III) reduction (cycles 2 and 3), and air-oxidized for 72 h before reduction again with Ti(III) (cycle 4). Consistent with Figure 2.5, the EAC of virgin SRB was 3.83 mmol e$^-$/g. In cycles 2 and 3, SRB consistently donated and accepted *ca.* 2.0 and 2.5 mmol e$^-$/g, respectively. Thus, the reversible ESC of SRB is at least 2.0 mmol e$^-$/g when measured using Ti(III) citrate and ferricyanide. A possible reason for the different EAC and EDC might be Ti(III)-reduced SRB was partly oxidized by O_2 ($\leq$25 ppm) during sample separation and drying (which took up to 3 d) between EAC and EDC cycles. If this was the reason, the reversible ESC of SRB should be close to 2.5 mmol e$^-$/g when measured with Ti(III) citrate and ferricyanide.
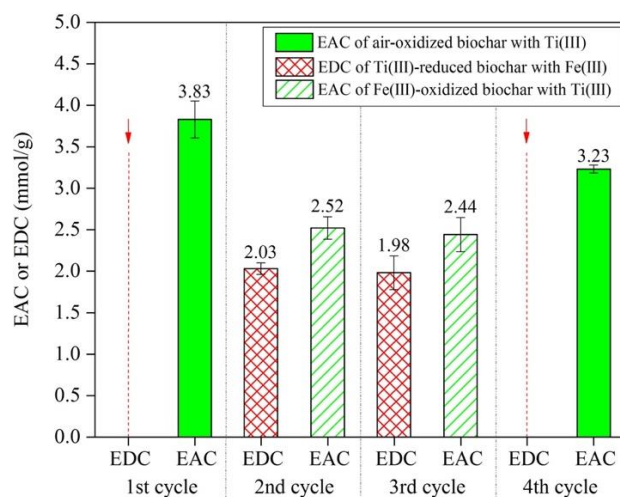
Figure 2.9   EAC and EDC measurements with the same SRB sample over four
             cycles using Ti(III) citrate and ferricyanide as reductant and oxidant,
             respectively. Error bars represent one standard deviation. Down arrow (↓)
             indicates air oxidation of SRB for 72 h before the next EAC analysis.

The fourth cycle clearly shows that DO could consume electrons stored in SRB that ferricyanide could not, resulting in a markedly higher EAC of 3.23 mmol e^-/g (Figure 2.9). This suggests that a portion of SRB's redox-active groups resided between +0.43 and +0.80 V and/or were oxidizable by DO but not ferricyanide. Indeed, when we performed the reversibility study using DO instead of ferricyanide, we obtained the same EAC (~3.0 and 3.3 mmol e^-/g, Figure 2.10(a)), indicating the reversible ESC of SRB was ~3.2 mmol e^-/g when measured using Ti(III) and DO. The fact that the EAC of "used" SRB (Figures 2.9 and 2.10) was reversible but lower than that of virgin SRB (*ca*. 3.8 mmol e^-/g, Figures 2.5 and 2.7) also suggests some functions in SRB were reduced irreversibly during the first Ti(III) treatment and could not be re-oxidizable by ferricyanide or DO.
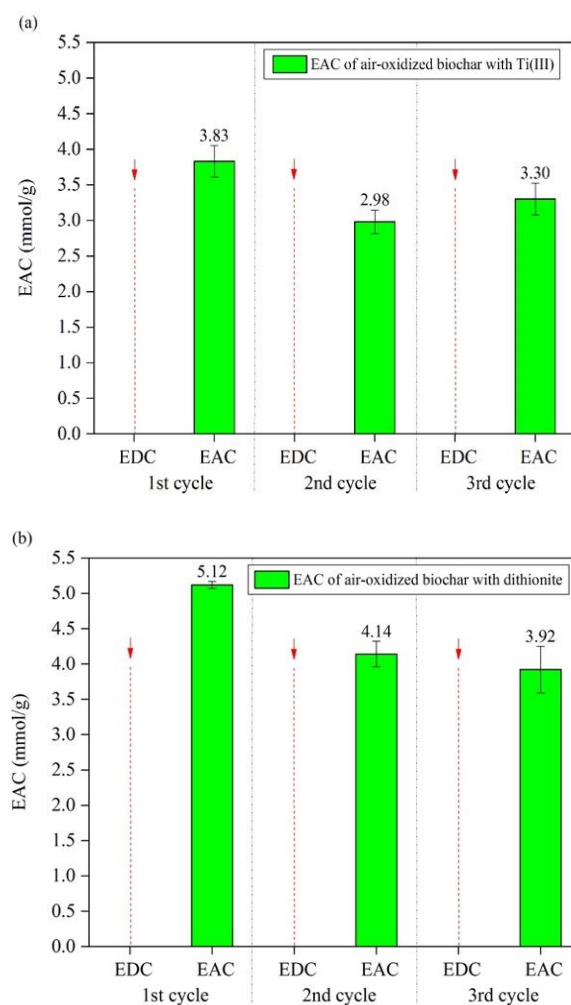
Figure 2.10   Reversibility of SRB ESC assessed with (a) Ti(III) citrate and DO, and (b) dithionite and DO. Arrows (↓) indicate where air oxidation of SRB was performed for 72 hours. Error bars represent one standard deviation.

We also assessed the redox reversibility of SRB using dithionite and DO. The electron content of the dithionite solution in the glove box was constant (Figure 2.11) even though dithionite decomposed over time (based on absorbance at 315 nm, data not shown). [52] The electron content immediately decreased upon the addition of an oxidized SRB sample. The EAC of virgin SRB was ~5.0 mmol e$^-$/g, greater than that

measured with Ti(III). The Eh of dithionite solution at equilibrium was –0.43 V at pH 6.4, more negative than that (–0.36 V) of Ti(III) citrate.
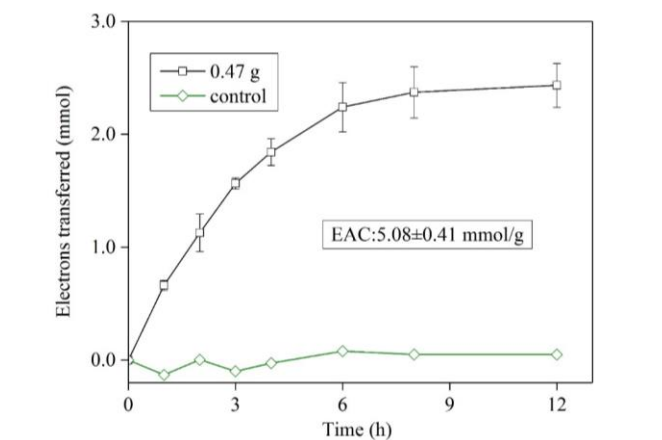
Figure 2.11   Reduction of air-oxidized virgin SRB measured with dithionite/DCPIP over time. Experiment was performed in 200 mL of 5 mM dithionite in 50 mM citrate buffer solution at pH 6.4. Error bars represent one standard deviation.

We then repeated the redox cycle two more times on the same sample and obtained an EAC of ca. 4.0 mmol e⁻/g both times (Figure 2.10(b)). Compared to Ti(III)/DO, the result with dithionite/DO suggests a portion of SRB's redox-facile groups resided between –0.36 V and –0.43 V and/or were reducible by dithionite but not Ti(III), and that certain moieties in virgin SRB were reduced by dithionite irreversibly (ca. 1 mmol e⁻/g). Collectively, results from these multi-cycle measurements suggest that the reversible ESC of SRB was constant for a given reductant-oxidant pair, and was approximately 4.0 mmol e⁻/g in the potential range between dithionite (–0.43 V) and DO (+0.80 V), 3.2 mmol e⁻/g between Ti(III) citrate

(–0.36 V) and DO, and 2.5 mmol e⁻/g between Ti(III) citrate and ferricyanide (+0.43 V).

1.3.5 Comparison of CRT and MEA

CRT quantifies the electron transferred between a sample and a redox titrant; i.e., a soluble, non-sorbing chemical reductant or oxidant, based on titrant consumption. In contrast, MEA quantifies the electrons transferred between a sample and the working electrode based on the current resulting from the electron transfer carried out by a redox mediator. [33] MEA has been applied to biochar by Klüpfel et al. [5] and since 2014 has been used by many to measure the EDC and EAC of biochars. [11-14, 41] EDC and EAC can both vary depending on the redox state of biochar, but their sum (i.e., ESC) should be constant for a given redox potential range. In the CRT method, each sample was oxidized individually with DO to bring the EDC to zero with respect to DO. The ESC was then obtained by measuring the EAC of the DO-oxidized sample using an anionic titrant such as Ti(III) citrate. Given MEA and CRT are different in their approach, sensitivity, and measurement time scale, we need to compare these two methods to confirm whether they yield similar results.

For method comparison, we first measured the ESC of SRB using both MEA and CRT. We also compared the ESC of SRB before (250-500 μm) and after grinding (<53 μm) using both methods. As shown in Figure 2.12(a), the ESC of SRB measured by MEA (hollow stacked bars) was significantly lower than those measured by CRT (solid bars): The ESC obtained by MEA was 0.48 mmol e⁻/g for 250-500 μm SRB and 1.86 mmol e⁻/g for <53 μm SRB, which was 12% and 43% of the ESC measured by CRT with Ti(III) citrate, respectively. In contrast, the ESC obtained using CRT was constant within measurement error for both 250-500 μm and <53 μm SRB (4.11±0.22

and 4.28±0.19 mmol e$^-$/g, respectively). These results show that (1) biochar ESC measured by MEA is particle size-dependent, whereas the ESC measured by CRT with Ti(III) citrate is not, (2) ESC results obtained by MEA are likely underestimated as the method captured only a fraction of the ESC that is measurable by CRT, and (3) a significant portion of the ESC resided in the bulk (i.e., biochar particle interior), as suggested by the effect of grinding.

MEA detects the anodic or cathodic current peak resulting from electron transfer between the working electrode and the mediator (i.e., ABTS or diquat^{2+}). Because biochar is highly porous (e.g., 158 m^2/g for SRB (Table 2.1)), the rate at which solutes, such as redox mediators and Ti(III) citrate, access the interior sites is controlled by pore diffusion (as shown in Section 2.3.2), [59] which occurs over a time scale of many hours to days depending on particle size and pore structure. This time scale is significantly longer than can be detected by a cathodic or anodic current, which is on the order of 1 h (Figures 2.12(b)). MEA can thus capture only the portion of ESC that is "exposed"; i.e., on and near biochar particle surface and readily accessible. The ESC that resides in the particle interior can, in theory, be accessed by mediators slowly over time through pore diffusion, but this would result in a continuous, minute background current that would not produce a detectable peak. This is consistent with the shaper MER current peak and the nearly 4-fold greater ESC observed for ground SRB (<53 μm), which had a higher total geometric surface area and exterior ESC than the non-ground SRB (250-500 μm). Even for SRB particles smaller than 53 μm, more than half of the ESC was in the interior and not measurable by MEA, as shown in Figures 2.12(a).

If we define ESC as the total capacity of biochar to store electrons, then we need a method that can quantify this property in its entirety and yield a consistent and reproducible value that is independent of particle size. Based on our results, we propose that the CRT method is a more suitable and accurate method than MEA for measuring the ESC of biochar and other porous materials. The measurement would take longer, as Ti(III) citrate would require 24–180 h (depending on particle size) to access all interior sites of SRB. In contrast, for soluble materials such as humic acid, for which pore diffusion is not involved, MEA would be an accurate, rapid, and sensitive method for ESC measurement. These two methods have different advantages and limitations and are suitable for different types of samples. If the same reductant/oxidant are used both in the CRT method and as mediators for MEA, then ESC obtained using both methods can be directly compared.
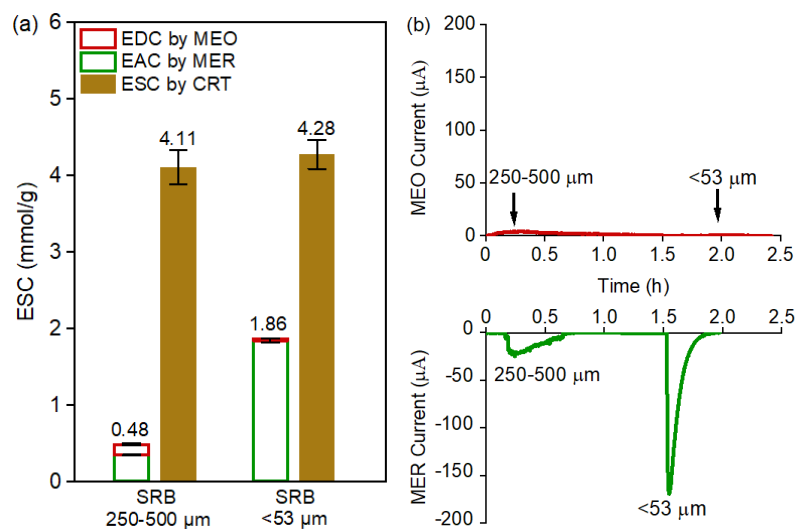
Figure 2.12 (a) Comparison of measured ESC of DO-oxidized SRB, before (250-500 µm) and after grinding (<53 µm), by MEA and CRT with Ti(III) citrate. The EDC measured by MEA (red hollow bars) for 250-500 µm and <53 µm SRB was 0.14 and 0.03 mmol e⁻/g, respectively. (b) MEO and MER current peaks for DO-oxidized SRB before and after grinding.

1.3.6 Surveying the ESC of black carbon using CRT

Figure 2.13 shows the ESC of 20 black carbon samples measured by CRT with Ti(III) citrate and DO. Graphite, a reference black carbon that contained few functional groups, gave zero ESC. In contrast, commercial biochars (SRB, CB1-5) possessed significant and highly reversible ESC, ranging from 1–7 mmol e⁻/g. These biochars were all produced from wood, but at different temperatures (450-950 °C) and pyrolysis conditions (e.g., residence time and exposure to air) which resulted in different ESC. All black carbon ESC showed high reversibility over three consecutive redox cycles. SRB contained a reversible ESC around 2.5 mmol e⁻/g. SRB has been applied to soil in a greenhouse experiment for 2 years [53] and in a field demonstration site for 3 years for stormwater treatment [54]. When the SRB was retrieved, interestingly, the ESC of aged SRB samples from the greenhouse and the

field site still retained ca. 2.3 mmol e⁻/g of fully reversible ESC, a value similar to the reversible ESC of virgin SRB. These results suggest that the ESC of black carbon and its rechargeability are long-lasting even under field conditions.

Since Klüpfel et al. (2014) [5] first applied MEA to demonstrate the electron donating and accepting properties of biochar, multiple studies have applied MEA to measure biochar ESC. [10-14] These ESC data by MEA are compiled in Figure 2.13(b) for comparison. All these biochars were produced through pyrolysis of lignocellulosic biomass, though pyrolysis conditions varied. With one exception (G400), all the ESC measured by MEA were ≤1 mmol e⁻/g and many significantly below. In contrast, when measured by CRT (Figure 2.13(a)), all samples pyrolyzed at >350 °C possessed ESC ≥1 mmol e⁻/g (except W550 0.89±0.01 mmol e⁻/g) and most significantly higher. These results support that MEA would underestimate biochar ESC. It is critical that this be understood and caution be exercised when comparing reported EDC/EAC/ESC data across samples and studies to avoid erroneous interpretations and conclusions.
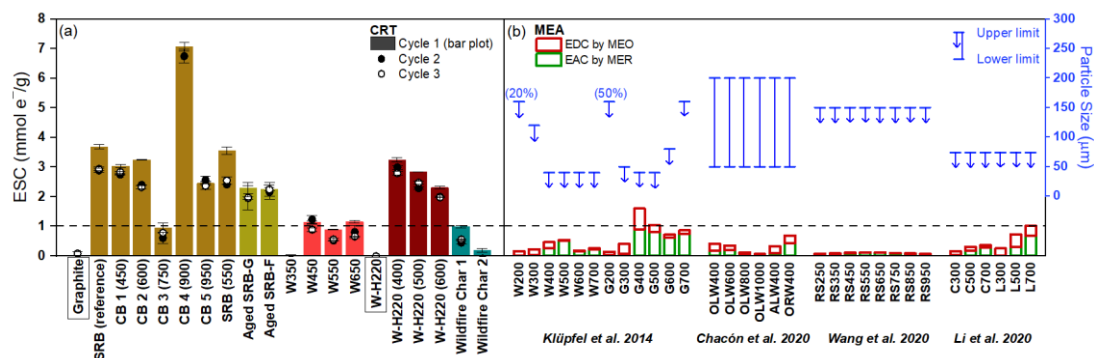
Figure 2.13 Comparison of ESC of black carbon measured by CRT with Ti(III) citrate and DO in this work (a) and reported ESC measured by MEA (b). (a) All black carbon samples measured by CRT had a particle size <53 µm. "CB" stands for commercial biochar and numbers in parenthesis represent pyrolysis temperature. Two black carbon samples, Graphite and W-H220, were not produced through pyrolysis. (b) |→ and |–| (in blue) represent the upper limit and range of particle size of biochar, respectively, except that, for the data from Wang et al., |→ shows the particle size of the feedstock. For W200 and G200, only 20% and 50% of biochar were below the particle size marked in the figure, respectively.

1.4   Conclusions and Environmental Implications

The EAC and EDC of humic acid and black carbon have been reported and attributed to quinone groups in these carbonaceous materials. [5, 34, 35] However, the total ESC of biochar and other black carbon has not shown to be reversible or constant. Our data indicate the ESC of biochar obtained over repeated redox cycles was constant for a given pair of reductant and oxidant, confirming the reversible nature of ESC and supporting the involvement of redox-labile moieties such as quinones. The CRT methods described in this Chapter can be used to obtain biochar ESC easily by using DO and a reductant of suitable E_h^o. When we applied the CRT method with Ti(III) citrate and DO to survey different types of black carbons, the

results showed that reversible ESC may be a constant and quantifiable property of black carbon, similar to BET surface area.

Redox potential distribution of biochar has not been reported, in part because many mediators [33] that have been applied successfully to obtain potential profiles of iron minerals and humic acids would sorb to biochar. Using four reductants/oxidants and by preventing their sorption to biochar, we obtained a rough potential distribution for SRB: approximately 0.8 mmol e$^-$/g between –0.43 and –0.36 V, 2.5 mmol e$^-$/g between –0.36 and +0.43 V, and 0.7 mmol e$^-$/g between +0.43 and +0.80 V. For biochar with a low anion exchange capacity, [60] a more detailed redox potential profile may be obtained by the CRT, if additional inorganic and anionic mediators of suitable E_h^o can be identified.

The result that pore diffusion was the rate-limiting step has implications for not only EAC/EDC measurement but also contaminant fate and treatment. It suggests that the fraction of the ESC of biochar available for contaminant (bio)transformation may depend on the retention time. In a rapid flow-through system, only the ESC at/near biochar surface would be available. Conversely, if the retention time is hours to days (depending on biochar particle size), redox-facile molecules such as quinones, flavins, and iron complexes would have time to diffuse in and out of deep pores and access a larger portion of the ESC.

The ESC of SRB accessible to *G. metallireducens* was reported to be ca. 0.86 mmol e$^-$/g, [6] which is 22% of the reversible ESC obtained with dithionite and DO. This percentage is surprisingly high, given the BET surface area of 100-µm SRB is ~3700 times its geometric surface area and that *G. metallireducens* presumably could access only redox moieties at/near SRB surface. Michelson et al. showed *G.*

sulfurreducens could access <200 nm pores through nanowires to reduce MnO_2 up to 15 µm away, and up to 40 µm when a soluble mediator such as AQDS was present. [61] These strategies might be employed by *G. metallireducens*, which is known to produce cytochromes, [62] to access the redox moieties in biochar.

Compared to the smallest quinone, 1,4-benzoquinone, which has an ESC of 18.5 mmol e⁻/g, the reversible ESC of SRB is 22% that value. This shows black carbon could possess a high quinone content. The ESC of SRB is also comparable to those (0.5–7 mmol e⁻/g organic carbon) [35, 36, 63, 64] reported for dissolved and particulate organic matter, suggesting black carbon may play an important role in environmental redox cycling. Finally, ESC would be an important design parameter for remediation applications where biochar is used as an electron donor and/or acceptor. It may be possible to optimize biochar ESC by choosing the "right" biomass and pyrolysis conditions for enhanced redox performance. CRT methods will be essential tools for these investigations.

Chapter 3

VISUALIZING THE SPATIAL DISTRIBUTION OF ELECTRON STORAGE CAPACITY OF BLACK CARBON THROUGH SILVER TAGGING

This chapter is a reprinted version of an articles published in Chemosphere: "Reprinted with permission from Chemosphere 2020, 248, 125952. Copyright 2020 Elsevier."

1.5   Introduction

The fact that black carbon can donate, accept, and/or conduct electrons chemically and microbially not only has important implications for the biogeochemical cycling of redox-active elements and the fate of contaminants in subsurface environments [2, 65], but also offers opportunities for developing novel, cost-effective remediation methods and site management strategies [44, 66-68]. The electron storage capacity (ESC) of black carbon is an important property that determines its capacity to support redox reactions in natural and engineered systems. Through the ESC, the electrons can be deposited into or vacated from the redox-facile (e.g., hydro/quinoic [24, 69]) functional groups of black carbon and then accessed at a different location and/or a later time. In Chapter 2, we showed that the ESC of biochar is highly reversible for a given oxidant-reductant pair [70, 71]. This is particularly important for environmental applications where black carbon donates/accepts electrons to support chemical and microbial degradation. Furthermore, because the electrons and vacancies in black carbon can be regenerated repeatedly, the ESC of

black carbon may have long-lasting impacts on how electrons flow in (intermittently) anaerobic environments, similar to the ESC of natural organic matter [72-74].

To date, however, it remains unclear where ESC is located in black carbon. Using dithionite as a reductant (–0.43 V vs. SHE, at pH 6.4) and dissolved O_2 (DO) as an oxidant (+0.80 V vs. SHE at P_{O_2}=0.21 atm and pH 7), we determined that the reversible ESC of Soil Reef biochar (SRB) is ca. 4 mmol/g. These measurements took hours to days to complete depending on the particle size, because the rate to access the ESC was controlled by pore diffusion of reductant or oxidant molecules within SRB particles. In a separate study, only 22% of the ESC (i.e., 0.86 mmol of electrons or electron vacancies per gram) could be accessed by the bacterium *Geobacter metallireducens* [6]. This suggests that a large portion of the ESC accessible to solute molecules was not accessible to microbes. These examples illustrate the need to determine the location of ESC in black carbon, as it controls not only the amount of accessible electrons and electron vacancies [6, 61, 75] but also the kinetics of redox reactions involving black carbon [70, 76].

In Chapter 3, we use Ag^+ as a tagging agent to probe the location of ESC on and within biochar particles. SRB was first reduced (i.e., ESC was saturated with 4 mmol e^- per gram) using dithionite, and Ag^+ was allowed to diffuse into the pores of reduced SRB to react with the stored electrons, producing Ag^0 nanoparticles (nAg) in situ at or near where ESC was located. As ESC markers, nAg were then visualized by electron microscopy to obtain the spatial distribution of ESC in intact and sectioned biochar particles.

1.6 Materials and Methods

1.6.1 Chemicals

Silver nitrate (99.9+%) and sodium dithionite (>85%) were purchased from Alfa Aesar (Haverhill, MA). Sodium nitrate (99.8%), sodium hydroxide solution (1.0 N), and nitric acid (67–70%, trace metal grade) were obtained from Fisher Scientific (Hampton, NH). Sodium citrate (99%) and 1,4-hydroquinone (99.5%) were acquired from ACROS Organics (Morris Plains, NJ). All chemicals were used as received.

1.6.2 Biochar

We used SRB in the size range of 250–500 μm from the same batch as in Chapter 2 and earlier studies [6] to allow direct comparison of data. SRB was used either directly (250–500 μm) or ground to generate subsamples of <100 μm for selected experiments. All reported Ag loadings are based on the dry weight.

1.6.3 Silver uptake by SRB

All experiments were performed in an anaerobic glove box (2.0±0.5% H_2, 98±0.5% N_2, P_{O_2}<25 ppm, Coy, MI). SRB was first oxidized with DO in air-saturated deionized water for 72 h to thoroughly deplete stored electrons. A sample of the oxidized SRB was then reduced in a solution containing 25 mM dithionite and 0.1 M citrate at pH 6.4 for 72 h in an anaerobic glove box. The dithionite solution had a measured reduction potential (E_h) of –0.43 V vs. SHE. Due to its high reactivity, dithionite was added in excess and was replenished as needed to ensure a complete reduction of SRB. Reduced SRB was collected on a glass fiber filter disc, rinsed thoroughly with deoxygenated deionized water to remove all residual chemicals, and vacuum-dried prior to Ag^+ addition. The oxidized and reduced SRB (SRB_{OX} and

SRB$_{RED}$, respectively) were rinsed thoroughly with DO-free water and dried in a glove box.

Ag$^+$ was added to a known mass of SRB$_{OX}$ or SRB$_{RED}$ suspended in NaNO$_3$ solution maintained at a constant pH of 6, 7, or 8 using a pH controller. Aqueous Ag$^+$ concentration was monitored continually and replenished as needed. Ag loading (mmol Ag/g SRB) was calculated from the mass balance at equilibrium. Specifically, a known mass (1 g) of SRB was suspended in 0.2 L of 0.1 M NaNO$_3$ solution in a 1 L amber glass bottle on an orbital shaker at 100 rpm. After equilibration for 30 min with NaNO$_3$ solution, a pre-determined aliquot of 100 mM AgNO$_3$ was added to the SRB. Aqueous Ag$^+$ concentration was monitored continuously using an Ag$^+$ ion-selective electrode (ISE) and an ISE meter (Cole–Parmer, Vernon Hills, IL). As Ag$^+$ concentration dropped below 1 mM, another aliquot of AgNO$_3$ would be added. As H$^+$ was produced due to cation exchange and Ag$^+$ reduction (Equation 3.3), an automatic pH controller (Bluelab, Tauranga, New Zealand) was used to maintain the solution pH at a preset value (±0.4) throughout each experiment using 5 mM NaOH in 0.1 M NaNO$_3$. The Ag$^+$ ISE was calibrated periodically against Ag$^+$ standards. The Ag loading of SRB was obtained from mass balance using Equation 3.4.

$$Ag^+ + e^- \rightleftharpoons Ag^0_{(s)}\downarrow \tag{3.1}$$

$$C=O_{(quinone)} + H^+ + e^- \rightleftharpoons C-OH_{(hydroquinone)} \tag{3.2}$$

$$Ag^+ + C-OH_{(hydroquinone)} \rightleftharpoons C=O_{(quinone)} + H^+ + Ag^0_{(s)}\downarrow \tag{3.3}$$
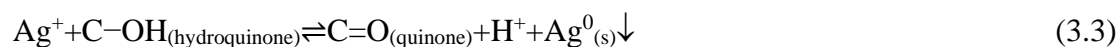
$$Ag\ loading\ (mmol) = C_{AgNO3} \times jV_{AgNO3} - C_i \times (V_{NaNO3} + jV_{AgNO3} + V_{NaOH}) \tag{3.4}$$

where C$_{AgNO3}$ and C$_i$ are concentrations of Ag$^+$ in the stock solution (100 mM) and in the reactor at the time of the ith measurement, respectively; j is the total number of AgNO$_3$ aliquots added; V$_{NaNO3}$ is the initial solution volume (0.2 L), V$_{AgNO3}$ is the

volume of $AgNO_3$ added each time (0.005 L), and V_{NaOH} is the total volume of NaOH added.

1.6.4 Characterization of SRB and Ag/SRB

Ag addition to 250–500 µm SRB_{RED} particles was performed at pH 7 following the method above. The product (denoted "Ag/SRB") was rinsed, retrieved from a glass microfiber filter, dried, and stored in a desiccator in a glove box before use. Ag loading was confirmed using inductively coupled plasma-mass spectrometry (ICP-MS 7500C, Agilent, CA) through acid digestion. Physical-chemical properties of SRB and Ag/SRB were determined and summarized in Table 3.1.

Table 3.1   Physical-chemical properties of SRB and Ag/SRB (250–500 µm, prepared at pH 7.0)

Properties	SRB	Ag/SRB	Method
Ag Loading	–	2.03±0.2 mmol/g (21.93±2.5%, w/w)	Acid digestion (1:1000 w/v in 35% HNO_3, 72 h)
CEC	0.24±0.01 mmol/g	–	NH_4^+ saturation
pH	7.23±0.02 (S.U.)	6.46±0.15	1:20 w/v in deionized water, 24 h
BET Surface Area	164.48 m^2/g	94.04 m^2/g	N_2 adsorption

Errors represent one standard deviation from triplicate measurements.

Scanning electron microscopy (SEM), energy dispersive X-ray spectroscopy (EDS), X-ray diffraction (XRD), transmission electron microscopy (TEM), and scanning TEM (STEM) were used to characterize the composition and morphology of Ag/SRB and the size and spatial distribution of nAg.

1.6.4.1 SEM–EDS

SEM images were taken for SRB and Ag/SRB using an Auriga 60 CrossBeam high-resolution SEM (ZEISS, Oberkochen, Germany) operating at 1.5–3.0 kV and imaging with secondary electron detectors. This instrument is equipped with an Oxford X-Max EDS silicon drift detector (SDD), which can determine the elemental composition of Ag/SRB. Selected SEM images were processed with ImageJ software to obtain particle size distribution.

1.6.4.2 XRD analysis

To obtain crystalline structural information, SRB and Ag/SRB were analyzed using a Bruker D8 XRD (Bruker, Billerica, MA) equipped with a LynxEye position sensitive detector. This instrument was operated with monochromatic Cu–Kα1 line at 40 kV and 40 mA by scanning 2θ ranging from 20° to 70° with a step size of 0.05°. The XRD data were analyzed for the phase of crystallites using DIFFRAC.EVA v3.1.

1.6.4.3 TEM and STEM imaging and STEM tomography

Ag/SRB was dispersed in an ethanol solution before transfer to a copper grid with carbon support film for TEM and STEM imaging. To obtain the distribution of Ag^0 nanoparticles (nAg) in the interior of Ag/SRB, a few Ag/SRB particles were cured with low viscosity Spurr embedding resin at 70 °C in a vacuum oven and sectioned with a diamond knife microtome into 80 nm sections. TEM and STEM images of microtomed Ag/SRB were obtained using a JEM–2010F (JEOL, Tokyo, Japan) and a Talos F200C (Thermo Fisher Scientific, Waltham, MA) operated at 200 kV. The STEM images were taken using an HAADF detector. Additionally, HAADF–STEM tomography was performed to construct a 3D image of Ag/SRB using a Talos F200C with a Fischione tomography sample holder. The sample holder was tilted from

–70° to +70° and images were captured every few degrees. Tomography reconstruction was conducted with Avizo and Inspect 3D software (Thermo Fisher Scientific).

1.7 Results and Discussion

We used anionic reductants and oxidants to measure ESC (in Chapter 2) to minimize sorption because plant-based biochars typically have limited anion exchange capacity but significant cation exchange capacity (CEC) [77]. SRB is negatively charged at pH 7 and has a CEC of 0.24 mmol/g (Table 3.1). This is consistent with the maximum Ag^+ uptake of 0.27 mmol/g by <100-µm SRB_{OX} at pH 7.0 (Figure 3.1(a)). In contrast, the Ag^+ uptake by <100-µm SRB_{RED} was much greater, plateauing at ~2.3 mmol/g. Despite the marked difference, the time required both SRB_{OX} and SRB_{RED} to reach the maximum uptake was similar (>2 d), suggesting the same process, i.e., inward diffusion of Ag^+ through pores within SRB particles, controlled the rate of Ag^+ uptake. For 250–500 µm SRB_{RED}, the same maximum uptake of 2.3 mmol/g was obtained, but it took much longer to reach equilibrium than for <100-µm SRB_{RED} (Figure 3.1(a)), again consistent with pore diffusion-limited solute transport. Assuming the same CEC for SRB_{OX} and SRB_{RED}, the greater uptake by SRB_{RED} can be attributed to Ag^+ reduction (Equation 3.1) by functional groups such as hydroquinones (Equation 3.2) [78-80] in SRB_{RED}.

The amount of stored electron consumed, and Ag^0 formed, was hence ca. 2.0 mmol/g at pH 7.0. Based on the standard reduction potential ($E_h°$) of Ag^+/Ag^0 and quinone redox couples (Figure A.1(b) and Table A.1), Ag^0 formation through electron transfer from hydroquinones (Equation 3.3) is thermodynamically favorable. Consistent with our results, Yao et al. [81] reported Ag^+ uptake by biochar through

both sorption and reduction, up to 0.72 mmol/g. The much lower Ag^+ reduction was presumably because their biochar was not pre-reduced and therefore much of its ESC was (electron-)vacant.

As pH increased from 6 to 8, Ag^+ uptake increased from 0.17 to 0.48 mmol/g for SRB_{OX} and from 1.75 to 2.97 mmol/g for SRB_{RED} (Figure 3.1(b)). Assuming the same CEC for SRB_{OX} and SRB_{RED} at each pH, the amounts of Ag^+ reduced were 1.58, 2.02, and 2.49 mmol/g at pH 6, 7 and 8, respectively. The pH effects on Ag^+ adsorption and reduction [78] can be readily understood. The CEC of SRB increased with pH due to the deprotonation of carboxylic and phenolic groups, resulting in greater Ag^+ adsorption at higher pH. The reduction potential of a quinone to its corresponding protonated hydroquinone decreases by 59 mV for each unit increase in pH, since the same number of protons and electrons are involved (Equation 3.2). [82, 83] This has been demonstrated for humic acid [35] and would also be true for BC that contain the same (quinone) moieties [24, 69]. In contrast, the reduction potential of Ag^+ is pH-independent (+0.80 V vs. SHE) since no proton is involved. Thus, Ag^+ was expected to be reduced to a greater extent because of a stronger thermodynamic driving force for its reduction at a higher pH, as shown in Figure A.1(b). Experiments at pH 9 or above were infeasible due to Ag^+ precipitation (Figure A.1(a)).
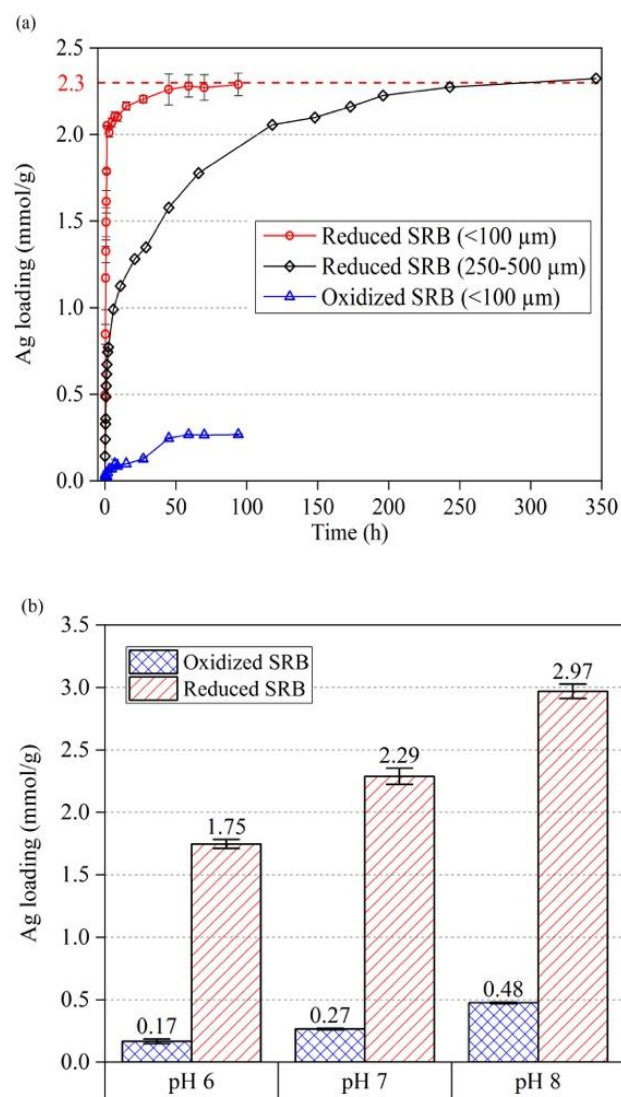
Figure 3.1   (a) Ag$^+$ uptake by air-oxidized and dithionite-reduced SRB at pH 7. The horizontal dashed line indicates the same maximum Ag loading of ca. 2.3 mmol/g for reduced SRB of two different sizes. (b) Maximum Ag loadings for oxidized and reduced SRB at pH 6, 7, and 8. All values are based on dry SRB mass. Error bars represent the range from duplicate measurements.

Interestingly, although Ag^+ and DO (at P_{O_2}=0.21 atm) have essentially the same E_h^0 at pH 7, the electrons in dithionite-reduced SRB that were accessed by Ag^+ at pH 7 and 8 were only 50% and 62% that accessible to DO (~4.0 mmol/g) [70]. The notably lower accessibility of ESC by Ag^+ was most likely due to the blocking of pores and channels [84] in SRB by freshly produced nAg, preventing subsequent access of Ag^+ to the ESC in deep pores. Consistent with this explanation, the specific (BET) area of Ag/SRB was 43% lower than that of SRB (Table 3.1). Nonetheless, Ag^+ was able to access and tag >60% of the ESC and thus would permit ESC visualization via Ag^0 formation.

The distinct atomic weights of Ag and C enable visualization of nAg in BC through electron microscopy. Using SEM, no nAg were observed on the SRB surface (Figure 3.2(a)), whereas Ag/SRB surface was densely covered by nanoparticles (Figure 3.2(b)). EDS mapping showed the abundance of Ag on Ag/SRB (Figures 3.2(c) and 3.3), and XRD analysis further confirmed the formation of elemental Ag^0 with predominant peaks corresponding to face-centered cubic (*fcc*) Ag^0 (Figure 3.4) [78, 85]. The measured *d*-spacing of 2.40 Å by TEM (Figure 3.5) is consistent with the inter-atomic *d*-spacing of the (111) lattice plane found at 38.12° of the XRD spectrum. This result is also in good agreement with the calculated inter-planar spacing between (111) planes along the [111] direction [86], confirming the reductive formation of nAg^0 crystals. A particle size analysis of the SEM images of Ag/SRB surface showed that most nAg were in the size range of 20–70 nm, with a mean particle size of ca. 45 nm (Figure 3.6). When the Ag/SRB surface was further magnified by high-angle annular dark-field (HAADF)–STEM, nAg of 1–5 nm became visible and were ubiquitous and well-dispersed (Figures 3.2(d)). These results show nAg were formed

abundantly and uniformly, albeit in variable sizes (1–100 nm), suggesting a high ESC density on or near the SRB surface.
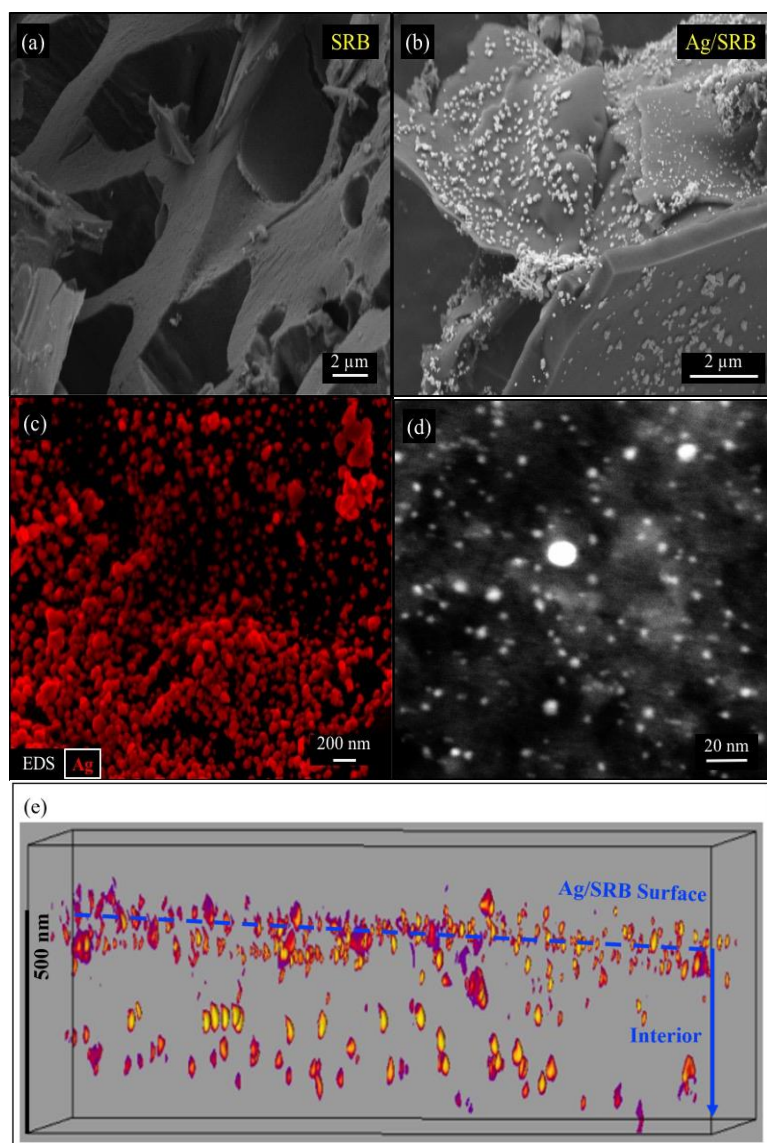
Figure 3.2   SEM images of (a) SRB and (b) Ag/SRB. (c) Elemental mapping of Ag on Ag/SRB by SEM–EDS. (d) HAADF–STEM image of Ag/SRB containing small (1–5 nm) nAg. (e) An image of the STEM tomography 3D reconstruction illustrating nAg distribution in Ag/SRB.
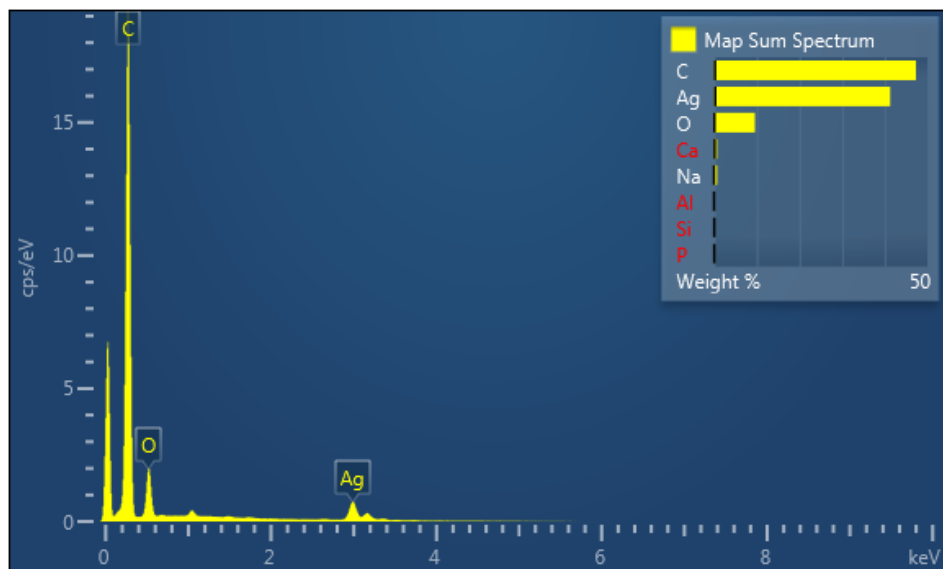
Figure 3.3   SEM–EDS elemental analysis of Ag/SRB
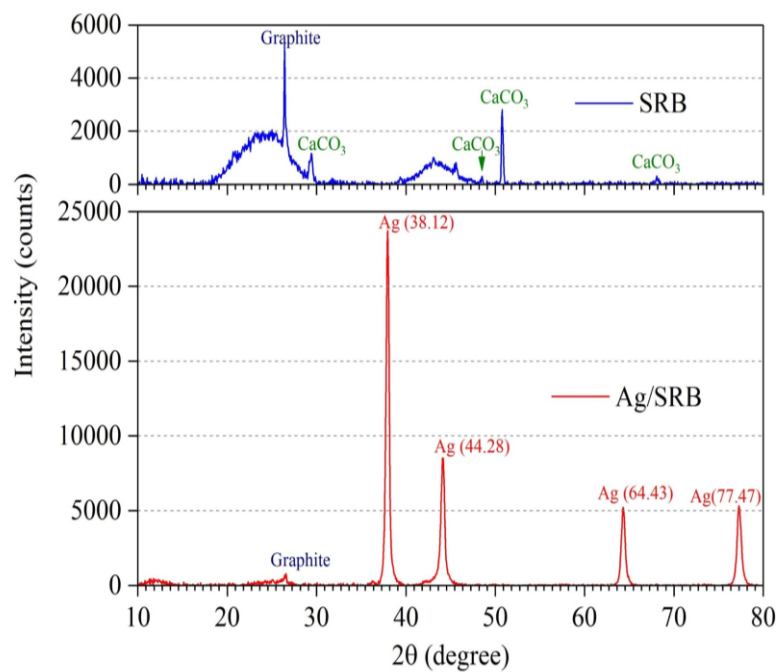
Figure 3.4   XRD spectra of SRB and Ag/SRB
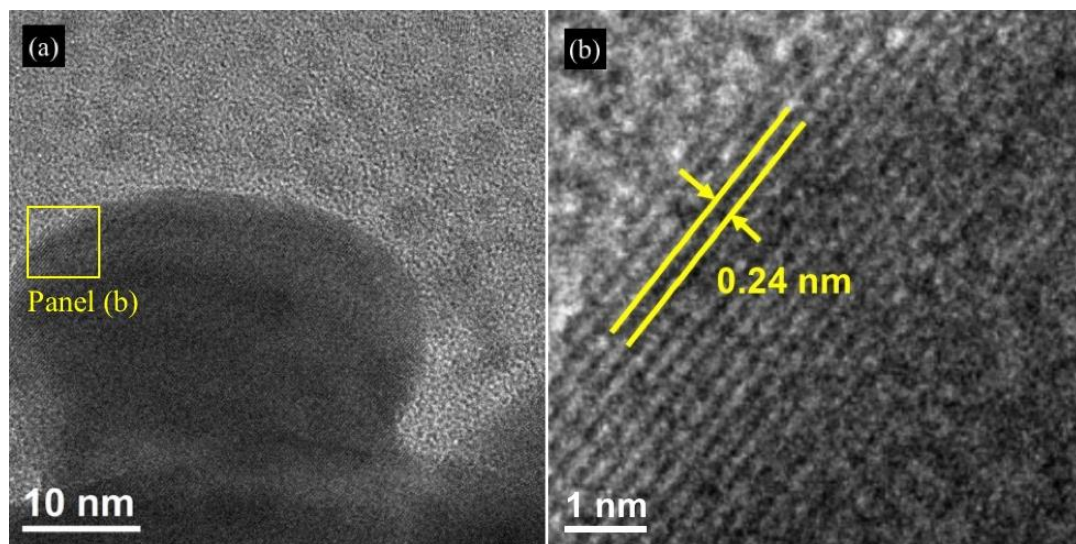
Figure 3.5   Atomic d-spacing of the lattice of nAg
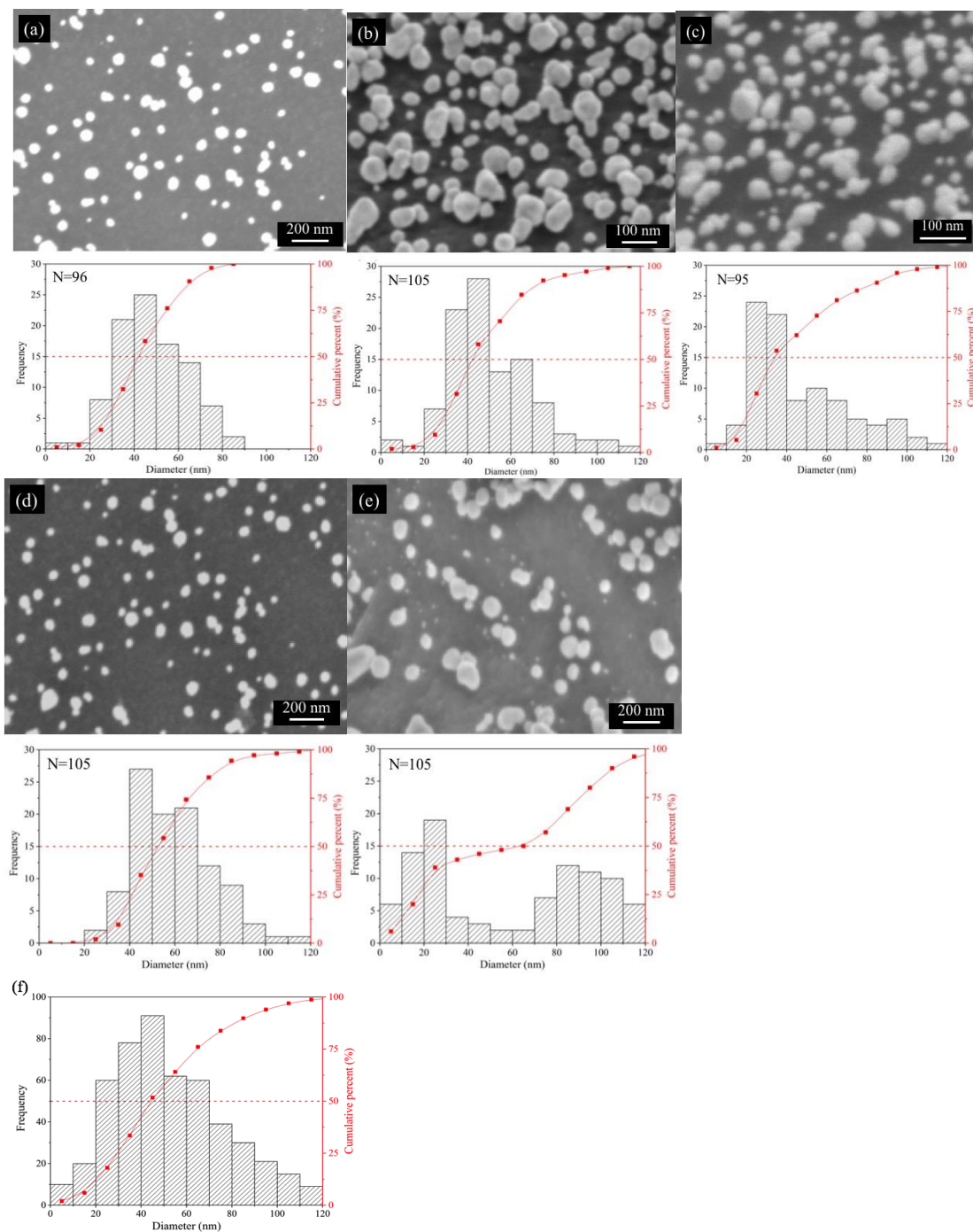
Figure 3.6   (a)–(e) SEM images and particle size distributions of nAg. N denotes the number of visible nAg in each SEM image. (f) Overall nAg particle size distribution. The frequency of nAg at each diameter range is the sum of the nAg in the same range in panels (a)–(e).

To visualize the spatial distribution of nAg in the biochar interior, STEM tomography was applied to a depth of ~500 nm from the surface (i.e., its detection limit). Numerous and dispersed nAg were also observed, though the density was lower than at the surface (Figure 3.2(e)). This shows that significant ESC existed in the SRB interior, not on the geometric surface. To probe the ESC distribution in even deeper regions, a 250 µm Ag/SRB particle was sectioned using a microtome. nAg would appear dark in TEM images (Figure 3.7) and bright in HAADF–STEM images (Figures 3.8 and Figures 3.9) due to its high atomic mass. Figure 3.7, a cross-section TEM image of Ag/SRB, locates the images taken through HAADF–STEM. Figures 3.8 and 3.9 show nAg were formed ubiquitously in the interior of SRB, supporting the hypothesis that Ag^+ was transported via pore diffusion and reductively deposited on the interior surface. While >10 nm nAg were formed on the surface (Figures 3.2(b) and 3.6) and in large pores (Figure 3.10), 1–10 nm nAg were observed throughout Ag/SRB, both on the surface and in the interior, when imaged with HAADF–STEM at high magnification (Figures 3.2(d), 3.8(d), and 3.9(c)). The ubiquity of small nAg in deep pores suggests they were formed *in situ* at or near where electrons were stored, with size controlled by either the electrons available locally and/or the connectivity of pores.
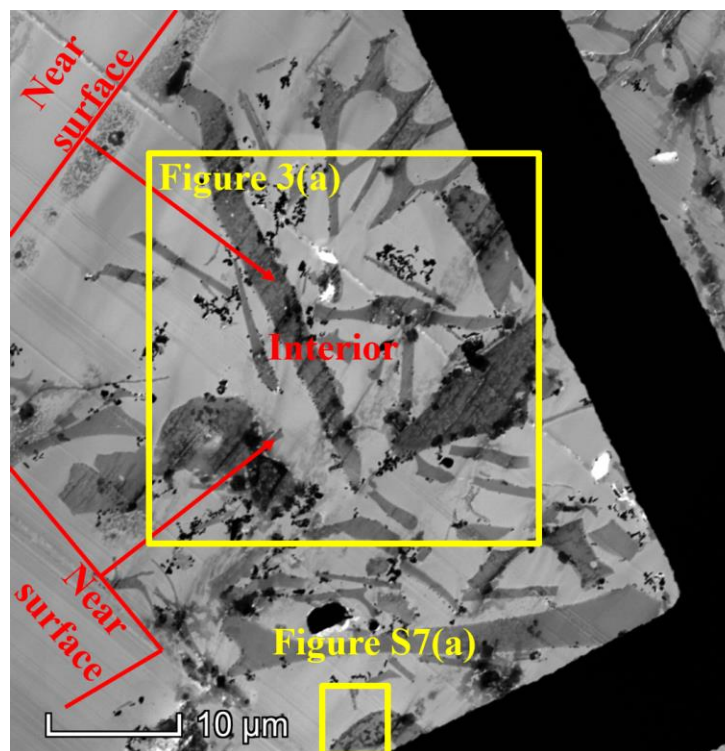
Figure 3.7   TEM image of the microtomed cross-section of a single Ag/SRB particle,
            locating the HAADF–STEM images shown in Figure 3.8 and Figure 3.9.
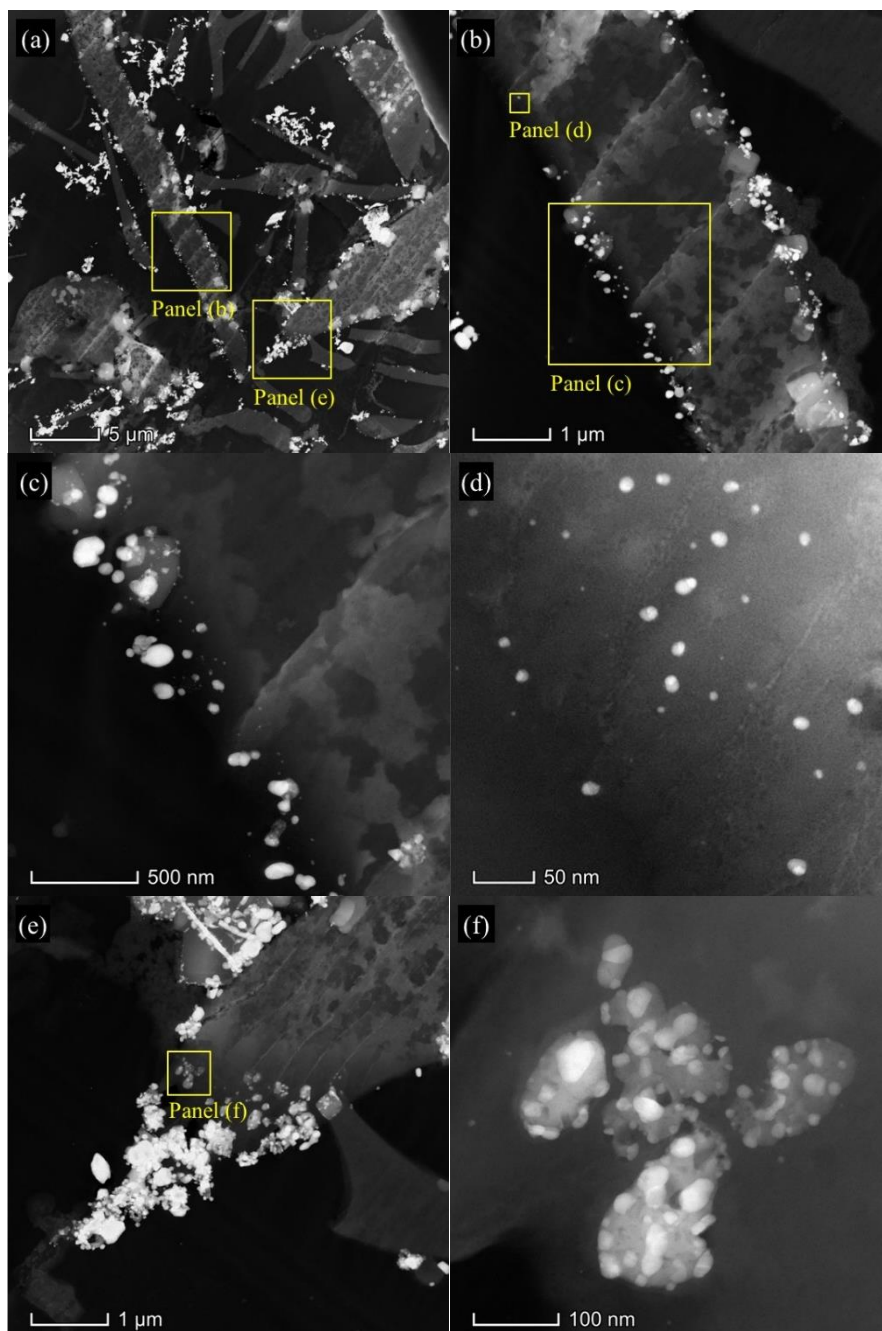
Figure 3.8   HAADF–STEM images of the microtomed cross-section of a single
Ag/SRB particle at different magnifications.
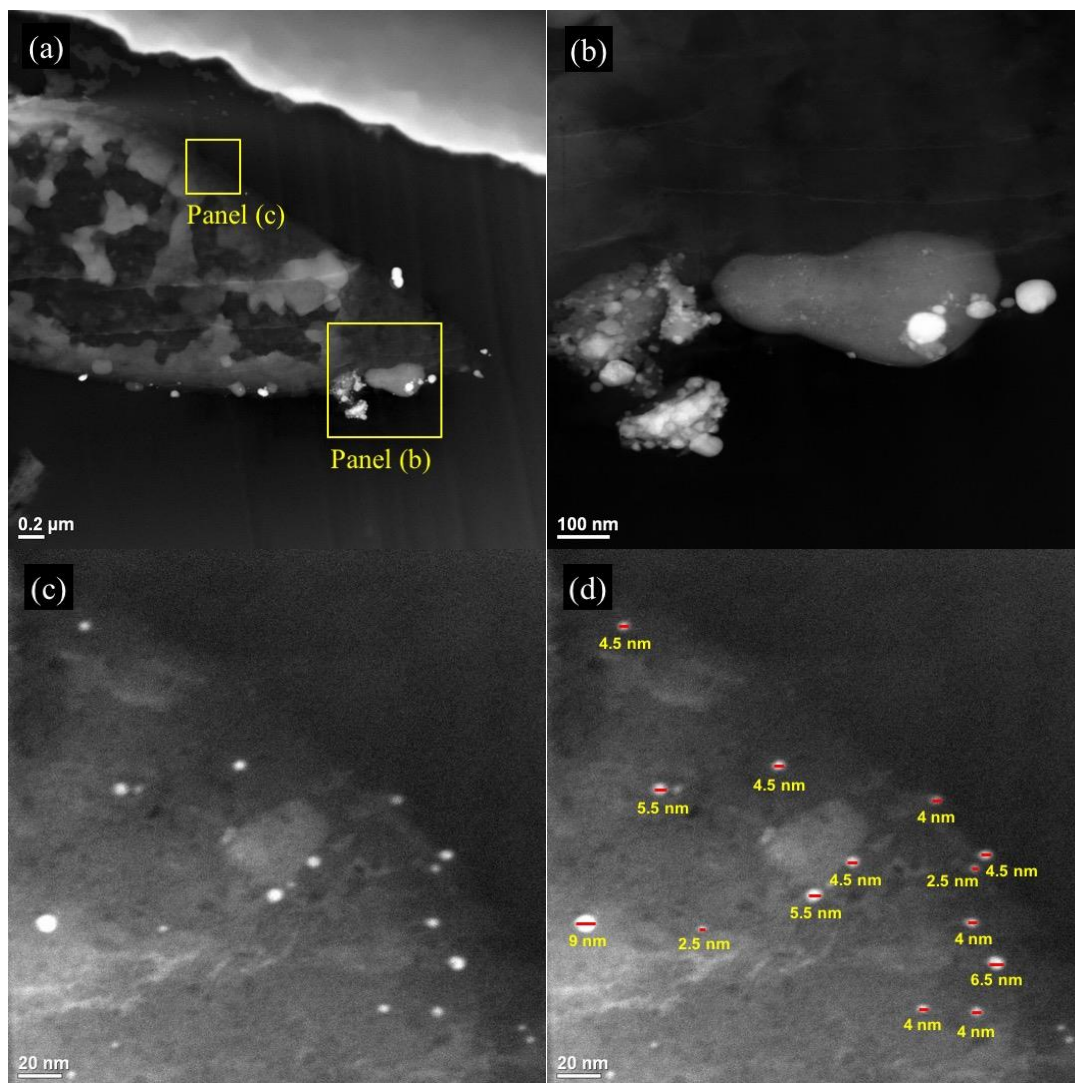
Figure 3.9   (a)–(c) Additional HAADF–STEM images of the microtomed cross-
section of the Ag/SRB particle at different magnifications. (d) Particle
size estimation of nAg in panel (c).
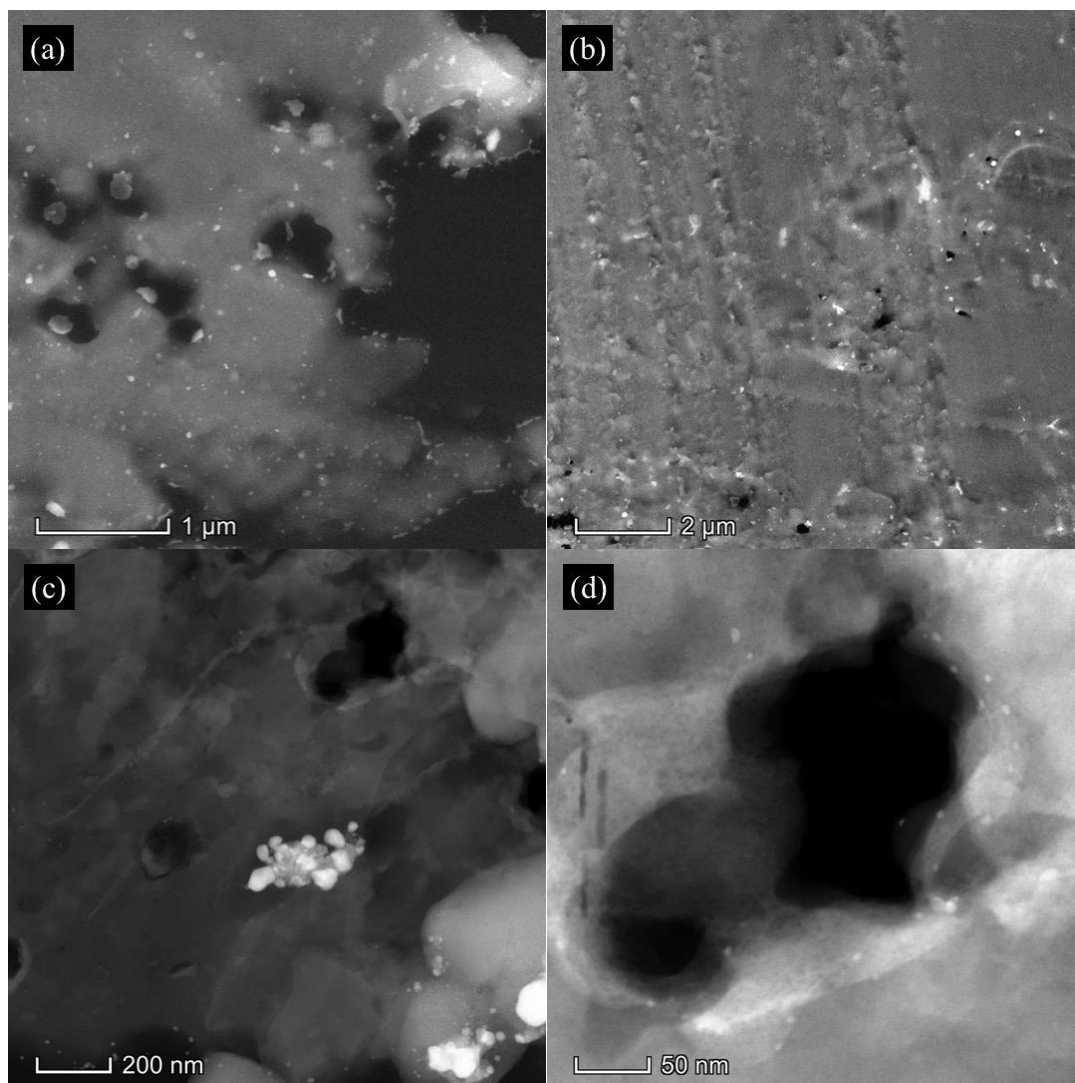
Figure 3.10 HAADF–STEM images showing nAg distribution and aggregation in large pores of SRB.

The number of Ag atoms in nAg particles of given sizes can be calculated (Table 3.2). Using the observed nAg distributions on SRB surface (SEM images, Figure 3.6) and in the interior (STEM images, Figures 3.8(d) and 3.9(d)) and assuming all particles were spherical, we calculated an nAg area density of 8.43×10^6 Ag^0/μm^2

SRB surface and a volume density of 3.98×10^7 $Ag^0/\mu m^3$ SRB. We then estimated the percent nAg on the surface of different size SRB particles (Table 3.3). The calculations agree reasonably well with the results in Figure 3.1(a), where approximately 87% and 34% of the total Ag^+ uptake was rapid and presumably occurred at/near the exterior surface of SRB. The calculation also explains the 22% of the ESC accessible to *G. metallireducens* [6], which is presumably the ESC at/near the surface of 250–500 μm SRB.

Table 3.2   Estimated numbers of Ag atoms in different size nAg.

nAg Diameter (nm)	No. of Ag Atoms	Electrons or ESC (in mmol)
1	31	5.15E-20
2	248	4.12E-19
3	838	1.39E-18
4	1987	3.30E-18
5	3881	6.44E-18
6	6707	1.11E-17
7	10650	1.77E-17
8	15897	2.64E-17
9	22635	3.76E-17
10	31050	5.16E-17

nAg were assumed to be spherical consisting of face-centered cubic unit cells with a cubic length of 0.407 nm.

Table 3.3   Estimated amounts of silver atoms (Ag^0) on the surface and in the interior of different size SRB particles.

SRB Size (µm)	Surface Ag^0 (mmol)	Interior Ag^0 (mmol)	Surface/Interior Ratio	Ag^0 on SRB Surface (%)
1	2.55E-12	3.46E-14	73.62	99
10	2.55E-10	3.46E-11	7.36	88
100	2.55E-08	3.46E-08	0.74	42
250	1.59E-07	5.41E-07	0.29	23
500	6.37E-07	4.33E-06	0.15	13

An area density of $8.43{\times}10^6$ $Ag^0/\mu m^2$ SRB geometric surface was estimated based on SEM images (Figure 3.6) and a volume density of $3.98{\times}10^7$ $Ag^0/\mu m^3$ SRB was obtained based on STEM images (Figures 3.8(d) and 3.9(d)). All SRB particles were assumed to be spherical for these calculations.

1.8   Conclusions and Environmental Implications

Using Ag^+ as a probe and nAg as a marker, the location and distribution of ESC on and within SRB were visualized through electron microscopy. Visual confirmation of the significant and ubiquitous ESC in the interior of SRB offers an explanation for the slow, pore diffusion-limited reactions of SRB and the incomplete accessibility of its ESC to *G. metallireducens* observed in previous studies [6, 70]. The high nAg (and thus ESC) density at/near the surface of SRB is also consistent with the rapid reactions in early times (Figure 3.1(a)). Our results show that almost half of ESC may reside in biochar interior and would take days to access even for 100-µm particles, and that fraction would increase with particle size. Knowing the spatial distribution and (bio)accessibility of ESC is crucial as it would guide the production and selection of biochar and other BC materials for targeted applications.

It has not escaped our attention that this method also represents a new approach to incorporate Ag, and potentially other redox-labile elements, onto/into

carbon materials. Ag loading as high as 30% by mass was achieved, which can be tuned by adjusting pH and reaction time. Given the antimicrobial and sorptive properties of silver and carbon, respectively, nAg-amended carbons can be effective media for simultaneous control of microbial and chemical contaminants [81, 87].

Chapter 4

ORIGIN OF ELECTRON STORAGE CAPACITY OF BLACK CARBON: PYROLYSIS OF LIGNOCELLULOSIC BIOMASS

This chapter is a shortened version of an articles: "Reprinted with permission from ACS Sustainable Chem. Eng. 2021, 9(19), 6821−6831. Copyright 2021 American Chemical Society."

1.9   Introduction

Black carbon is a collection of carbonaceous materials produced through natural or anthropogenic pyrogenic processes such as wildfires, deforestation, and incomplete fossil fuel combustion. [2, 27, 88, 89] As an integral part of the global carbon cycle, black carbon is ubiquitous in terrestrial and aquatic environments, influencing biogeochemistry and the fate and transport of contaminants. [2-4, 27, 88, 90] Biochar is a class of manmade black carbon produced through pyrolysis of surplus biomass under oxygen-limited conditions. [3, 4, 27, 91] Due to its stability, high surface area, and sorption capacity, [1, 2, 4] biochar has been proposed for a wide range of applications including carbon sequestration, [3, 88, 89] soil improvement, [4, 91] and environmental remediation. [66, 68, 92, 93]

Grass- and wood-derived biochars are reported to possess considerable electron storage capacity (ESC) [5]. Given the high annual production and ubiquity of black carbon in soil and sediment, [1, 2, 4] the discovery of ESC may have important implications for biogeochemistry and climate. For example, ESC may enable black carbon to serve as a terminal electron acceptor and redirect electron flow in anaerobic

ecosystems from methanogenesis to respiration, [72, 74] thereby suppressing CH4 production. In addition, ESC may greatly expand the applications of biochar, which can serve not only as a passive sorbent but a reactive medium that supports chemical and microbial redox transformation. [6] Such applications may include (1) (bio)degradation of contaminants, [10, 26, 27, 41, 44, 94, 95] (2) sequestration, storage, and reuse of metal(loid)s, [94, 96, 97] and (3) synthesis of biochar-metal composites. [98, 99]

Studies in recent years have shown that ESC is a property of biochars produced from lignocellulosic biomass such as wood, rice straw, and grass. [5, 8, 11-14, 41, 43, 100] The origin of this property, however, remains unknown. Biochar ESC may originate from the source biomass if the biomass itself possesses ESC that can survive pyrolysis. Alternatively, ESC may be generated during pyrolysis. In addition, it is unclear what plant component(s) contributes to ESC. Identifying the origin of biochar ESC is necessary to understand how ESC is controlled by biomass composition and/or pyrolysis conditions. This knowledge is essential for producing biochars that have desired properties to support redox-based applications.

Lignocellulosic biomass, the most widely used feedstock for biochar production, [91, 101] is essentially composed of three biopolymers: cellulose, hemicellulose, and lignin, along with variable amounts of extractives and minerals. [15] One approach to determine the origin of biochar ESC is to compare the ESC of the biopolymers and their corresponding biochars prepared at different pyrolysis temperatures. Furthermore, comparing the ESC of biochars produced from individual biopolymers, [102-106] their combination, [107, 108] and biomass consisting of these

biopolymers under identical conditions may permit estimation of each biopolymer's contribution to the ESC of biochar produced from lignocellulosic feedstocks.

In Chapter 4, experiments were designed to identify the origin of black carbon's ESC; i.e., is the ESC of black carbon leftover ESC of its lignocellulosic precursors, created during pyrolysis, or both? We first measured the ESC of the feedstocks, including three biopolymers and wood, using mediated electrochemical analysis (MEA) and their pyrolysis products at temperatures from 350 to 650 °C, using chemical redox titration (CRT). We then compared the ESC of biochars prepared from individual biopolymers and those from wood and biopolymer mixture pyrolyzed under the same conditions to assess whether ESC is an additive property. Finally, we used solid-state ^{13}C NMR (ss-NMR) to monitor the alternation of functionalities during the pyrolysis of wood and biopolymers.

1.10 Materials and Methods

1.10.1 Chemicals

Titanium(III) chloride (20% w/v, in 2 N HCl) and sodium citrate (99%) were acquired from Acros Organics (Fair Lawn, NJ). Sodium hydroxide (NaOH, 50%) and hydrochloric acid (HCl, 36.5-38%) solutions, potassium phosphate dibasic (K_2HPO_4, 99.4%), and potassium chloride (KCl, >99.0%) were obtained from Fisher Scientific (Pittsburgh, PA). 2,2-Azino-bis(3-ethylbenzothiazoline-6-sulfonic acid) diammonium salt (ABTS, 98%) and 1,1'-ethylene-2,2'-bipyridinium dibromide monohydrate (diquat, 95%) were purchased from Sigma-Aldrich (St. Louis, MO). Potassium phosphate monobasic (KH_2PO_4, 99.5%) was obtained from J.T. Baker (Phillipsburg, NJ). All chemicals were used as received.

1.10.2 Feedstocks and biochar

Three biopolymers —cellulose, xylan (an analog of hemicellulose), and lignin (alkali) —were purchased from Acros Organics. Pinewood (*Pinus taeda*), which is composed of 57.5%, 13.5%, 27.5%, and 1.5% of cellulose, hemicellulose, lignin, and ash, [109] respectively, was purchased from Lowe's retail shop (Athens, OH) and chopped with a power saw to obtain a particle size smaller than 1 mm. A biopolymer mixture sample was prepared by mixing the biopolymers according to the pinewood composition above normalized on an ash-free basis (i.e., 58.4% cellulose, 13.7% hemicellulose, and 27.9% lignin).

The three biopolymers, a pinewood sample, and the biopolymer mixture were individually pyrolyzed in a GCF Series controlled atmosphere muffle furnace (Livingston, NJ). Samples were pyrolyzed at four temperatures (350, 450, 550, and 650 °C) for 1 h under N_2 atmosphere at a flow rate of 2.0 L/min, following a three-stage process. First, the furnace was heated from an ambient temperature to 100 °C at 10 °C/min and kept at 100 °C for 5 min. The furnace was then heated to the set pyrolysis temperature at 20 °C/min, which was followed by a 60-min isothermal phase. Finally, the furnace was cooled to 200 °C at 20 °C/min by a built-in forced draft fan and allowed to cool naturally to room temperature.

The feedstock and biochar samples were labeled as C/X/L/W/M-T, where C, X, L, W, and M stand for cellulose, xylan, lignin, wood, and mixture of biopolymers, respectively, and T is pyrolysis temperature in °C. The feedstocks and corresponding biochars prepared in this work are summarized in Table 4.1.

Table 4.1   Summary of the feedstocks and corresponding biochars characterized.

Pyrolysis Temperature (°C)	–	350	450	550	650
Cellulose	**C**	C350	**C450**	C550	C650
Xylan	**X**	X350	**X450**	X550	X650
Lignin	L	L350	**L450**	L550	L650
Wood	W	W350	**W450**	W550	W650
Mixture of Biopolymers	M	M350	M450	M550	M650

M consisted of 58.4% cellulose, 13.7% xylan, and 27.9% lignin by mass. The ESC of feedstocks was measured by MEA, whereas the ESC of biochars was measured by CRT. The ESC of selected samples (**bold**) was measured by both MEA and CRT. Selected samples (underlined) were characterized by ss-NMR.

Prior to ESC measurement, all black carbon samples were individually dried at 65 °C for 24 h. Unless noted otherwise, each sample was ground at 4000 rpm for 3 min using a Beadbug 3 bead homogenizer with 3 mm zirconium beads filled in a tube (Benchmark Scientific Inc., Sayreville, NJ) and sifted to <53 μm. Each sample was oxidized individually with dissolved O_2 (DO) in continuously aerated deionized water to drain stored electrons, i.e., to bring the EDC to zero with respect to DO. Based on our preliminary ESC analyses, the biochar samples prepared in our laboratory (listed in Table 4.1) were oxidized for 72 h to ensure complete oxidation of reduced functional groups in those samples that were accessible and oxidizable by DO. The oxidized chars were then vacuum-filtered, dried, and stored in a desiccator before use.

1.10.3 ESC measurement of feedstocks by MEA

All MEA experiments were performed in an anaerobic glove box (Plas Labs, Lansing, MI). The EDC and EAC were determined using mediated electrochemical oxidation and reduction (MEO and MER), respectively. We used ABTS (ABTS/ABTS$\cdot^+$, E_h = +0.68 V vs. SHE) and diquat (diquat$\cdot^+$/diquat^{2+}, E_h = −0.36 V vs. SHE) as MEO and MER redox mediators, respectively. [34] A 40-mL glassy carbon

cylinder (HTW, Thierhaupten, Germany) served as the working electrode as well as a reaction vessel. A separate coiled platinum wire was applied as the counter electrode (Bioanalytical Systems, West Lafayette, IN) housed within a porous glass frit (Ace Glass, Vineland, NJ). Electrochemical potentials were controlled by a potentiostat (DropSens µStat 400, Metrohm, Herisau, Switzerland) and controlled from outside the glovebox by a Bluetooth connection. Reduction potential (E_h) was measured against the Ag/AgCl reference electrode and reported against SHE. The glassy carbon cylinder and porous glass frit, containing 36 mL of 100 mM KCl and 100 mM phosphate buffer at pH 7, were equilibrated to a predetermined reduction potential (+0.61 V in MEO and −0.49 V in MER). To initiate the experiment, a 1-mL mediator (~10 mM ABTS or diquat^{2+}) was spiked into the cell and the oxidative or reductive current peaks were recorded. After a constant background current was established, 500 µL of 1 g/L biopolymer, wood, or DO-oxidized char suspensions (500 µg) were spiked into the cell in sequence, resulting in current peaks. Each sample was spiked at least twice and the average and range of results from duplicates were reported. The MEO and MER current peaks were integrated over time to obtain the electrons transferred per gram of samples (Equation 4.1).

$$\text{e}^- \text{ transferred (mmol e}^-/\text{g)} = 1000 \times (\int \frac{\text{I}}{\text{F}} \text{dt}) / \text{m} \tag{4.1}$$

where F is Faraday constant (96485 A·s/mol), I is MEO/MER current (A), t is time (s), and m is sample mass (g).

1.10.4 ESC measurement by CRT

All ESC measurements by CRT were conducted in an anaerobic glove box (Coy, Grass Lake, MI) under 98±0.5% N_2 and 2.5±0.5% H_2, except when samples were oxidized by DO for assessing ESC reversibility. Ti(III) citrate, which has an E_h

of –0.36±0.01 V at pH 6.4, [59] and is negatively charged and does not adsorb to biochar, was used as the reductant to measure the EAC of DO-oxidized biochar. Given the EDC of DO-oxidized biochar is zero, as shown by the ESC reversibility study (below), the EAC of DO-oxidized biochar was taken to be the ESC. DO-oxidized samples were transferred into a glove box, deoxygenated under N_2/H_2, and reduced with 10 mM Ti(III) citrate solution (pH 6.4±0.2). The electron transferred from Ti(III) citrate to biochar was quantified based on the Ti(III) consumed (Equation 4.2), which was determined using the Beer-Lambert law and the extinction coefficient of 91.5±3.3 $M^{-1}cm^{-1}$ at 400 nm [59, 71] measured using a Vernier LabQuest 2 UV-vis spectrophotometer (Vernier, OR):

$$e^- \text{ transferred (mmol/g)} = EAC = ESC = [C_1V_1 - C_n \times (V_1 - \Sigma_i v_i) - \Sigma_i C_i v_i]/m$$

(4.2)

where C_1 and V_1 are initial concentration (mM) and volume (L) of Ti(III), respectively, C_n is final Ti(III) concentration (mM), v_i and C_i are volume (L) and Ti(III) concentration (mM) of aqueous sample withdrawn, and m is biochar mass (g) on a dry basis. Note that the CRT method with Ti(III) citrate and DO covers the ESC in the E_h range of –0.36 V to +0.80 V, whereas MEA covers a lower E_h range of −0.49 V to +0.61 V.

All ESC measurements were performed in duplicates. The average and range of results from duplicate measurements were reported. The electron transferred to a sample was taken to be at equilibrium with Ti(III) citrate solution when the values calculated from Equation 4.2 for two consecutive samples were statistically the same based on a Student's t-test ($P<0.05$). As in oxidation with DO, ESC measurements for biochars prepared in our laboratory (Table 4.1) were performed for 72 h since the electrons transferred at 48 h and 72 h were statistically the same.

After reduction, the biochar sample was collected on a glass microfiber filter, rinsed thoroughly with deionized water, and dried completely for another cycle of ESC measurement to assess the redox reversibility of ESC. The entire ESC measurement procedure was repeated two more times for the same biochar sample, each cycle consisting of DO oxidation and Ti(III) citrate reduction as described above.

pH was measured using an Oakton pH electrode and Oakton 11 series pH/mV/°C meter (Oakton Instruments, Vernon Hills, IL). E_h of Ti(III) citrate solution was measured before and after each experiment using an Oakton Pt ORP electrode. The ORP electrode was calibrated periodically against the Zobell's solution (+0.42 V vs. SHE at 25 °C).

1.10.5 Prediction of biochar ESC from biomass composition

The ESC of biochars from wood (W) or biopolymer mixture (M) were predicted based on the ESC of biochars from individual biopolymer (ESC_{i-T}) and the mass fraction of each biopolymer (w_{i-T}) in the biochar, as shown in Equation 4.3:

$$ESC_{P-T} = \sum_i w_{i-T} \times ESC_{i-T} = w_{C-T} \times ESC_{C-T} + w_{X-T} \times ESC_{X-T} + w_{L-T} \times ESC_{L-T}$$

$$(i = C, X, or\ L)(4.3)$$

where ESC_{P-T} is the predicted ESC for biochars derived from W or M prepared at pyrolysis temperature T.

The mass fraction of each biopolymer w_{i-T} in W or M biochar was calculated from the initial biopolymer composition and the yield of biochar produced from each biopolymer, as shown in Equation 4.4:

$$w_{i-T} = \frac{w_{i0} \times Y_{i-T}}{\sum_i w_{i0} \times Y_{i-T}} = \frac{w_{i0} \times Y_{i-T}}{w_{c0} \times Y_{c-T} + w_{X0} \times Y_{X-T} + w_{L0} \times Y_{L-T}} \quad (i = C, X, or\ L)(4.4)$$

where w_{i0} is the initial mass fraction of each biopolymer in W or M; Y_{i-T} is the yield of biochar from biopolymer i at pyrolysis temperature T.

Biochar mass yields of W or M were predicted using Equation 4.5:

$$Y_{P-T} = \sum_i w_{i0} \times Y_{i-T} \quad (i = C, X, \text{ or } L) \quad (4.5)$$

where Y_{P-T} is the predicted biochar yield of W or M.

1.10.6 Proximate analysis, ultimate analysis, and solid-state ^{13}C-NMR spectroscopy

1.10.6.1 Proximate analysis

Proximate analysis was conducted for biopolymers and wood. Proximate analysis, i.e., assessment of the content of volatile matter, fixed carbon, and ash, was performed by thermogravimetric analyses (TGA) using TGA Q500 from TA Instruments (New Castle, DE). The sample heating rate and gas flow rate were set at 20 °C/min and 50 mL/min, respectively. A nitrogen atmosphere was used for determining the volatile matter. Samples were heated from 25 to 105 °C and held at 105 °C for 5 min, and then heated to 900 °C and held at 900 °C for another 5 min. To further determine fixed carbon and ash contents, the air was introduced to combust the remaining sample at 900 °C for 10 min. Mass remaining at the end of the combustion process was taken to be ash, and fixed carbon was obtained by subtracting volatile and ash contents from 100%.

1.10.6.2 Ultimate analysis

Ultimate analysis was conducted for all samples and the composition of biochars derived from W and M was predicted in the same way as for ESC in Equation 4.3. Carbon, hydrogen, nitrogen, sulfur, and oxygen contents were determined for ultimate analysis using a Flash 2000 Organic Elemental Analyzer from Thermo Scientific (Waltham, MA). Cystine sulphanilamide methionine BBOT was used as a calibration standard and vanadium oxide (V_2O_5) was used as a conditioner.

Fully dried samples were combusted at around 960 °C in ultra-high purity oxygen and passed through copper oxide pellets and then electrolytic copper with a helium carrier gas. The gases were then analyzed by a thermal conductivity detector (TCD). The detection limits for nitrogen and sulfur were 1.6% and 1.8%, respectively. Oxygen content was calculated by subtracting carbon, hydrogen, nitrogen, and sulfur from 100%.

Based on the elemental composition, mole ratios of O/C and H/C were calculated. In addition, aromaticity index (AI), which is a measure of C=C double bond density, [110] was calculated based on Equation 4.6.

$$AI = \frac{1+[C]-[O]-[S]-0.5[H]}{[C]-[O]-[S]-[N]} \text{ (If AI<0, then AI=0) (4.6)}$$

where [element] is the mole content of the element in feedstock or biochar.

1.10.6.3 Solid-state ^{13}C-NMR spectroscopy

ss-NMR was applied to characterize selected samples (Table 4.1) including feedstocks and biochars. ss-NMR is a powerful tool for investigating complex environmental samples, as it enables nondestructive, comprehensive, and quantitative analyses of intact solid samples such as plant materials and biochar. [111] The advanced multiple cross-polarization (CP) is a new and robust quantitative ^{13}C technique for the characterization of unlabeled solids with at least 50 times shorter measurement time yet uncompromised sensitivity than previously achieved in direct-polarization NMR. [112] The multiple CP ss-NMR with ramp CP at 14-kHz MAS has been successfully validated for plant matter, humic acids, and biochar. [112, 113]

NMR spectra were collected on a Bruker AVIII 500 MHz spectrometer (Billerica, MA) with a 4mm HX probe at a spinning speed of 14 kHz and frequency of

125.770 MHz. Multiple CP magic angle spinning (MAS) was used to obtain quantitative peak intensities with a total CP time of 10.45 ms and a repolarization delay of 125 ms between CP blocks. 3328 scans were acquired over 4 h with a recycle delay of 2 s. We also ran 19968 scans over 24 h for selected samples and observed no discernible difference in the relative content of functional groups (data not shown). All sample spectra were calibrated to a glycine external standard. Two reference compounds, 1,4-benzoquinone (BQ) and 1,4-hydroquinone (HQ), were added to confirm shift ranges of (hydro)quinoic functional groups in samples (Figure 4.1). ss-NMR spectra were baseline-corrected, divided into chemical shift ranges of carbon functional groups typical of biochar [113], and peak integrated using MestreNova (Mestrelab Research S.L., A Coruña, Spain).
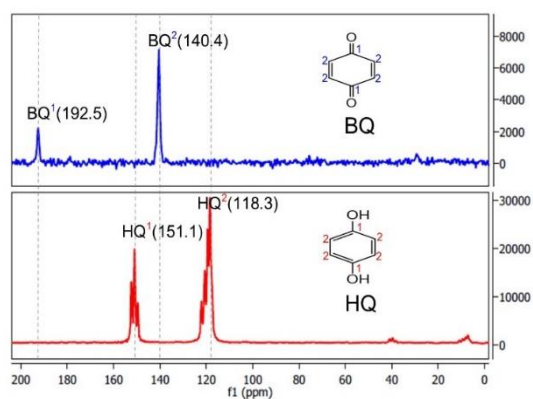
Figure 4.1   ss-NMR spectra of reference compounds including BQ and HQ

1.11 Results and Discussion

1.11.1 ESC of biopolymers

The EDC and EAC of the three biopolymers and ground pinewood chips measured by MEA are shown in Figure 4.2. Cellulose and xylan contained negligible EDC or EAC, which is not surprising since cellulose and xylan are polysaccharides of D-glucose and xylose, respectively, and do not contain redox-labile functional groups. In contrast, lignin, which is comprised mainly of cross-linked polymers of p-hydroxyphenyl, guaiacyl, and syringyl units, possessed a significant EDC of 3.22 mmol e$^-$/g and a modest EAC of 0.49 mmol e$^-$/g. These results are consistent with those reported by Klüpfel et. al. [5], who showed the EDC and EAC of cellulose measured by MEA were below detection, whereas the EDC and EAC of lignin were 4.32 and 0.25 mmol e$^-$/g, respectively. The heterogeneous molecular structure of lignin and the methods used to extract lignin may account for the different values. For example, through wavelength dispersive X-ray fluorescence spectrometry (WDXRF) and elemental analysis we identified sulfur and iron in lignin (Sections A2–A3), and the sulfur content was sufficiently high to have affected the EDC value. Nonetheless, our result confirms that lignin is the only biopolymer that could contribute to the ESC of lignocellulosic biomass.

The wood sample possessed 0.12 mmol e$^-$/g of EDC and 0.16 mmol e$^-$/g of EAC (Figure 4.2). Given the pinewood was composed of predominantly the three biopolymers with minimal ash (Table A.2), its ESC could have been derived from lignin. Based on its 27.5% lignin content, the wood sample could possess an EDC and EAC of up to 0.89 and 0.13 mmol e$^-$/g, respectively. The lower EDC of wood may be

due to either differences between commercial and natural lignin or different accessibility and/or reactivity of the lignin in wood.

Interestingly, DO-oxidized lignin gave virtually the same EDC (3.37 mmol e^-/g) and EAC (0.40 mmol e^-/g) as non-oxidized lignin. This indicates that DO was unable to oxidize the electron-donating functional groups in lignin that the oxidized form of ABTS (i.e., the $ABTS^{\cdot+}$ radical) could oxidize, despite the fact that the E_h of aerated water (+0.80 V) is higher than the set potential (+0.61V) for MEO. In other words, the EDC of lignin measured by MEO was entirely due to the greater reactivity of $ABTS^{\cdot+}$ than that of O_2, even though ABTS operated at a lower potential. This result suggests that the EDC of lignin consisted of not hydroquinones or catechols (both of which can be oxidized by O_2) but predominantly phenolic groups, [114] which are abundant in lignin and could be readily oxidized by $ABTS^{\cdot+}$ but not O_2. [36, 115] In addition, the result suggests that measured EDC and EAC are to some extent operational, in that their values may depend on not merely thermodynamics (e.g., E_h) but also the reaction mechanism specific to the oxidant or reductant used.
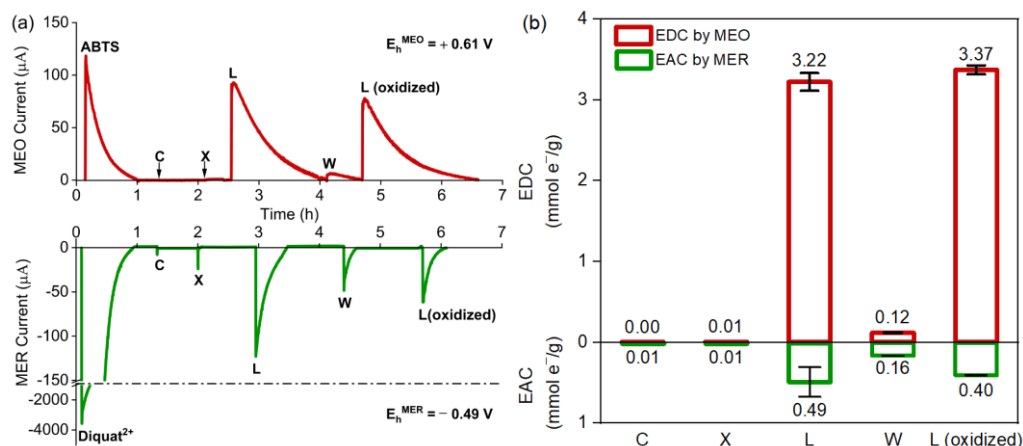
Figure 4.2   (a) MEO and MER current peaks of feedstocks. 500 μg each of cellulose, xylan, and lignin, wood, and DO-oxidized lignin (noted as "L (oxidized)"), spiked individually in sequence into an electrochemical cell for EDC and EAC measurements, respectively. Every sample was injected twice to confirm reproducibility and one set of the peaks is shown. (b) Summary of the EDC and EAC of feedstocks measured using MEO and MEA, respectively.

We also attempted to measure the ESC of biopolymers by CRT using Ti(III) citrate. As expected, DO-oxidized cellulose and xylan did not consume Ti(III) citrate (Figure 4.3), confirming that cellulose and xylan do not possess any ESC. Unfortunately, CRT with Ti(III) citrate cannot be applied to lignin because lignin absorbs strongly at 400 nm, which hinders the quantification of either Ti(III) citrate or lignin.
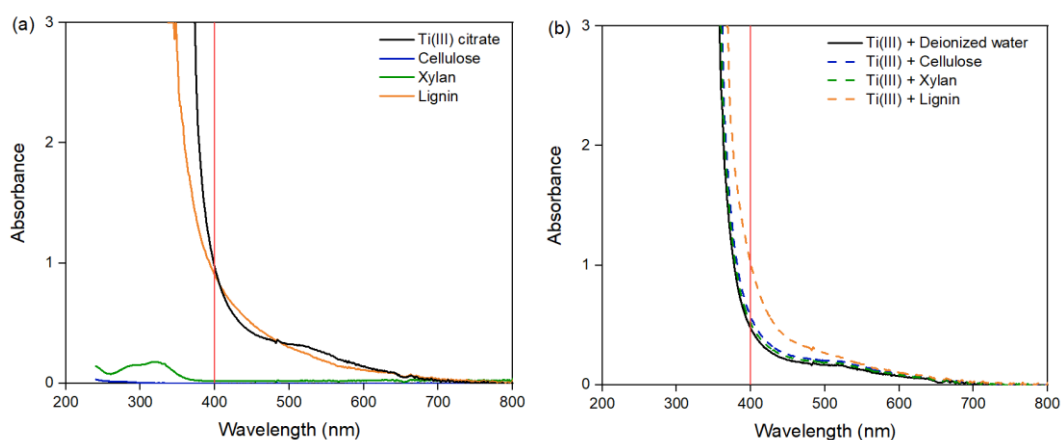
Figure 4.3   (a) UV-vis spectra of 10.6 mM Ti(III) citrate, 1 g/L DO-oxidized cellulose, 1 g/L DO-oxidized xylan, and 0.25 g/L DO-oxidized lignin. (b) UV-vis spectra of solutions containing 5mL of 10.6 mM Ti(III) citrate mixed with 5mL of deionized water, 1 g/L DO-oxidized cellulose or xylan, or 0.25 g/L DO-oxidized lignin.

1.11.2 ESC of biochars

Figure 4.4(a) shows the ESC of biochars prepared by individually pyrolyzing three biopolymers and wood at four temperatures (350–650 °C). All samples were measured by CRT with Ti(III) citrate and DO. Although the polysaccharides (cellulose and xylan) and lignin have very different ESC, once pyrolyzed, all three biopolymers possessed comparable and highly reversible ESC, ranging from 0.5 to 2.0 mmol e$^-$/g. Since cellulose and xylan contained no ESC, these results suggest that the ESC of cellulose- and xylan-derived biochars were created entirely through pyrolysis. In contrast, the ESC of lignin decreased by almost 90%, from 3.71 to 0.40 mmol e$^-$/g, after pyrolysis at 350 °C. This suggests that most of the original ESC of lignin was destroyed during pyrolysis at temperature $\leq$ 350 °C. In fact, given that the ESC of L350 was similar to that of C350 and X350, it is plausible that some or all of the 0.40 mmol e$^-$/g ESC was also created through pyrolysis. This is further supported by the

ESC reversibility result using DO and Ti(III) citrate. Recall that DO did not affect the EDC of lignin since DO could not oxidize the phenolic groups in lignin. The fact that the ESC of L350 was fully reversible over three redox cycles (Figure 4.4(a)) indicates that DO completely depleted the EDC of L350 measurable by CRT, and therefore the electron-donating groups in L350 must be different from those in lignin and thus could not have been leftover EDC of lignin that survived pyrolysis at 350 °C. At higher pyrolysis temperatures (450–650 °C), the ESC of all biopolymer chars increased further, to 1.0–1.5 mmol e$^-$/g for cellulose and xylan chars and 1.0–2.0 mmol e$^-$/g for lignin chars, while the char yields decreased (Figure A.2(a)). This indicates that, at pyrolysis temperatures above 350 °C, a greater number of redox-active functional groups was created per unit biochar mass for all biopolymers. For pinewood, the ESC of 0.28 mmol e$^-$/g was destroyed at 350 °C, and ca. 1 mmol e$^-$/g of new ESC was created at 450–650 °C. These results again support the ESC of wood and biopolymer biochars were created entirely through pyrolysis, rather than preserved from the original ESC of wood or lignin.

The ESC of biochar has been attributed to (hydro)quinone groups, which undergo facile and reversible redox reactions. [5, 72] Consistent with this, Figure 4.4(a) shows that all ESC created through pyrolysis was highly rechargeable. For biopolymer chars, the measured ESC from the second cycle (closed circle) was more than 80% of that from the first cycle, and the ESC from the third cycle (open circle) was statistically the same as from the second based on a Student's t-test (two-tailed, P<0.05), except for C650. For wood biochars, reversibility of the ESC was lower but still above 60% over three redox cycles, confirming the highly rechargeable nature of

biochar ESC. This result suggests that plant-based biochars can undergo recurrent redox transformation over repeated oxic-anoxic oscillations. [116, 117]

The hypothesis that ESC is created through pyrolysis is supported by changes in elemental composition and functionalities during the pyrolysis of biopolymers and wood. Figure A.2 shows that mass loss increased with pyrolysis temperature and was most significant at below 350 °C for all biopolymers. In addition, the aromaticity index (AI), a proxy for the development of condensed ring structures, was above the condensation threshold (AI=0.67) [110] for all biochars. These results indicate that at temperatures below 350 °C, biopolymers underwent structural transformation and developed characteristics of biochar, including ESC. To further understand the structural changes of biopolymers and ESC creation during pyrolysis, feedstocks and selected biochar samples were characterized using ss-NMR with signal enhanced by multiple cross-polarization. As shown in Figure 4.5 and Table 4.2, the biopolymers exhibited distinct NMR spectra, illustrating their compositional differences. Cellulose and xylan consist only of alkyl carbons (>98% C in 45–110 ppm), whereas lignin contains a variety of aromatic and aliphatic carbons, as revealed by the broad spectra. The high aromatic content and the peak in the O-aryl-C region (e.g., phenolic groups) are consistent with the high EDC of lignin. [36, 114, 115] The NMR spectra of wood appear to be a combination of the spectra of the biopolymers, as previously reported. [69] Once pyrolyzed, all materials lost their original features and displayed a unimodal NMR spectrum, characteristic of biochar. [69] While no aryl-C was observed for cellulose and xylan, aryl-C represented ca. 64% C in C450 and X450 (Table 4.2). Likewise, the aryl-C contents in lignin and wood significantly increased after pyrolysis, resulting in 73% and 60% aryl-C in L450 and W450, respectively. These

changes in ss-NMR spectra due to pyrolysis confirm the molecular transformation of biopolymers and wood and the creation of new structural moieties in the resulting biochars, all of which possessed comparable ESC. If the redox moieties created that composed biochar ESC were indeed (hydro)quinones, given that pyrolysis was carried out under pure N_2, the oxygen in the (hydro)quinone groups must have been derived from the biopolymers. Hence, O_2 is not necessary for ESC creation from lignocellulosic biomass.

To further compare MEA and CRT methods and verify the results with ESC measurement of SRB in Chapter 2, we also used MEA to measure the ESC of DO-oxidized biochars prepared from biopolymers and wood at 450 °C (Figure 4.4(b)). As observed with SRB, the ESC measured by MEA ranged from 4% (W450) to 42% (L450) obtained by CRT, confirming that MEA could access only a fraction of the ESC of biochar. Since we pre-oxidized these biochars with DO, their EDC measured by CRT would be zero. This was the case for the other chars when measured by MEA, but not L450, which showed a small but measurable EDC of 0.27 mmol e⁻/g. A small, non-zero EDC was also observed for DO-oxidized SRB (Chapter 2, Figure 2.12(a)). These results suggest that, while most phenolic groups in lignin were destroyed at temperature below 350 °C, a small fraction could survive even 450 °C (L450) and 550 °C (SRB). This fraction is reactive toward ABTS·⁺ but not DO, and thus contributes to the EDC measured by MEA but not CRT. That is, the 0.27 mmol e⁻/g (hollow red bar for L450) is not part of the 2.04 mmol e⁻/g (solid orange bar) in Figure 4.4(b). Therefore, ESC obtained by MEA with ABTS would be larger than that obtained by CRT with DO/Ti(III) if a sample contains phenolic and other functional groups that are oxidizable by ABTS·⁺ but not O_2.
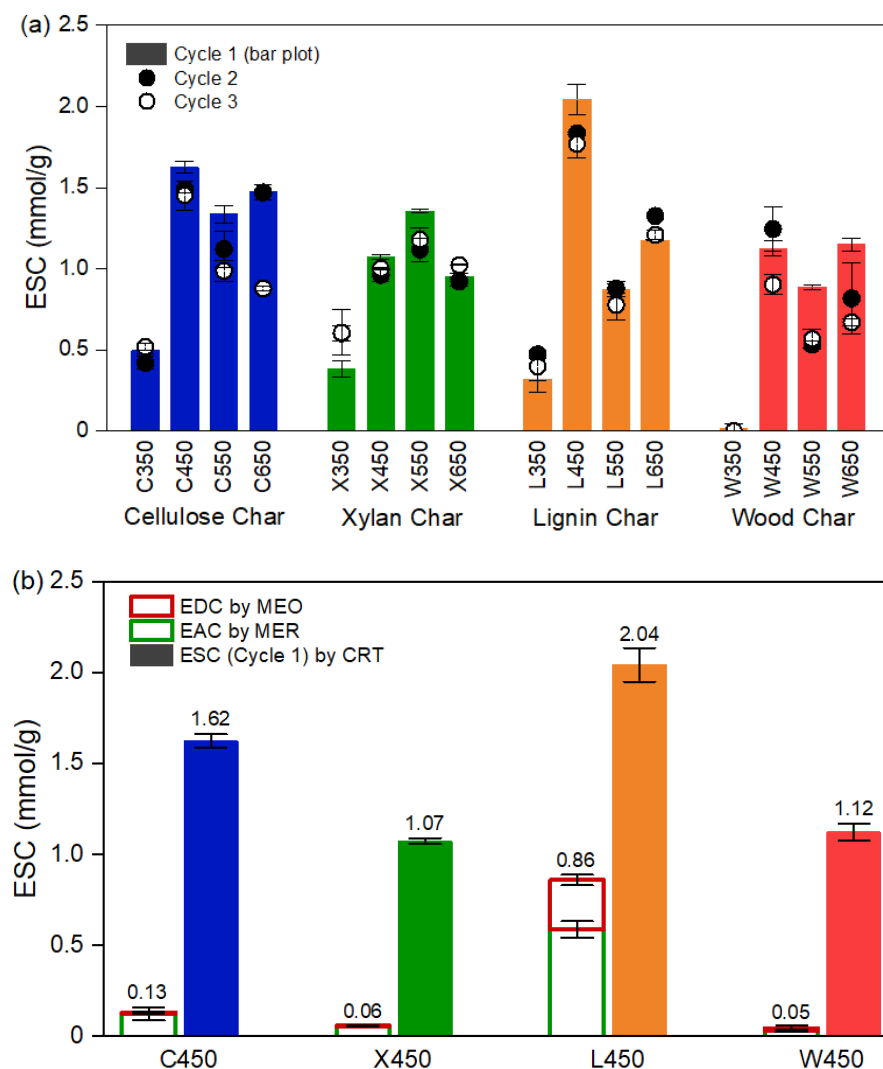
Figure 4.4   (a) ESC of biochars prepared at 350, 450, 550, and 650 °C. All ESC was measured by CRT with Ti(III) citrate. Solid bars, closed circles, and open circles represent ESC results from the first, second, and third cycle CRT, respectively. (b) Comparison of ESC of biochars derived from cellulose, xylan, lignin, and wood pyrolyzed individually at 450 °C, measured by MEA and CRT. Numbers represent total ESC (EDC+EAC). The EDC of L450 measured by MEO (hollow red bar) was 0.27 mmol e⁻/g; the EDC of other biochar was <0.02 mmol e⁻/g.
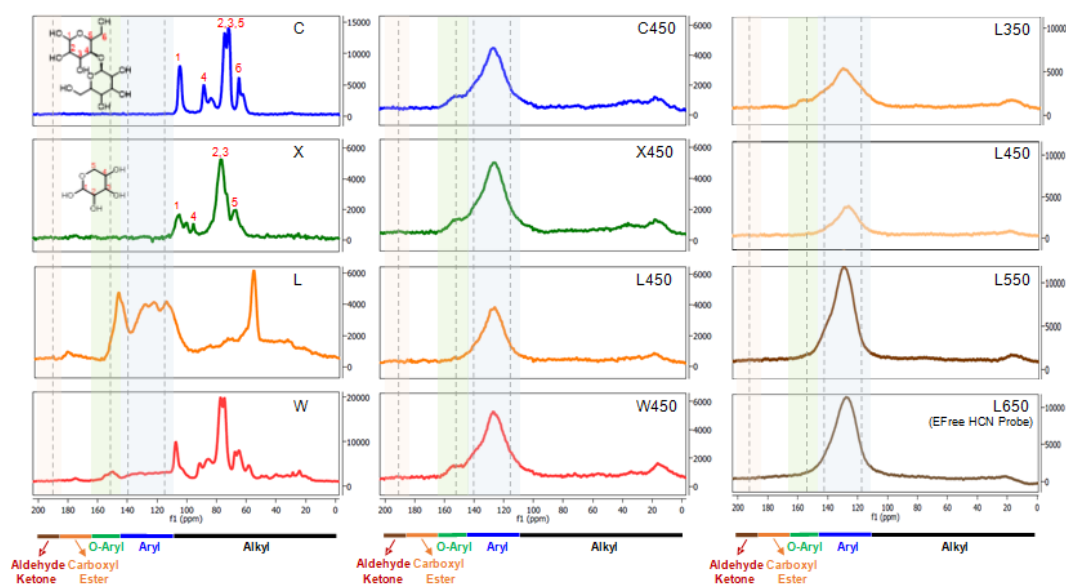
Figure 4.5   ss-NMR spectra of feedstocks (cellulose, xylan, lignin, and wood), biochars prepared at 450 °C, and biochars derived from lignin at different pyrolysis temperatures. The regions of carbon groups that are potentially redox-active, namely aldehyde/ketone-C, O-aryl-C, aryl-C, are shaded using different background colors and the peak positions of two reference compounds (BQ and HQ, Figure 4.1) are specified in dotted vertical lines.

Table 4.2   Carbon content (%) of functional groups in feedstocks and biochars
calculated from ss-NMR spectra (Figure 4.5)

Sample	Carbonyl-C		Total Aryl-C		Alkyl-C			
	220-184 ppm	184-165 ppm	165-146 ppm	146-110 ppm	110-90 ppm	90-45 ppm	45-20 ppm	20-0 ppm
	Aldehyde/Ketone $RC=O$	Carboxyl /Ester RCOOR	Oxygenated Aromatic Ar-OR	Aromatic $C=C$/Ar-C-H	Dioxygenated Alkyl RO-C-OR	Oxygenated Alkyl RCH_2-OR	Methylene CH_2	Methyl CH_3
C	0.00	0.12	0.00	0.00	18.22	81.29	0.38	0.00
X	0.29	0.27	0.00	0.00	19.52	79.16	0.76	0.00
L	1.14	2.05	6.91	41.52	8.58	26.97	9.89	2.94
W	0.00	0.00	1.23	7.83	13.71	74.05	3.18	0.00
C450	2.25	2.21	8.20	55.95	5.96	9.29	9.68	6.46
X450	2.23	1.99	7.85	56.47	5.94	9.56	9.42	6.55
L450	0.00	1.21	3.65	68.86	5.18	8.22	7.73	5.14
W450	3.28	2.85	7.84	52.39	7.09	10.31	7.56	8.68
L350	6.22	4.60	9.52	44.25	6.97	12.07	8.95	7.42
L550	4.48	3.61	6.60	61.55	5.31	9.23	4.57	4.64
L650	5.99	4.44	7.17	60.61	6.81	8.86	4.85	1.27

1.11.3 ESC prediction for wood-derived biochars

To assess the extent to which the ESC of biochar derived from lignocellulosic biomass can be explained by the composition of its source biomass, we prepared a mixture of biopolymers based on the composition of the pinewood and measured the ESC of corresponding biochars. We also calculated the ESC of biochar derived from wood or mixed biopolymers using the mass fractions of biopolymers and their individual ESC created under the same conditions.

Figure 4.6(a) shows the measured and predicted ESC for wood and mixed biopolymer chars at four different temperatures. The measured ESC of biochars from the mixed biopolymers ranged from 0.5 to 1.5 mmol e⁻/g and exhibited a temperature dependency similar to that for wood biochars. This similarity supports the postulate that the ESC of biochar from lignocellulosic biomass is derived from its constituent biopolymers through pyrolysis. The contribution of lignin to the ESC was similar to or

higher than that of cellulose (Figure A.4(a)) because the biochar yield of lignin was much higher, even though lignin was less abundant than cellulose.

When predicted ESC are plotted against measured ESC (Figure 4.6(b)), the slopes for both wood biochars and mixed biopolymer biochars are close to 1, suggesting proportionality between measured and predicted ESC. However, most data are above the 1:1 line, indicating we over-predicted measured ESC. The deviations are greater for wood biochars, as indicated by the larger intercept (0.36) than for mixed biopolymer biochars (0.13), possibly due to the cellular structure of wood and/or its larger size (<1 mm for wood vs. <100 μm for biopolymers). The deviations in biochar yield are also greater for wood than for biopolymers: While the predicted and measured yields were practically the same for the biopolymer mixture, the predicted biochar yields were almost 9% higher for wood (Figure 4.6(c)). These differences notwithstanding, all wood biochars prepared at 450–650 °C possessed an ESC of 1.0–1.5 mmol e$^-$/g, similar to those predicted and measured from individual biopolymers and their mixture, supporting that, through pyrolysis, biopolymers contribute additively to the formation of biochar ESC.
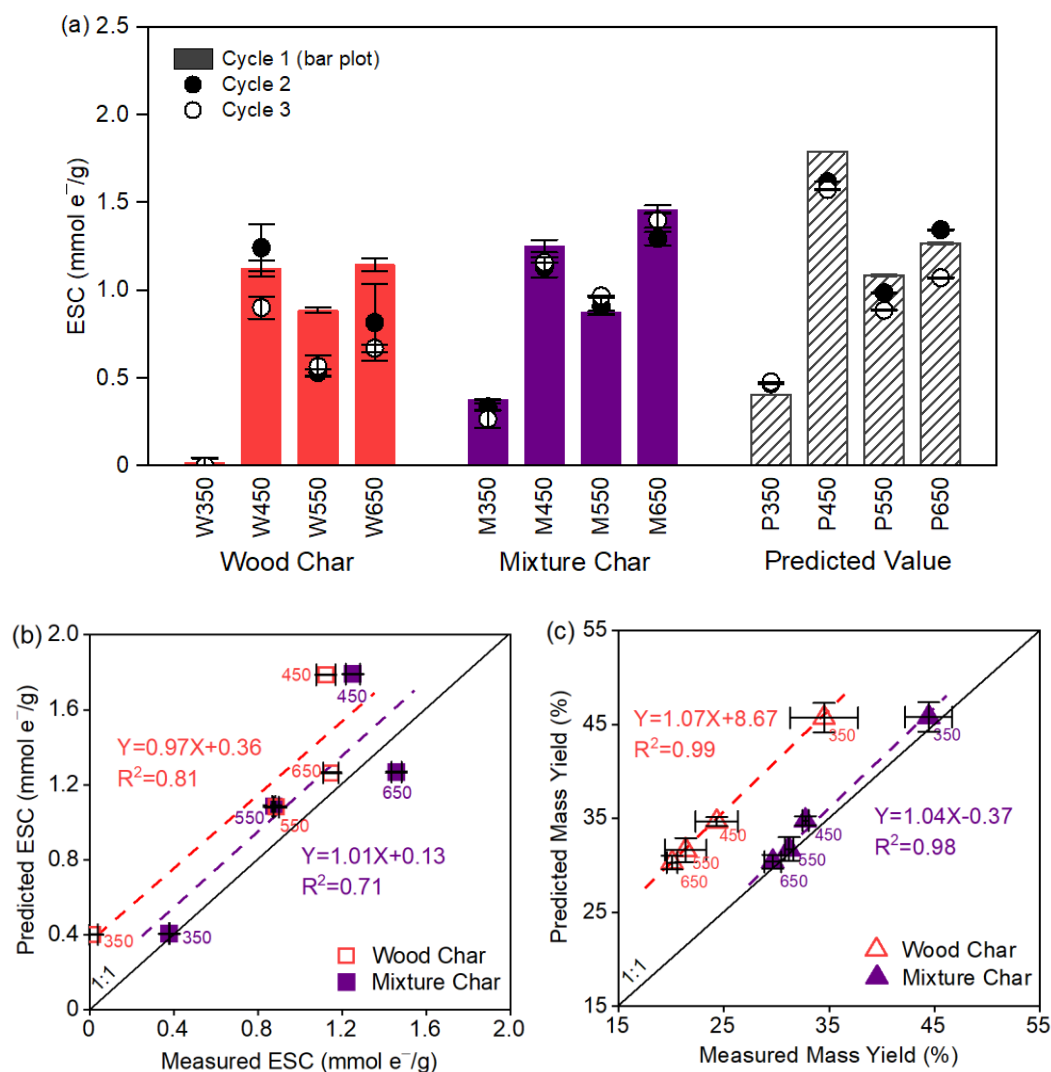
Figure 4.6   (a) Measured ESC of biochars made from wood and biopolymer mixture and predicted ESC of these biochars based on the yield and ESC of biochars from individual biopolymers. Solid bars, closed circles, and open circles represent ESC results from the first, second, and third cycle CRT, respectively. (b) Comparison of measured and predicted first cycle ESC for wood chars and biopolymer mixture chars. (c) Comparison of measured and predicted mass yield for biopolymer mixture chars and wood chars.

1.12 Conclusions

Cellulose, hemicellulose, and lignin make up over 90% and 60–80% of woody biomass and herbaceous biomass, respectively, [118] which are predominant source materials of biochar and other pyrogenic black carbon. The finding that the ESC of biochar originates from biopolymers through pyrolysis suggests that ESC is a common property of plant-based black carbon. This is also consistent with the results shown in Figure 4.7 (reproduced from Figure 2.13 in Chapter2). These biochars were all produced from lignocellulosic biomass. The wide range of ESC of different wood biochars suggests that pyrolysis conditions are critical for ESC creation. Pyrolysis created ESC of $\leq$2 mmol e$^-$/g in laboratory-prepared biochars under pure N_2 (Figures 4.4(a) and 4.6(a)), most likely by converting oxygen in (hemi)cellulose and lignin into that in (hydro)quinones, since there was no external source of oxygen. In contrast, pyrolysis created ESC of 3–7 mmol e$^-$/g in multiple commercial biochars. Given that ESC would only decrease outside the temperature range of 350–650 °C [5, 41], the comparison strongly suggests that additional ESC must have been created in commercial biochars, not by varying temperature but by incorporating O_2 through exposure to air during pyrolysis.

W-H220 is a hydrochar sample produced through hydrothermal carbonization of the same pinewood used in this work. [100] Although W-H220 has been reported to possess abundant oxygen containing functional groups, [100] it did not possess any ESC. After W-H220 was pyrolyzed at 400 to 600 °C, the resulting biochars had ESC of 2.0–3.5 mmol e$^-$/g, again confirming ESC was created via pyrolysis. Interestingly, these ESC are more than two times higher than those created by direct pyrolysis of the same wood in the similar temperature range (350-650 °C). This suggests that, while unable to create ESC itself, hydrothermal pretreatment may promote ESC creation

during pyrolysis, and hence hydrochars may yield greater ESC than their wood precursors.

We also analyzed two wood char samples from the California wildfires in 2019 by CRT. The ESC of the wildfire chars were 1.0 mmol e⁻/g and 0.2 mmol e⁻/g, within the range of ESC of the wood biochars in Figure 4.4(a). These data, while limited, suggest the universality of ESC in pyrolyzed lignocellulosic biomass, produced from both anthropogenic and natural processes. In summary, results in Chapter 4 demonstrate that pyrolysis is an ESC-creating process and that ESC is a property common to all pyrogenic black carbon from lignocellulosic biomass.
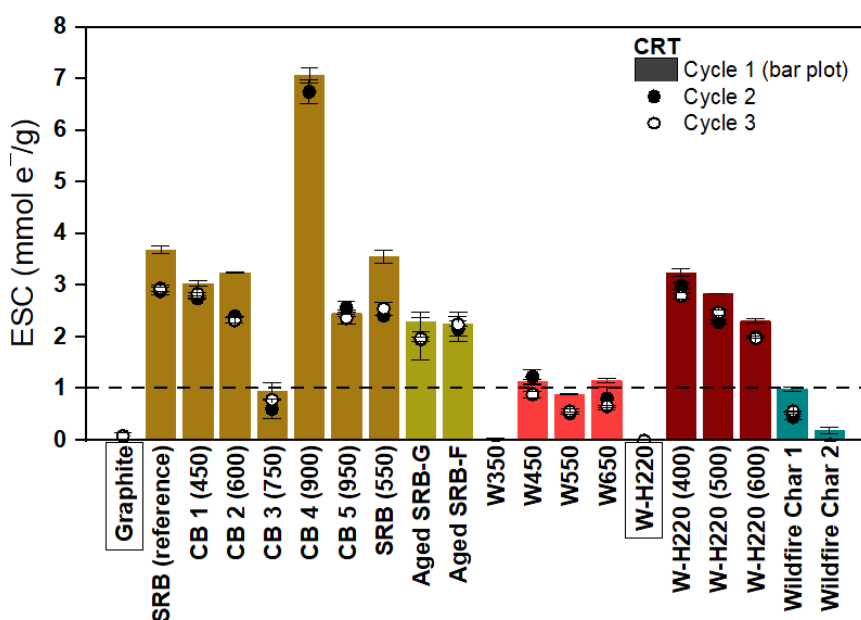
Figure 4.7   (Reproduced from Figure 2.13(a)) ESC of black carbon measured by CRT with Ti(III) citrate and DO. All black carbon samples had a particle size <53 µm. "CB" stands for commercial biochar and numbers in parenthesis represent pyrolysis temperature. Two black carbon samples, Graphite and W-H220, were not produced through pyrolysis.

Chapter 5

ABIOTIC REDUCTION OF MUNITIONS COMPOUNDS BY BIOCHAR THROUGH ITS ELECTRON STORAGE CAPACITY

1.13 Introduction

With the production, storage, and phase-in of insensitive munitions constituents (MCs), the contamination of insensitive MCs has become widespread in soils and groundwater at/near military sites across the U.S., posing environmental and health threats. [119-122] 3-Nitro-1,2,4-triazol-5-one (NTO), nitroguanidine (NQ), and 2,4-dinitroanisole (DNAN) are the three major constituents of the insensitive munitions explosive IMX-101 formulation; NTO and DNAN are also the main constituents of the IMX-104 formulation, along with a legacy MC– hexahydro-1,3,5-trinitro-1,3,5-triazinane (RDX). Although insensitive MCs are more stable and less prone to unintentional detonation than legacy MCs, they are more water-soluble and hence highly leachable in the environment. [119, 120] For example, the solubility of NTO is 16,642 mg/L (at 25 °C), which is >250 times higher than that of RDX (60 mg/L, at 25 °C). [123] Insensitive MCs can be mobilized during storm events and may exist at elevated concentrations in surface runoff from active ranges. There is a need to develop effective and inexpensive materials that can be used in stormwater treatment systems to remove and/or degrade insensitive MCs in DoD testing sites and training ranges.

Biochar is a type of black carbon produced through the pyrolysis of surplus biomass. [124] Owing to its high specific surface area, biochar has been widely

applied as a sorbent for removing hydrophobic organic contaminants including dyes, pesticides, pharmaceuticals [66], as well as MCs such as 2,4,6-trinitrotoluene (TNT) and RDX [125, 126],. However, biochar may not be an effective sorbent for insensitive MCs as they are much more hydrophilic than legacy MCs. Notably, the anionic nature of NTO at circumneutral pH (pK_a=3.76) [127, 128] would aggravate the effectiveness of its sorption by biochar.

Once considered chemically inert, biochar is now found to be capable of mediating redox reactions, i.e., exchanging electrons, through at least two mechanisms: conduction [18, 22, 23] and electron storage capacity (ESC) [5, 6]. The first mechanism, i.e., conduction, requires the presence of an external electron donor in situ, in which the electrons are transferred from the external electron donor to an electron acceptor, e.g., a contaminant, though conductive graphitic domains of biochar [23, 31]. A previous study has reported that the reduction of 2,4-dinitrotoluene and RDX was facilitated by biochar in the presence of dithiothreitol [23], demonstrating that biochar is chemically reactive toward 2,4-dinitrotoluene and RDX through the conduction mechanism.

Unlike the conduction mechanism, the second mechanism, ESC, does not require an external electron donor in place; instead, the electrons are stored in the redox functional groups of biochar. Through the ESC, biochar can be a sole electron donor when the ESC is saturated, or conversely, be a sole electron acceptor when ESC is vacant, for supporting chemical and microbial redox processes. ESC mechanism is important because it would determine the reactivity of biochar towards contaminants in the absence of an external electron donor. Studies in recent years have shown that ESC is a common property of biochar prepared from pyrolysis of plant-based biomass.

[5, 11, 12, 43, 59, 100, 129] In addition, the ESC of biochar is reported to be distributed over a broad range of reduction potential and highly reversible over multiple redox cycles. Previous studies have suggested that the ESC of biochar is available for the abiotic reduction of metals [81, 96] and oxyanions [94, 95]. However, no studies have ever determined the availability of ESC of biochar for the abiotic transformation of organic compounds including MCs.

We hypothesized that biochar can be a rechargeable electron donor to support abiotic transformations of MCs through its ESC. Furthermore, it is necessary to determine the availability of ESC to insensitive MCs and the rate at which the ESC promotes MC reductions, in order to provide biochar-based remediation alternatives for stormwater systems. The goal of this Chapter is twofold– to test the hypothesis that biochar can abiotically reduce MCs through its ESC, and to demonstrate the utility of biochar for removing insensitive MCs from stormwater systems.

To this end, we conducted batch experiments to assess the efficacy of two wood-derived biochars to remove NTO in buffered solutions at pH 6−10 and in artificial stormwater runoff (ASR) at pH 6. Parallel experiments were performed using dithionite-reduced (ESC-saturated) biochar as an electron donor for the abiotic reduction of NTO and air-oxidized (ESC-vacant) biochar for non-reactive sorption control. Mass balance, electron balance, and ESC reversibility were assessed to determine the amount of NTO reduced by biochar, the fraction of ESC of biochar reactive toward NTO and its reversibility over multiple redox cycles, respectively. To further confirm our hypothesis, we measured the capacity of biochar to sorb and/or reduce other MCs, including NQ, DNAN, and RDX. To the best of our knowledge, this is the first to demonstrate that biochar can be a rechargeable electron donor for the

abiotic degradation of organic pollutants, in which NTO and other MCs served as model compounds. Moreover, the comparison of the reactivity of biochar toward different MCs would collectively offer insights into the development of biochar-enhanced treatment technology and remediation strategies for DoD sites.

1.14 Materials and Methods

1.14.1 Chemicals

NTO and RDX (with 3.8% octahydro-1,3,5,7-tetranitro-1,3,5,7-tetrazocine (HMX) as a manufacturing impurity) were acquired from U.S. Army Armament Research Development and Engineering Center (Picatinny, NJ). NQ (25% water content) and DNAN (98%) were purchased from Sigma-Aldrich (St. Louis, MO). 3-Amino-1,2,4-triazol-5-one (ATO, >99%) was purchased from Princeton BioMolecular Research (Princeton, NJ). 2-Amino-4-nitroanisole (2-ANAN) and 4-amino-2-nitroanisole (4-ANAN) were purchased from Apollo Scientific (Cheshire, UK), and 2,4-diaminoanisole (DAAN, 99.6%) was purchased from Honeywell Fluka (Charlotte, NC). The three nitroso-containing intermediates of RDX, including hexahydro-1-nitroso-3,5-dinitro-1,3,5-triazine (MNX), hexahydro-1,3-dinitroso-5-nitro-1,3,5-triazine (DNX), and hexahydro-1,3,5-trinitroso-1,3,5-triazine (TNX), were purchased from SRI International (Menlo Park). Neat standards of NTO, NQ, DNAN, RDX, and HMX were acquired from AccuStandard (New Haven, CT). Other chemicals used for making buffers or ASR, adjusting solution pH, serving as HPLC eluents, and chemical redox titration of biochar are provided in Table 5.1 below. All chemicals were used as received.

Table 5.1   List of chemicals used [a]

	Name	Formula	Purity	Manufacturer
Buffer	2-(N-morpholino)ethanesulfonic acid (MES)	$C_6H_{13}NO_4S$	>98%	Fisher Scientific (Pittsburgh, PA)
	2-amino-2-(hydroxymethyl)-1,3-propanediol (Tris, base)	$C_4H_{11}NO_3$	99.8%	Sigma-Aldrich (St. Louis, MO)
	3-(cyclohexylamino)-2-hydroxy-1-propanesulfonic acid (CAPSO)	$C_9H_{19}NO_4S$	>99%	Acros Organics (Morris Plains, NJ)
Artificial stormwater runoff (ASR)	sodium chloride	NaCl	99%	Fisher Scientific
	potassium chloride	KCl	99+%	Acros Organics
	magnesium chloride hexahydrate	$MgCl_2 \cdot 6H_2O$	99%	Fisher Scientific
	calcium chloride dihydrate	$CaCl_2 \cdot 2H_2O$	98+%	Fisher Scientific
	sodium sulfate anhydrous	Na_2SO_4	99.8%	Fisher Scientific
	ammonium sulfate	$(NH_4)_2SO_4$	99%	Fisher Scientific
	calcium nitrate tetrahydrate	$Ca(NO_3)_2 \cdot 4H_2O$	>99%	Fisher Scientific
For pH adjustment	hydrochloric acid solution	HCl	37.2% (ACS plus)	Fisher Scientific
	sodium hydroxide solution	NaOH	1N standard solution (trace metal grade)	Acros Organics
Eluents for HPLC	acetonitrile	C_2H_3N	>99.9%	Fisher Scientific
	trifluoroacetic acid	$C_2HF_3O_2$	>99.9%	MilliporeSigma (Burlington, MA)
	methanol	CH_3OH	>99.9%	Fisher Scientific
	potassium phosphate dibasic	K_2HPO_4	99.4%	Fisher Scientific
	potassium phosphate monobasic	KH_2PO_4	99.5%	J.T. Baker (Phillipsburg, NJ)
Redox titrants	sodium dithionite	$Na_2S_2O_4$	>85%	Alfa Aesar (Haverhill, MA)
	potassium ferricyanide	$K_3Fe(CN)_6$	>99%	Acros Organics

[a] Information on MCs are provided in the main text.

Table 5.2   Summary of batch reaction conditions for MC reduction

	MC	C_0	Biochar	Dose	pH	Background solution	Replicate	Figure
Buffered system	NTO	110 µM	SRB_{OX}, SRB_{RED}	0.80 g/L	6	50mM MES	3	5.1(a)
	NTO	110 µM	SRB_{OX}, SRB_{RED}	0.80 g/L	8	50mM Tris	3	5.1(b)
	NTO	110 µM	SRB_{OX}, SRB_{RED}	0.80 g/L	10	50mM CAPSO	3	5.1(c)
	NTO	110 µM	SRB_{OX}, SRB_{RED}	0.40 g/L	10	50mM CAPSO	3	5.2(b)
	ATO	120 µM	SRB_{RED}	0.80 g/L	6, 8, and 10 [a]		2	A.5
	NQ	100 µM	SRB_{RED}	1.33 g/L	6 and 8 [a]		2	A.8(b)
	NQ	100 µM	SRB_{OX}, SRB_{RED}	1.33 g/L	8	50mM Tris	2	A.10
ASR	NTO	110 µM	SRB_{OX}, SRB_{RED}	0.80 g/L	6	ASR	3	5.9(a), (b)
	NTO	110 µM	$Rogue_{OX}$, $Rogue_{RED}$	0.80 g/L	6	ASR	3	5.9(a), (b)
	DNAN	400 µM	$Rogue_{OX}$, $Rogue_{RED}$	0.44 g/L	6	ASR	2	5.9(c), (d)
	RDX	200 µM	$Rogue_{OX}$, $Rogue_{RED}$	0.44 g/L	6	ASR	2	5.9(e), (f)
	HMX	6 µM						A.7(a), (b)
	2A4NAN	350 µM	$Rogue_{OX}$, $Rogue_{RED}$	0.44 g/L	6	ASR	2	5.10(a)
	NO_2^-	200 µM	$Rogue_{OX}$, $Rogue_{RED}$	0.44 g/L	6	ASR	2	5.10(b)

All experiments were run in an anaerobic glove box.

[a] 50 mM MES, Tris, and CAPSO buffers were used, respectively, to control the pH at 6, 8, and 10.

Table 5.3   Summary of batch reaction conditions for MC sorption

MC	C_0	Biochar	Dose	pH	Background solution	Replicate	Figure
NTO	5-125 µM	Rogue$_{OX}$	0.20 g/L	6	ASR	2	5.6(a), 5.7(a)
NQ	20-250 µM	Rogue$_{OX}$	0.44 g/L	6	ASR	2	5.6(b), 5.7(b)
DNAN	30-300 µM	Rogue$_{OX}$	0.33 g/L	6	ASR	2	5.6(c), 5.7(c)
RDX	10-125 µM	Rogue$_{OX}$	0.88 g/L	6	ASR	2	5.6(d), 5.7(d)
HMX	0.5-6 µM						5.8(a), (b)
NQ	200 µM	SRB$_{OX}$	0.80 g/L	8	50mM Tris	2	A.8(a)
NQ	25-200 µM	SRB$_{OX}$	0.80 g/L	8	50mM Tris	2	A.9(a), (b)

All experiments were run outside of an anaerobic glove box.

1.14.2 Biochars

Two wood-based commercial biochars, Soil Reef biochar (SRB) and Rogue biochar (Rogue), were used. Physical-chemical properties of SRB and Rogue were determined, as described in Section A.4, and summarized in Table A.5. Note that SRB and Rogue are both derived from pine wood but prepared under distinct pyrolysis conditions, 550 °C through pyrolysis and 900 °C through fast pyrolysis, respectively. While the production of SRB had discontinued years ago, SRB was chosen because it has been field-tested for stormwater treatment and its ESC is well characterized. Among the properties, BET surface area and ESC are arguably the most important properties that may influence the sorption and transformation capacities of biochar, respectively, for MCs. Based on the BET surface area and ESC of Rogue biochar (407.22±9.18 m^2/g and 7.07±0.15 mmol/g) being more than two times those of SRB (158.39±3.34 m^2/g and 3.54±0.13 mmol/g), Rogue biochar was also included.

To facilitate the reaction kinetics between a biochar and MC, SRB and Rogue biochar in the size range of 250–500 µm was individually ground at 4000 rpm for 3 min using a Beadbug 3 bead homogenizer (Benchmark Scientific Inc., Sayreville, NJ) to obtain a particle size <53 µm. Ground biochars were then oxidized with dissolved O_2 (DO) in continuously aerated deionized water to drain stored electrons, i.e., to bring the electron donating capacity of biochar to zero with respect to DO (E_h= +0.80 V vs SHE, at pH 7 and P_{O_2}= 0.21 atm). Based on our preliminary ESC analyses, SRB and Rogue were oxidized for 72 and 2 weeks, respectively, to ensure complete oxidation of reduced functional groups in those samples. The prolonged oxidation of biochar was necessary to exclude the possibility of MC reduction. The DO-oxidized

biochars were collected on a glass microfiber filter, dried at 64 °C, and stored in a desiccator before use.

Each biochar was split into two types: DO-oxidized biochar (labeled SRB_{OX} and $Rogue_{OX}$ hereafter) and dithionite-reduced biochar (labeled SRB_{RED} and $Rogue_{RED}$). SRB_{OX} or $Rogue_{OX}$, which was depleted of stored electrons, served as sorption control, whereas SRB_{RED} or $Rogue_{RED}$ served to test whether the electrons stored in biochar is accessible and reactive toward MCs. To prepare dithionite-reduced biochars, the DO-oxidized biochars were first deoxygenated and transferred into an anaerobic glove box (Coy Laboratory Products Inc., Grass Lake, MI). A subsample of SRB_{OX} or $Rogue_{OX}$ was reduced with the solution containing 25 mM freshly prepared sodium dithionite and 100 mM citrate at pH 6.4 for 3 days (measured $E_h = -0.43$ V vs SHE). Dithionite was added in excess and was replenished as needed to ensure the reduction of biochar. SRB_{RED} and $Rogue_{RED}$ were collected on a glass microfiber filter, rinsed thoroughly with DO-free deionized water to remove residual chemicals, vacuum-dried, and stored in a desiccator in the glove box. All reported data are based on dry weights.

1.14.3 Summary of batch experimental conditions

Batch reactors were prepared using dithionite-reduced biochar (SRB_{RED} or $Rogue_{RED}$) to test its reactivity as an electron donor for the abiotic reduction of each MC. In parallel, batch reactors containing DO-oxidized biochar (SRB_{OX} or $Rogue_{OX}$) were prepared under the same conditions as a non-reactive, sorption control. All the experiments were conducted inside an anaerobic glove box under $98\pm0.5\%$ N_2, $2.5\pm0.5\%$ H_2, and $P_{O_2} < 5$ ppm. A summary of the batch experimental conditions,

including the initial concentration of MC, biochar dose, and background solution, is included in Table 5.2.

1.14.4 NTO reduction in buffered solutions

A set of batch experiments was performed with SRB for NTO in buffered solutions at pH 6, 8, and 10. To initiate the reaction, a predetermined amount of either SRB_{OX} or SRB_{RED} (0.4 or 0.8 g/L) was added to amber borosilicate reactors containing 125 mL of 110 µM NTO and 50 mM buffer. MES, Tris, and CAPSO buffers were used to maintain the pH constant at 6.0 ± 0.1, 8.0 ± 0.1, and 10.0 ± 0.1, respectively, throughout equilibration. Blanks without biochar were also prepared for comparison. All reactors were shaken on an orbital shaker at 100 rpm. Aliquots of 0.625 mL solution were taken at different elapsed times and immediately passed through 0.22-µm PTFE syringe filters for high-performance liquid chromatography (HPLC) analysis. Experiments were run up to 600 h at which the concentration of ATO stayed constant. Up to 13 samples were taken, which was less than 10% of the initial solution volume; the consumption of NTO (and ATO) due to sampling was accounted for based on mass balance.

After 600 h for equilibration, the SRB (SRB_{OX} or SRB_{RED}) exposed to NTO was retrieved on a glass microfiber filter, vacuum-filtered, thoroughly rinsed with deionized water. Given no sorption of NTO (and ATO) was observed at pH 10, we placed the retrieved SRB in 50 mL of 50 mM CAPSO buffer at pH 10 ± 0.1, in order to extract the sorbed NTO (and ATO) from the SRB. Extracts (0.625 mL) were sampled at predetermined times up to 600 h for HPLC analysis.

1.14.5 Ferricyanide titration for electron balance

An attempt was made to retrieve electrons from NTO-exposed SRB_{RED} and fresh SRB_{RED} using ferricyanide (E_h = +0.43 V vs. SHE at pH 7). Reactors containing NTO-exposed SRB_{OX} and fresh SRB_{OX} were included as controls, respectively. NTO-exposed SRB is the SRB that was exposed to NTO and then to CAPSO buffer for NTO reduction and desorption of NTO (and ATO), respectively. After exposure to CAPSO buffer, NTO-exposed SRB was again collected on a glass microfiber filter, rinsed thoroughly with deoxygenated deionized water to remove residual CAPSO buffer. NTO exposed or fresh SRB was then placed in 0.23 L of 1 mM ferricyanide solution at pH 6, 8, or 10, buffered with 50 mM MES, Tris, or CAPSO, respectively. The electrons transferred from SRB to ferricyanide at each pH were determined by quantifying the consumption of ferricyanide. Ferricyanide concentrations were determined by monitoring absorbances at the wavelength of 420 nm using a Vernier LabQuest 2 UV-vis spectrophotometer (Beaverton, OR). The extinction coefficients of ferricyanide at pH 6, 8, 10 were 1135 ± 38 $M^{-1} \cdot cm^{-1}$, 1152 ± 42 $M^{-1} \cdot cm^{-1}$, 1058 ± 42 $M^{-1} \cdot cm^{-1}$, respectively. The ferricyanide experiments were run for 24–72 h depending on the equilibration time needed. At the end of the experiment, SRB in each reactor was collected through filtration and dried at 65 °C for 24 h in a vacuum oven to confirm the SRB mass.

1.14.6 The reversibility of ESC towards NTO

A set of batch experiments was performed to demonstrate the reversibility of ESC of SRB toward NTO over three redox cycles. To prevent sorption of NTO or ATO to SRB, the experiments were run at pH 10 in 50 mM CAPSO buffer. Four types of reactors containing 125 mL of 100 µM NTO were set up in duplicates: 0.8 g/L of

SRB_{RED} was added to the first two pairs of reactors, 0.8 g/L of SRB_{OX} was added to the third pair of reactors, and no biochar was added to the last pair of reactors. For each cycle, the experiments were run in the same way as described above for NTO reduction but were run only for 24 h. After 24 h, SRB (SRB_{OX} or SRB_{RED}) exposed to NTO was retrieved on a glass microfiber filter, vacuum-filtered, thoroughly rinsed with 50 mL of 50 mM CAPSO buffer three times. For the first pair of reactors containing SRB_{RED}, the retrieved SRB_{RED} was reduced with 50 mL of 1 mM dithionite (100 µmol e$^-$ equivalence) for 24 h and retrieved for the next cycle of NTO reduction. This pair of reactors was labeled as "SRB_{RED}-ESC-recharged". For the other pair of reactors containing SRB_{RED}, the retrieved SRB_{RED} was left as it is and labeled as "SRB_{RED}-ESC-not-recharged". The procedures for the second cycle of NTO reduction are the same as the first cycle, that is, exposing both "SRB_{RED}-ESC-recharged" and "SRB_{RED}-ESC-not-recharged to 125 mL of 100 µM NTO in 50 mM CAPSO buffer for 24 h. After the second cycle, the ESC was charged again for the SRB in "SRB_{RED}-ESC-recharged" reactors for the third cycle. No biochar and SRB_{OX} controls were included in each cycle.

1.14.7 MC reduction in ASR

To mimic the performance of biochar in stormwater, batch experiments were also run in ASR that was developed based on the composition of stormwater samples collected in swales. The ASR consists of 10 mg/L NaCl, 18mg/L KCl, 10 mg/L $MgCl_2 \cdot 6H_2O$, 10 mg/L $CaCl_2 \cdot 2H_2O$, 15 mg/L Na_2SO_4, 6 mg/L $(NH_4)_2SO_4$, 3 mg/L $Ca(NO_3)_2 \cdot 4H_2O$. A set of batch experiments was performed with either $Rogue_{OX}$ or $Rogue_{RED}$ for NTO, DNAN, and RDX in ASR at pH 6. For comparing SRB and Rogue, an additional experiment with SRB (SRB_{OX} or SRB_{RED}) was run for NTO in

ASR at pH 6 under the same conditions. During the experiment, pH was controlled at pH 6.0±0.2 using 0.05 N HCl. Aliquots of 0.625 mL solution were taken for NTO and DNAN experiments, whereas aliquots of 6 mL solution were collected for RDX experiments, in which 5 mL was used to determine NO_2^- concentration, and the leftover was used to determine RDX and its daughter compounds. The total solution volume that was consumed due to sampling was less than 10% in all experiments, which were accounted for in MC mass balance.

After completion of each reduction experiment, both oxidized and reduced biochar samples were subjected to organic solvent extractions. NTO, NQ, and their daughter products sorbed to biochar were extracted using a 3:7 (v/v) mixture of acetonitrile and 0.1% trifluoroacetic acid, whereas DNAN, RDX, and their daughter products were extracted using an 8:2 (v/v) mixture of acetonitrile and 0.1% trifluoroacetic acid. [130] The extractions were repeated twice on the same biochar sample. Recovery of each MC (and, if exist, its daughter products) from two extractions were combined to obtain the total mass recovery.

1.14.8 MC sorption isotherm

A series of batch experiments were performed to obtain the sorption isotherm of each MC to Rogue$_{OX}$ in ASR at pH 6. For obtaining an isotherm, amber borosilicate glass reactors were set up in duplicates, each containing ASR and an MC at seven different initial concentrations. The concentration range of MC and biochar dose (given in Table 5.3) were designed based on preliminary experiments and the solubility of MC. MC sorption experiments were performed using a similar procedure as described above for NTO reduction. Specifically, a predetermined amount of Rogue$_{OX}$ was added to each reactor, which was then placed on an orbital shaker at 100

rpm. Aliquots of 0.8 mL solution were collected at different elapsed times and passed through 0.2-μm PTFE syringe filters prior to analysis by HPLC. The experiments were run up to 400 h until the change of MC concentration was less than 1% per hour compared to its initial concentration. During the experiment, pH was manually adjusted to 6.0±0.2 using 0.05 N HCl. In addition to the experiments with Rogue$_{OX}$, we ran a set of batch experiments to obtain the sorption isotherm of NQ to SRB$_{OX}$ in 50 mM Tris buffer at pH 8±0.1.

Mass of MC sorbed to each gram of biochar (C_s) was plotted against the equilibrium aqueous concentration (C_{aq}), and the data were fitted to a Langmuir isotherm (Equation 5.1) using the least-square method.

$$C_S = \frac{K_L C_{aq} C_{s,max}}{1 + K_L C_{aq}}$$ (5.1)

where C_s (μmol/g) is the sorbed MC mass per gram of biochar, C_{aq} is the aqueous concentration of MC at equilibrium (μM), $C_{s,max}$ (μmol/g) and K_L (μM^{-1}) are fitted parameters representing the maximum adsorption capacity and adsorption affinity of MC for biochar, respectively.

After each set of sorption experiments, biochar samples that sorbed the maximum mass (i.e., at $C_{s,max}$) of MC were subjected to organic solvent extractions. The extractions were done following the same procedure described above for MC reduction experiments.

1.14.9 Analytical methods.

MCs were analyzed using an Agilent 1200 Series HPLC (Agilent, Santa Clara, CA) with an Agilent 1260 diode array detector. The three hydrophilic compounds, including NTO, ATO, and NQ, were separated with a Thermo Scientific (Waltham,

MA) Hypercarb Porous Graphitic Carbon column (4.6 mm×100 mm, 5 μm particle size). A mixture of acetonitrile and 0.1% trifluoroacetic acid was used as eluent in a gradient at a flow rate of 2.0 mL/min. The run time was 10 min and the temperature was set at 34.0 °C. NTO, ATO, and NQ were detected at 7.9 min, 4.3 min, and 5.8 min and quantified based on absorbance at 318 nm, 210 nm, and 260 nm, respectively. Hydrophobic MCs, DNAN, RDX, and HMX, and their daughter compounds were separated with an Agilent Zorbax SB-C18 column (4.6 mm×50 mm, 3.5 μm particle size). A mixture of phosphate buffer and methanol was used as eluent at a flow rate of 1.7 mL/min. The run time was 7 min and the temperature was set at room temperature. DNAN and RDX were detected at 3.4 min and 4.8 min, respectively, and quantified based on absorbance at 214 nm. HMX was detected at 2.4 min at 234 nm. The same method was used to detect and quantify potential daughter compounds of DNAN and RDX. 2-ANAN, 4-ANAN, and DAAN, which could be the reduction products of DNAN [131], were measured at 4.2 min (254 nm), 3.2 min (234 nm), and 2.3 min (210 nm), respectively. MNX, DNX, and TNX, which could be the reduction products of RDX [132, 133], were measured at 2.9 min, 2.4 min, and 1.9 min, respectively, based on absorbance at 234 nm. Nitrite, which could be a reduction product of RDX, was measured using Hach NitriVer® 3 Nitrite Reagent (Loveland, CO).

1.15 Results and Discussion

1.15.1 The effect of pH on NTO removal by SRB

Figure 5.1 shows NTO removed by SRB_{OX} or SRB_{RED} over time at pH 6, 8, and 10 in buffered solutions and the mass balance of NTO at the end of each experiment. Since no transformation product was detected in reactors containing

SRB_{OX}, the removal of NTO by SRB_{OX}, although minimal, is most likely due to sorption. Sorption of NTO to SRB_{OX} decreased with increasing pH and was negligible at pH 10, leading to a gradual increase in equilibrium mass balance at ca. 600 h, from 80%, 93%, to 99% at pH 6, 8, and pH 10, respectively (solid blue bars in Figure 5.1(d)). The effect of pH on the sorption of NTO to SRB_{OX} is mainly due to the electrostatic interaction between NTO and SRB. Given the pK_a of NTO is 3.67 [127], NTO is negatively charged at the pH range tested. While an isoelectric point of 2−3.5 [77] has been reported for wood- and other plant-based biochars, locally positively charged points, e.g., mineral cations, of SRB_{OX} may be responsible for the electrostatic sorption. This is also consistent with the relatively small amount of NTO sorbed to SRB_{OX} (24, 10, 2 µmol/g at pH 6, 8, 10, respectively). When CAPSO buffer was used to extract NTO sorbed to SRB_{OX}, the final mass balance of NTO for SRB_{OX} that was exposed at pH 6 and 8, respectively, was 94% and 101%, verifying that NTO was sorbed to SRB_{OX} mainly through electrostatic force.

In all pH conditions tested (6−10), a significantly higher amount of NTO was removed by SRB_{RED} than SRB_{OX}. In addition, ATO was formed concomitantly with the removal of NTO in the reactors containing SRB_{RED}, showing NTO was chemically reduced to ATO by SRB_{RED}. The difference in NTO removed by SRB_{RED} and SRB_{OX} also demonstrates that the removal of NTO by SRB_{RED} can primarily be attributed to reduction. The mass balance of NTO (NTO+ATO) for SRB_{RED} at the end of the experiment (solid blue and red bars in Figure 5.1(d)) remained constant at 80% at pH 6 and pH 8 but closed at pH 10. This implies that, unlike NTO that showed a gradual decrease in sorption with pH increase, ATO, which was predominant in reactors containing SRB_{RED}, sorbed to SRB_{RED} to a similar extent at pH 6 and 8 but negligibly

106

at pH 10. The sorption of ATO to SRB_{RED} at different pH was also confirmed in Figure A.5. As the pK_a of ATO has not been experimentally determined in literature, we performed an acid-base titration for ATO. In agreement with the results, the pK_a of ATO was determined to be 8.71 (Figure A.6), meaning ATO was mainly in its deprotonated and negatively charged form at pH 10, whereas ATO was in its neutral form at pH 6 and 8.

As a complete mass balance (the dotted line) was developed at pH 10 (Figure 5.1(c)), (1) neither NTO nor ATO was sorbed to SRB_{RED}, and (2) all NTO removed by SRB_{RED} was due to reduction at pH 10. After CAPSO buffer extraction for ATO and NTO, the mass balance of reactors with SRB_{RED} ranged between 91−100%. The small but incomplete mass balance could potentially be due to other interactions between SRB and NTO than the electrostatic force, such as π−π electron donor-acceptor interaction [126], which cannot be overcome by increasing the pH.
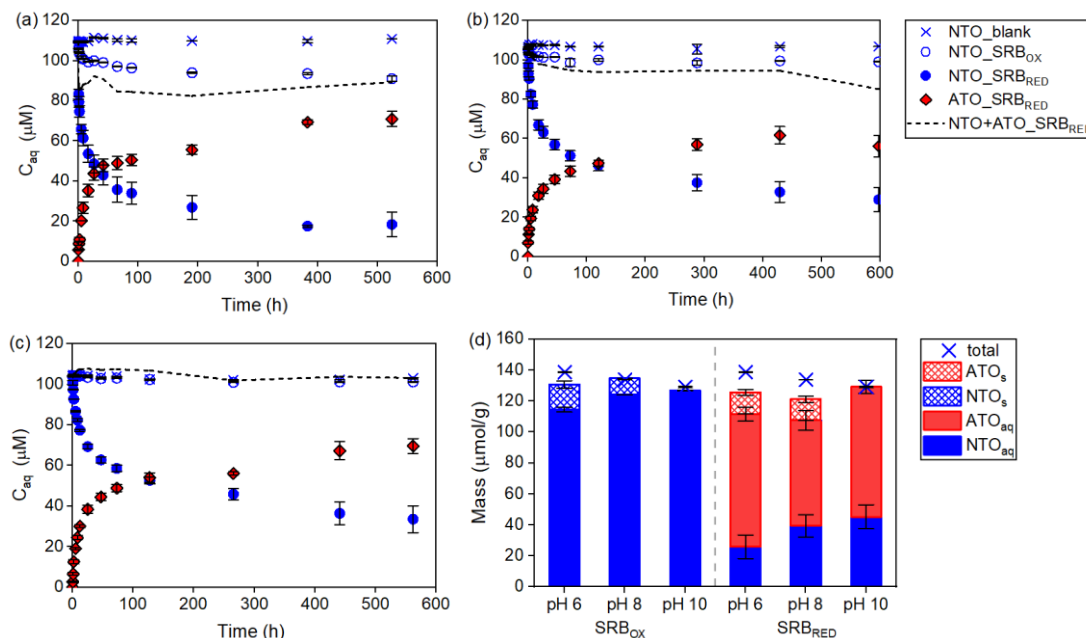
Figure 5.1　Aqueous concentration (C_{aq}) of NTO and/or ATO over time with 0.80 g/L of SRB_{OX} or SRB_{RED}. (a) pH 6 (buffered with 50 mM MES) (b) pH 8 (buffered with 50 mM Tris) (c) pH 10 (buffered with 50 mM CAPSO) (d) NTO mass balance. "total" is the NTO in the blank (no SRB reactor). NTO_{aq} and ATO_{aq} are the mass in the aqueous phase at the end of the experiment (ca. 600 h). NTO_s and ATO_s are the extracted mass from the solid phase.

1.15.2　The fraction of ESC of SRB available for NTO reduction

Figure 5.2(a) shows NTO removal and ATO formation in the aqueous phase by 0.4 g/L and 0.8 g/L of SRB at pH 10. Since no ATO was detected in reactors with SRB_{OX} that is vacant of its ESC, the reactivity of SRB_{RED} to NTO can be attributed to the ESC of SRB. When the mass of SRB_{RED} decreased by half, the formation of ATO decreased proportionally, showing the quantity of electrons available for NTO reduction is proportional to SRB mass. In addition, the ATO formed matched nicely with the NTO removed (Figure 5.2(b)), demonstrating that NTO was completely

108

transformed to ATO by SRB_{RED} through its ESC. These results suggest that the ESC of SRB that is reactive toward NTO is consistent. The amount of ATO that was formed by SRB_{RED} through abiotic reduction was 83.87 µmol/g at pH 10, as determined by the slope of ATO formed in Figure 5.2(b).
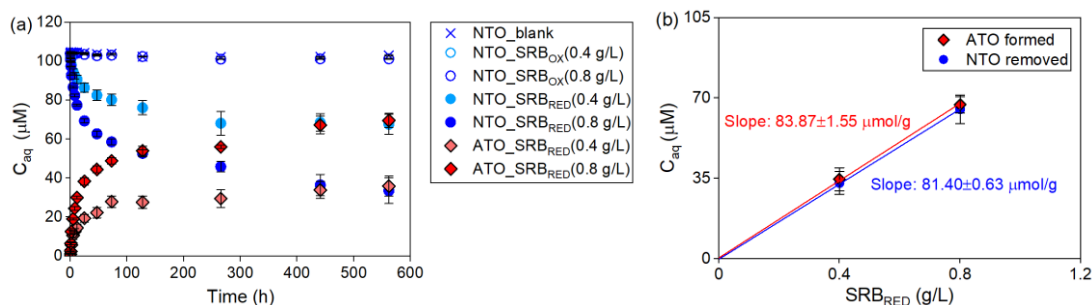
Figure 5.2   (a) Aqueous concentration (C_{aq}) of NTO and ATO over time with 0.80 g/L or 0.40 g/L of SRB over time at pH 10. (b) Total ATO formed and NTO removed by SRB_{RED} at the end of the experiment (ca. 600 h) at pH 10.

Despite the sorption of ATO at pH 6 and 8, the total amount of ATO was determined by combining ATO in the aqueous phase (ATO_{aq}) and the solid phase (ATO_s). The total amount of ATO formed by 0.8 g/L of SRB_{RED} at pH 6 and 8 was 99.65 ± 6.61 and 81.64 ± 8.41 µmol/g, respectively (Table A.6). As the reduction of NTO to ATO requires $6e^-$ transfer per molecule (Equation 5.2), the total electrons transferred from SRB_{RED} to NTO, i.e., the ESC of SRB that is reactive toward NTO, can be estimated by multiplying 6 to the ATO formed ($ATO_{aq}+ATO_s$).

O₂N—[triazolone ring, N⁻, =O, N—NH] $+ 7H^+ + 6e^- \rightarrow$ H₂N—[triazolone ring, NH, =O, N—NH] $(pK_{a\,(NTO)}=3.76<pH<pK_{a\,(ATO)}=8.71)$

O₂N—[triazolone ring, N⁻, =O, N—NH] $+ 6H^+ + 6e^- \rightarrow$ H₂N—[triazolone ring, N⁻, =O, N—NH] $(pH>pK_{a\,(ATO)}=8.71)$ (5.2)
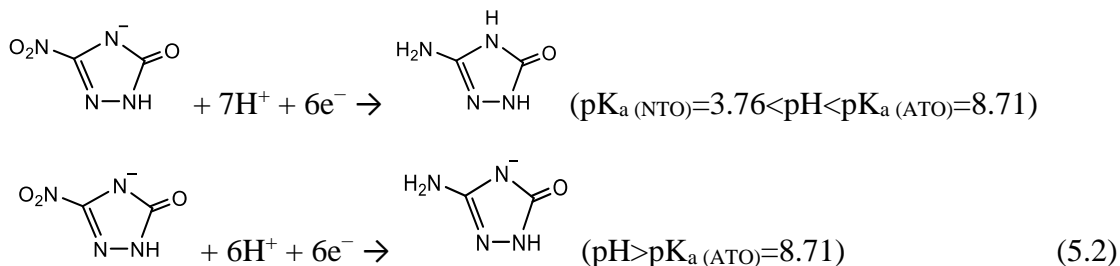
As a result, the quantity of the ESC of SRB that was accessible to and reactive toward NTO was 598, 490, 503 μmol/g at pH 6, 8, and 10, respectively (patterned red bars in Figure 5.3). The ESC of biochar has been attributed to quinoic/hydroquinoic functional groups [5]. The redox reaction of quinone/hydroquinone redox couples involves $2e^-$ and $2H^+$ at the pH below the first pK_a of the hydroquinone, which is usually above 8 [35, 96]. Although the nature of ESC of biochar has not been fully understood, the higher availability of ESC at pH 6 appears to be consistent with the quinone/hydroquinone theory. It is possible that, as the pH increased from 6 to 8, the thermodynamic driving force of NTO reduction by the reduced functional groups of SRB$_{RED}$, e.g., hydroquinoic functional groups, decreased, due to the fact that H^+/e^- of NTO reduction half-reaction was slightly higher than 1.

While the reduction potential of ESC of biochar has not been delineated, our previous findings support that the ESC is distributed over a broad range of reduction potential [59]. As each gram of SRB$_{OX}$ (DO-oxidized SRB) can store up to 4 mmol e^- with dithionite ($E_h= –0.43$ V vs. SHE at pH 6.4) [59], only a fraction of the electrons stored in SRB$_{RED}$ by dithionite (500–600 μmol/g) was available for reducing NTO.

The full electron balance for the electrons stored in SRB$_{RED}$ was not attainable due to the difficulty in quantifying DO ($E_h= +0.80$ V vs. SHE at pH 7). However, an attempt was made to retrieve part of the remaining electrons from NTO-exposed SRB$_{RED}$ using ferricyanide ($E_h= +0.43$ V vs. SHE at pH 7) [59, 71]. Theoretically, the

remaining electrons retrievable by ferricyanide should be the difference between the electrons that can be retrieved from the fresh intact SRB_{RED} (i.e., SRB that is never exposed to NTO) by ferricyanide and the portion of electrons that had been consumed during NTO reduction Equation 5.3.

e^- retrieved from NTO-exposed SRB_{RED}

$$= e^- \text{ retrieved from fresh } SRB_{RED} - e^- \text{ consumed by NTO reduction} \qquad (5.3)$$

Figure 5.3 confirms that the sum of the electrons that was utilized by NTO (patterned red bars) and the electrons retrieved from NTO-exposed SRB_{RED} by ferricyanide (patterned green bars) was the same as the electrons retrieved directly from fresh SRB_{RED} by ferricyanide (stars). This shows that the ESC of SRB that is reactive towards NTO was 26–38% of that towards ferricyanide, suggesting the reactivity of NTO is much lower than that of ferricyanide. It should be noted that the electrons retrieved from fresh SRB_{RED} by ferricyanide seem to be dependent on pH. It notably increased from 1591 µmol/g to 1899 µmol/g when pH increased from 6 to 8 but remained relatively stable (1944 µmol/g) when the pH further increased to 10. The trend of ESC availability to ferricyanide with respect to pH is the opposite of that to NTO, which may be due to the fact that the reduction of ferricyanide does not involve proton transfer. This trend may become less evident when the hydroquinoic functional groups across the pK_as (>8), which appear to be suggested by the data.
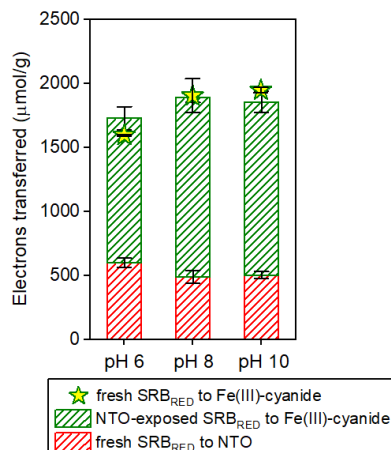
Figure 5.3   Electron balance for SRB$_{RED}$. Electron transferred from fresh SRB$_{RED}$ to NTO was calculated by multiplying 6 to the total mass of ATO formed.

1.15.3 The reversibility of ESC of SRB for NTO reduction.

The high reversibility of ESC of biochar has been demonstrated based on repeated redox titration over multiple cycles [59, 129], which implies that biochar may be a rechargeable electron storage medium for contaminant transformation. Here, as shown in Figure 5.4, the reversibility of ESC of SRB for NTO reduction was assessed at pH 10 over three redox cycles. The pH 10 condition was chosen to avoid the sorption of NTO and ATO to SRB. Consistent with the previous results, NTO removed by SRB$_{OX}$ was negligible. In contrast, NTO was transformed quantitatively to ATO by SRB$_{RED}$, as demonstrated by good mass balances. For the first cycle, the NTO removed in the aqueous phase by SRB$_{RED}$ was around 32 µM after 24 h, which was congruent with the data in Figure 5.1(c). For the second and third cycles, the spent SRB$_{RED}$ ("ESC-not-recharged") was not able to further reduce NTO. However, when the ESC is recharged ("ESC-recharged") by dithionite reduction, a similar amount of NTO was transformed to ATO for all three cycles (Figure 5.5). The ESC that is

112

available for NTO reduction for the second and third cycles was >85% of that for the first cycle, demonstrating high reversibility of ESC of SRB for NTO transformation. This suggests that biochar may be used as a rechargeable reactive medium for contaminant transformation in remediation applications.

To date, most of the environmental research on NTO has focused on sorption [134, 135] and anaerobic biodegradation of NTO to ATO [136, 137] in environmentally relevant matrices such as different types of soils [138]. As ATO can be easily mineralized to products like N_2, CO_2, NH_4^+ [139], the reduction of NTO to ATO is a critical step to achieve complete treatment of NTO. Recent studies have reported that NTO can be abiotically reduced to ATO in Fe^{2+}/hematite system [128] and by humic acids. Adding to these findings, our results suggest that black carbon, which is ubiquitous in subsurface environments, may also support the abiotic reduction of NTO through its ESC, demonstrating that abiotic reduction could potentially be an effective site remediation strategy for NTO.
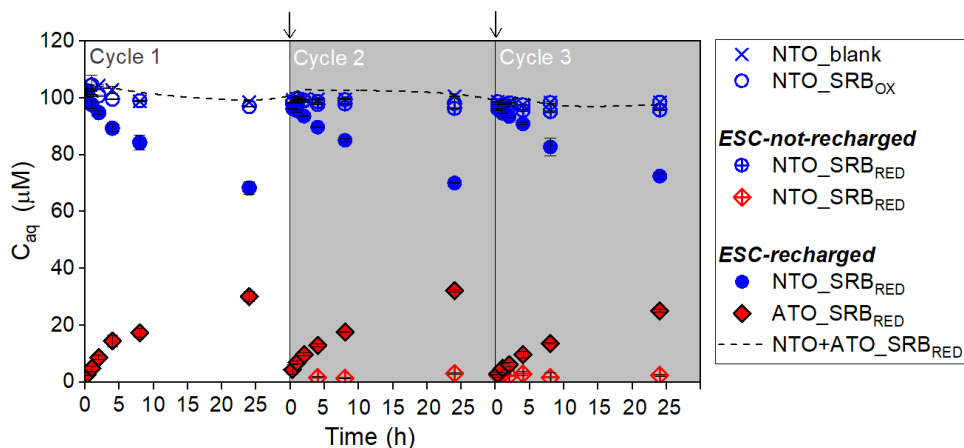
Figure 5.4   The reversibility of ESC of SRB for NTO reduction. Aqueous concentration (C_{aq}) of NTO and ATO over time with 0.80 g/L of SRB_{OX} or SRB_{RED} at pH 10. After each cycle ($\downarrow$), NTO solution was replaced and the ESC of SRB_{RED} was recharged with dithionite. The error bars for the data of SRB_{RED} in the first cycle represent one standard deviation from four replicates.
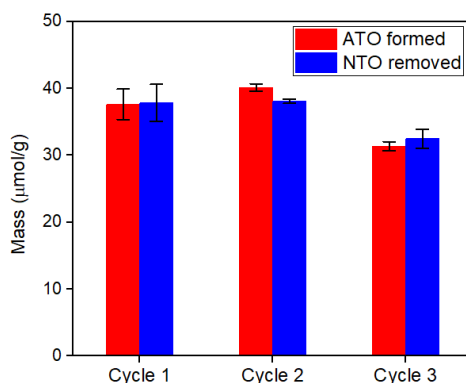
Figure 5.5   The total ATO formed and NTO removed with 0.8 g/L of SRB_{RED} (ESC-recharged) at pH 10 in the three consecutive redox cycles.

1.15.4 The application of biochar for removing MCs

A goal of this work is to evaluate the potential utility of biochar for removing MCs, including NTO, NQ, DNAN, and RDX, from stormwater systems. There are

114

two possible mechanisms, i.e., sorption and abiotic reduction, through which MCs can be removed by biochar. Unlike NTO that is negatively charged under circumneutral pH conditions, NQ, DNAN, and RDX stay neutral and are less water-soluble, which implies that sorption may play a greater role in removing these other MCs.

Prior to determining the availability of ESC towards other MCs, it is necessary to systematically investigate the sorption of MCs to biochar. We chose a commercially available wood-derived biochar–Rogue biochar–to assess its sorption capacity for MCs in ASR at pH 6. Sorption experiments were performed using the air-oxidized biochar (Rogue$_{OX}$), in order to prevent abiotic reduction. As shown in Figure 5.6, each MC was rapidly removed from the aqueous phase as soon as Rogue biochar was added, indicating fast sorption of the MCs onto the biochar surface. However, the sorption subsequently slowed down and continued up to 150-350 h until an apparent equilibrium (<1% removal per hour) was reached. Assuming the sorption of each MC to the biochar surface is instantaneous, the overall kinetics of MC sorption is appeared to be rate-limited by the physical diffusion of MCs through internal pores within Rogue biochar grains. [71]
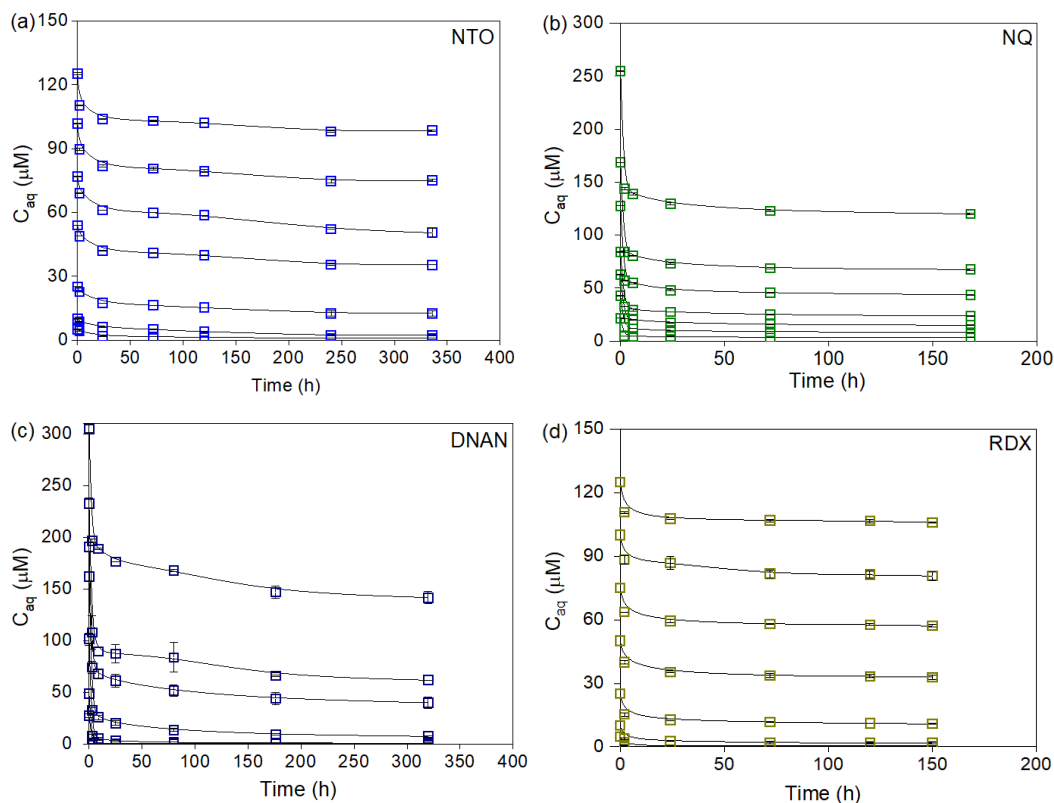
Figure 5.6   Sorption of MCs to Rogue$_{OX}$ over time. Experiments were performed in ASR at pH 6 with different initial MC concentrations. (a) NTO to 0.20 g/L Rogue$_{OX}$ (b) NQ to 0.44 g/L Rogue$_{OX}$ (c) DNAN to 0.33 g/L Rogue$_{OX}$ (d) RDX to 0.88 g/L Rogue$_{OX}$

The sorption capacities of Rogue biochar toward four different MCs were compared through Langmuir isotherm fitting in Figure 5.7, which was further summarized in Table 5.5. The maximum sorption capacity ($C_{s, max}$) of Rogue biochar for NTO, NQ, DNAN, RDX were 153.68, 387.94, 475.94, and 213.01 µmol/g in ASR at pH 6, corresponding to 2.0%, 4.0%, 9.4%, and 4.7% of Rogue biochar mass, respectively. Through organic solvent extraction, 83-88% of sorbed MCs (Table 5.4) were recovered, confirming MCs were sorbed to, not transformed by, Rogue$_{OX}$.

116

Both $C_{s, max}$ and K_L values, reflecting the maximum sorption capacity and affinity, respectively, were highest for DNAN. The strong sorption of DNAN to biochar can be anticipated from the relatively K_{OW} and K_{OC} values (Table 5.5). The favorable sorption of DNAN can also be explained by an enhanced π–π interaction due to two electron-withdrawing nitro functional groups of DNAN. For RDX, despite its low solubility, the non-aromatic plane structure may have resulted in the considerably lower $C_{s, max}$ as compared to DNAN. It should be noted that as 3.8% of HMX was contained in RDX solution, in addition to 4.7% of RDX, Rogue biochar sorbed 30.77 µmol/g of HMX (Figure 5.8), corresponding to 0.9% of Rogue biochar mass. This indicates that Rogue biochar can sorb HMX stronger than RDX when the two compounds co-exist. Although NQ has relatively high water-solubility and the lowest molecular weight, the $C_{s, max}$ for NQ was twice that for NTO in terms of mass, showing that the charge of molecules plays an important role in sorption. Overall, Rogue biochar showed significant sorption capacities for MCs, especially for neutral and aromatic MCs such as DNAN. When the $C_{s, max}$ for NQ was compared for SRB and Rogue (Section A.7), the former was only 98.42 µmol/g (1% of SRB mass), around one-fourth of the latter. This shows that Rogue biochar exhibits a greater sorption capacity for MCs than SRB, possibly due to more than two times higher BET surface of Rogue biochar (Table A.5).
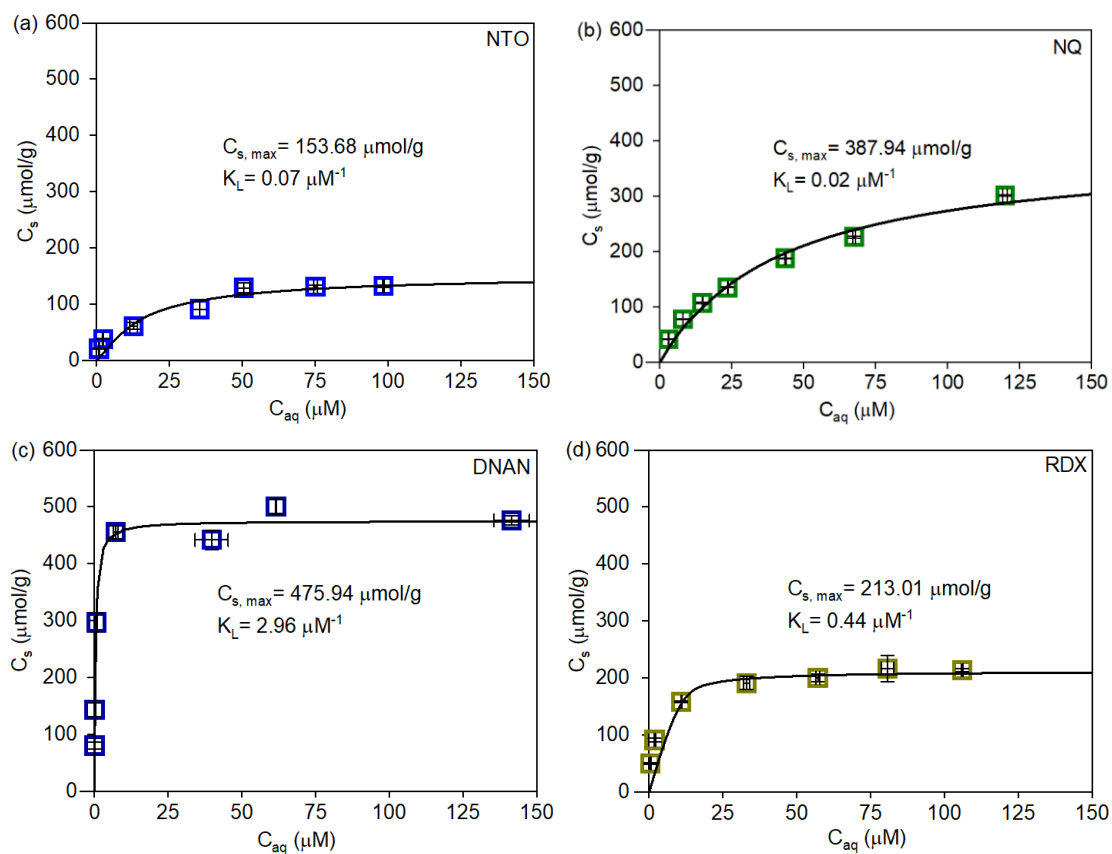
Figure 5.7   MC sorption to Rogue$_{OX}$ in ASR at pH 6 and the fitted Langmuir
isotherms. (a) NTO (b) NQ (c) DNAN (d) RDX

Table 5.4   Extraction efficiency of MCs from Rogue biochar

	Removal (µmol/g)		Recovery(µmol/g)		Extraction efficiency (%)
	AVE	STD	AVE	STD	
NTO	133	4	110	2	83±1%
NQ	374	0.5	329	30	88±8%
DNAN	477	8	421	17	88±4%
RDX	214	3	180	12	84±6%
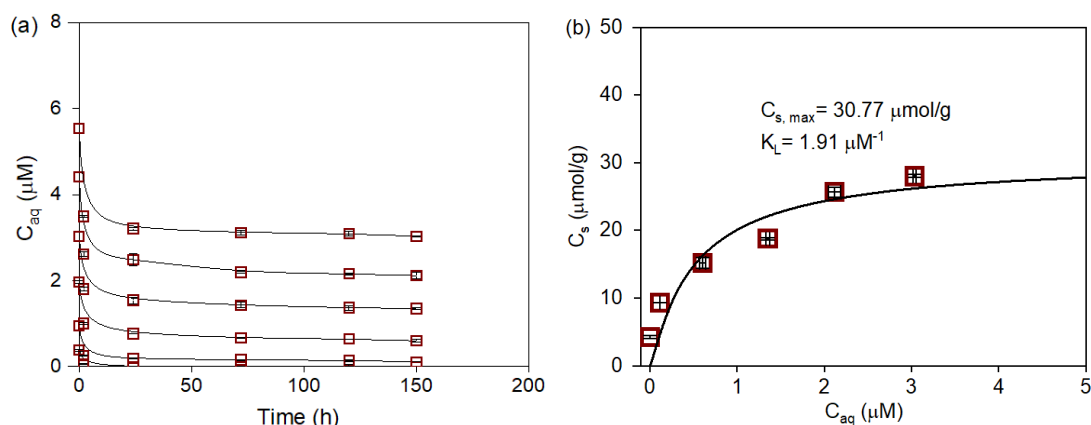
Figure 5.8   Sorption of HMX to Rogue$_{OX}$ in the presence of RDX in ASR at pH 6 (a) Sorption of HMX to 0.88 g/L Rogue$_{OX}$ over time. (b) Sorption of HMX to Rogue$_{OX}$ and its fitted isotherm.

The reactivity of biochar towards other MCs was tested by comparing the removal of each MC by oxidized and reduced biochars. As shown in Figure A.10, NQ was removed from the aqueous phase at similar rates and to the same extent by SRB$_{OX}$ and SRB$_{RED}$, suggesting NQ was sorbed to both oxidized and reduced SRB but did not chemically react with SRB$_{RED}$. This also suggests that, in terms of sorption, the surface characteristics of SRB were not altered by dithionite reduction. While NQ has been reported to undergo photolysis under light and hydrolysis at high pH conditions [140] and be degraded by bimetallic particles [141], it appears that NQ can hardly be degraded by naturally occurring reductants such as carbonaceous materials.

While inert to NQ, as shown in Figure 5.9, reduced biochar was able to abiotically reduce not only NTO but also DNAN and RDX through its ESC. The reduction of NTO by SRB$_{RED}$ in ASR at pH 6 (Figure 5.9(a)) was in good agreement with that in MES buffer also at pH 6 (Figure 5.1(a)), showing that the background solution did not influence the reactivity of biochar. The same NTO reduction

119

experiment in ASR with Rogue$_{OX}$ and Rogue$_{RED}$ demonstrated that Rogue biochar can also abiotically reduce NTO to ATO through its ESC, suggesting that the reactivity of biochar towards NTO is not specific to SRB. Interestingly, SRB$_{RED}$ and Rogue$_{RED}$ biochar removed NTO to a similar extent, produced a total of 91.55 and 94.26 µmol/g ATO (Table 5.6), respectively. This means that the ESC of Rogue biochar reactive toward NTO was around 565.56 µmol/g, which was almost the same as that of SRB (549.30 µmol/g), although the ESC of Rogue biochar measured with Ti(III) citrate and DO was significantly higher than that of SRB (Table A.5). The difference in the fraction of ESC reactive to NTO may be due to the variant distribution of redox functional groups in biochar with respect to reduction potential, requiring further investigation on the nature and its reduction potential distribution of ESC.

The maximum sorption capacity of Rogue biochar, determined through Langmuir isotherm fitting, was 475.94 and 213.01 µmol/g for DNAN and RDX, respectively (Table 5.5). Consistent with this, Rogue$_{OX}$ was able to remove 517.68±4.60 µmol/g of DNAN and 231.50±25.33 µµol/g of RDX at the end of the experiment (Table 5.6). In comparison, when exposed to Rogue$_{RED}$, an additional 117 µmol/g of DNAN was removed beyond sorption, whereas an additional 101 µmol/g of RDX was removed, suggesting the ESC of Rogue may be responsible for the additional removal.

Abiotic reduction of DNAN by Rogue$_{RED}$ was confirmed by the formation of 2ANAN and 4ANAN, which led to a total of 66 µmol/g of 2ANAN and a trace amount of 4ANAN (<2 µmol/g) from aqueous and solid phases. We did not observe any DAAN in the aqueous phase over time as well as in the solid phase after extraction. In addition, Figure 5.10(a) confirmed that Rogue$_{RED}$ was not able to reduce

2ANAN to DAAN, suggesting that 2ANAN—the daughter product of DNAN—is not as reactive as DNAN. The fraction ESC reactive toward DNAN was estimated to be 409 µmol/g, based on the total product formation (assuming 6 electron transfer per molecule of 2ANAN or 4ANAN), which is around 30% lower than that for NTO.

In RDX experiments, trace quantities of NO_2^- (around 5 µM) and MNX (<1 µM) were formed in the presence of $Rogue_{RED}$, but not with $Rogue_{OX}$. We also attempted to measure DNX and TNX but did not observe any. MNX and NO_2^-, with many others (e.g., DNX, TNX, methylenedinitramine, NH_4^+, N_2O, and CH_2O), have been detected as degradation products of RDX [133, 142]. While small quantities, the detection of both NO_2^- and MNX supports that RDX was degraded by $Rogue_{RED}$. The degradation of RDX was further supported by the accumulation of NO_2^- with multiple additions of RDX in reactors containing excess amount of $Rogue_{RED}$, as detailed in Section A.8 (Figure A.11). The accumulation of NO_2^-, on the other hand, supports that Rogue biochar cannot chemically reduce NO_2^- through its ESC, as confirmed in Figure 5.10(b). When organic solvent extraction was performed for both $Rogue_{OX}$ and $Rogue_{RED}$ (Figure 5.9(f)), in contrast to 92% of the mass balance obtained for $Rogue_{OX}$, the mass balance of RDX for $Rogue_{RED}$ was only 60%, showing the remaining 32% of RDX may have been transformed by $Rogue_{RED}$. While an additional 3 µmol/g of MNX was retrieved from the solid phase of $Rogue_{RED}$, the incomplete mass balance suggests that RDX may have undergone ring cleavage and further degraded by $Rogue_{RED}$. Overall, the results show that (1) DNAN and RDX can be reduced by biochar through its ESC; (2) DNAN and RDX can be removed by biochar through concurrent sorption and reduction.
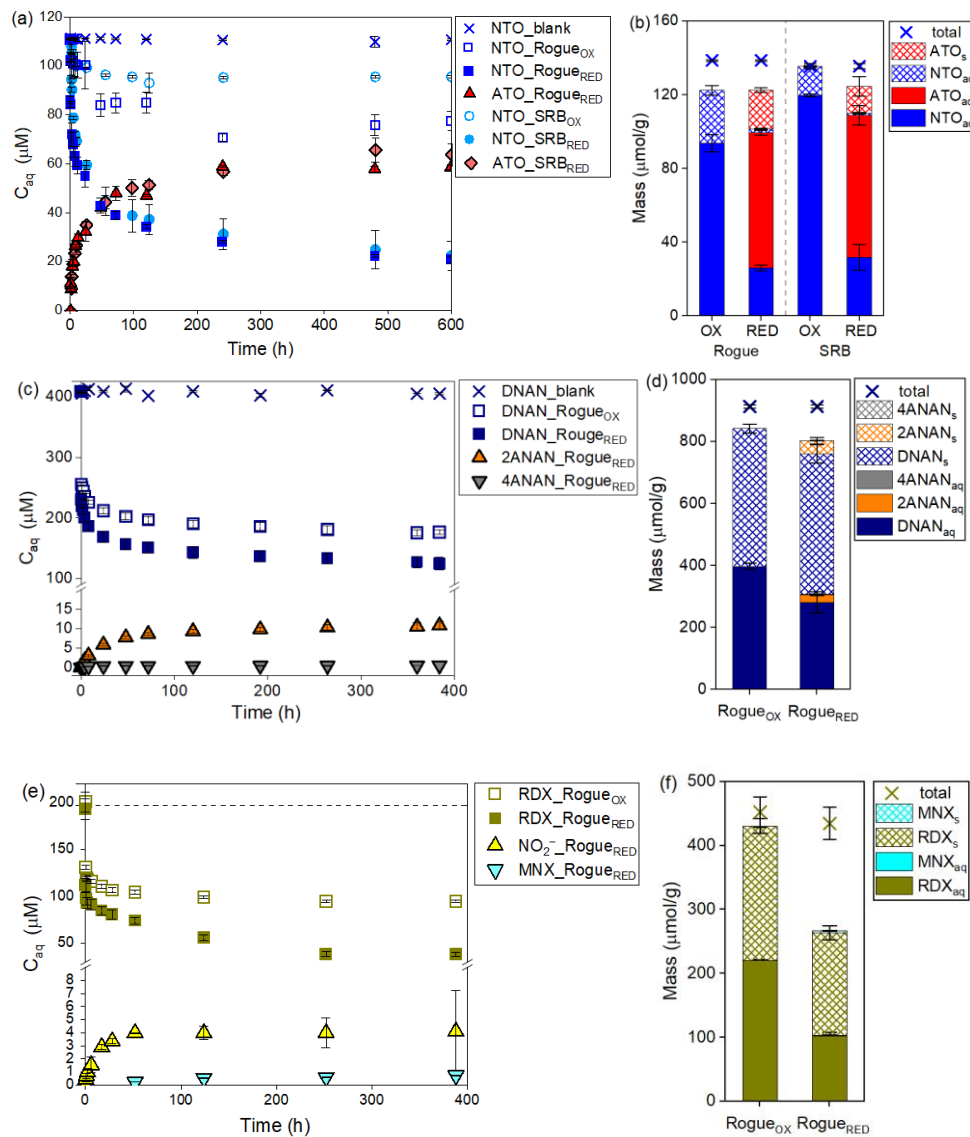
Figure 5.9   MC reduction by biochar in ASR at pH 6. (a) Aqueous concentration (C_{aq}) of NTO and ATO over time with 0.8 g/L of SRB or Rogue. (b) NTO mass balance. (c) C_{aq} of DNAN and 2ANAN/4ANAN over time with 0.44 g/L of Rogue. (d) DNAN mass balance. (e) C_{aq} of RDX and MNX/NO$_2^-$ over time with 0.44 g/L of Rogue. (f) RDX mass balance. "total" is the DNAN or RDX added to blank. Compound names with the subscripts "aq" and "s" represent the masses in the aqueous phase at the end of experiment (ca. 400 h) and the extracted masses from the solid phase, respectively.
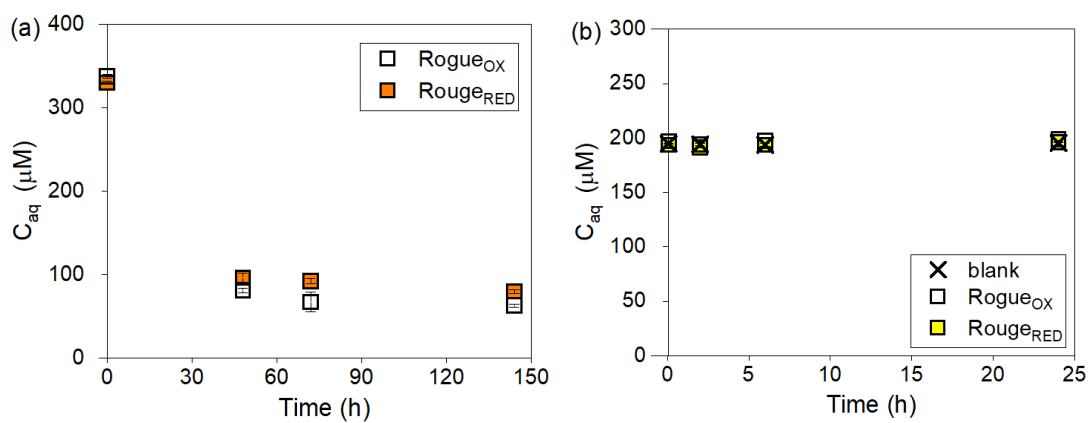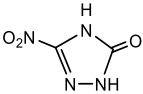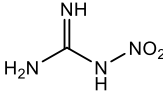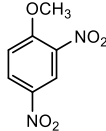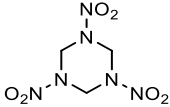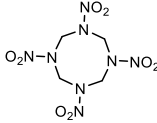
Figure 5.10 Aqueous concentration (C_{aq}) of the daughter product of MC transformation over time with 0.44 g/L of Rogue in ASR at pH 6. (a) 2A4NAN (b) NO_2^-

Table 5.5   Sorption of MCs by Rogue biochar in ASR at pH 6

MC		NTO	NQ	DNAN	RDX	HMX
Structure		O_2N, N, H, O, N–NH	NH, H_2N, N, H, NO_2	OCH_3, NO_2, NO_2	NO_2, O_2N, NO_2	NO_2, O_2N, N–NO_2, O_2N
Formulation		IMX-101 IMX-104	IMX-101	IMX-101 IMX-104	IMX-104	
Physical Properties [a]	M.W. (g/mol)	130.08	104.07	198.13	222.26	296.16
	Solubility (mg/L)	16642 [120]	2600-5000 [141]	276 [120]	60 [120]	5 [120]
	Log K_{OW}	0.37-1.03 [120][b]	0.10 [140]	1.64 [120]	0.81-0.87 [120]	0.19 [120]
	Log K_{OC}	3.03 [120]	−	3.11 [120]	0.88-2.40 [120]	0.54-2.80 [120]
Isotherm Parameters [c]	$C_{s, max}$ (μmol/g)	153.68	387.94	475.94	213.01	30.77
	$C_{s, max}$ (w/w)	2.0%	4.0%	9.4%	4.7%	0.9%
	K_L (μM^{-1})	0.07	0.02	2.96	0.44	1.91
	Regression R^2	0.94	0.96	0.97	0.98	0.88

[a] M.W., solubility, K_{OW}, K_{OC} are molecular weight, solubility at 25 °C, octanol-water partition coefficient, and soil organic carbon adsorption coefficient, respectively.

[b] an estimated value

[c] Parameters of the isotherms are obtained through Langmuir isotherm fitting, as shown in Figure 5.7.

Table 5.6   Summary of MC reduction by biochar at pH 6

MC		NTO	NTO	NTO	DNAN	RDX	HMX
Biochar		SRB	SRB	Rogue	Rogue	Rogue	
Background solution		MES	ASR	ASR	ASR	ASR	
Removal by RED [a]	(μmol/g)	112±8	104±8	112±2	634±20	332±19	11.6±0.7
Removal by OX [b]		24.0±0.07	15.6±2	44.7±6	518±5	232±20	11.0±0.7
Δ Removal [c]		88.2±8	87.9±6	67.6±6	116±16	100±6	0.6±0.02
Product(s) formed		99.6±7[d]	91.6±6[d]	94.3±2[d]	68.1±7[e]	–	–
e− transferred [f]		598±40	549±40	566±14	409±40	–	–

[a] RED: reduced biochar (SRB_{RED} or $Rogue_{RED}$)

[b] OX: oxidized biochar (SRB_{OX} or $Rogue_{OX}$)

[c] Δ Removal: additional MC removal by reduced biochar than oxidized biochar (Row 4 – Row 5).

[d] ATO formed; [e] 2ANAN and 4ANAN formed.

[f] e− transferred=product(s) formed×6 (Row 6 × 6)

1.16 Conclusions

The ESC of biochar is available to abiotically reduce NTO to ATO at pH 6−10, for which a complete mass balance was developed. Through an electron balance, the fraction of ESC available for NTO reduction was around 500-600 µmol/g, which was 26-38% of the ESC available for ferricyanide and 12-15% of that for DO. Moreover, consistent with the reversible nature of ESC, the ESC of biochar was also rechargeable for NTO reduction over three redox cycles, suggesting that biochar can be a rechargeable reactive medium to support the abiotic reduction of contaminants. Finally, the ESC of biochar was also available to abiotically reduce DNAN and RDX in ASR, demonstrating that biochar may be a promising medium for removing MCs in stormwater systems through concurrent sorption and reduction.

This work is the first to demonstrate the availability of ESC of biochar towards organic contaminants and show the abiotic transformation of MCs, including NTO, DNAN, and RDX, by biochar. The work demonstrates the potential of biochar for the attenuation of MCs through sorption and/or abiotic degradation and the development of biochar-enhanced remediation systems for military sites. The results from this Chapter will also offer insights into how black carbon, as an electron storage medium, may influence the fate of MCs in subsurface environments.

Chapter 6

SUMMARY AND OUTLOOK

Centered on the electron storage capacity (ESC) of plant-based black carbon, this work investigated questions related to its origin, redox reversibility, spatial distribution, and environmental applications. First, chemical methods were developed to quantify the ESC of black carbon, evaluate its redox reversibility, and characterize its spatial distribution. Based on a chemical redox titration (CRT) method with Ti(III) citrate and dissolved O_2, the ESC of plant-based black carbon ranged from 0.2−7 mmol/g, which was highly reversible over multiple redox cycles. Using a silver tagging method, a sizable fraction of ESC was confirmed to reside in the interior of black carbon particles, which explains partial microbial accessibility of ESC and the pore diffusion-limited rate observed in the reactions involving the ESC of black carbon. Furthermore, by comparing the ESC of biopolymers and their corresponding chars, the origin of ESC was identified. Pyrolysis was the ESC creating process, suggesting ESC is common for black carbon produced from pyrolysis of lignocellulosic biomass. Finally, fully reduced biochars were applied to abiotically transform munitions compounds, demonstrating the potential utility of biochar for removing organic pollutants through its ESC. This dissertation represents a major step towards understanding the ESC of black carbon. Findings from this dissertation will help explain historical and future data on black carbon-mediated redox processes, lead to new remediation strategies, and have implications for biogeochemical processes

involving black carbon. Future directions that would advance the understanding of black carbon ESC include the following:

1.17 Evaluating the Potential of Biochar to Sequester Redox-Labile Metals and Radionuclides through ESC

The finding (in Chapter 3) that a significant portion of ESC resides in the biochar interior suggests a new mechanism to sequester redox-labile elements. Metal cations, in addition to being removed by biochar through its cation exchange capacity [143, 144], may be removed by and encapsulated in biochar through its ESC. For example, Hg^{II} can potentially be stored as Hg^0 in biochar, which would prevent Hg^{II} from methylation and further bioaccumulation through the food chain. For metal(loid)s ($Cr^{VI}O_4^{2-}$) and radionuclides ($U^{VI}O_2(CO_3)_2^{2-}$) that are commonly present in anionic forms, ESC-enabled reductive immobilization offers a new remediation approach.

1.18 Unraveling the Reduction Potential (E_h) Distribution of ESC

The origin of ESC of black carbon raises a question regarding the nature of the ESC of black carbon and of natural organic carbon (NOM). The ESC of NOM and black carbon have been attributed to redox-labile functionalities such as (hydro)quinones [5, 35, 145], and their ESCs appear to be comparable [5, 34, 73, 146]. However, the ESC of NOM is presumably derived from its precursor biomolecules or produced through a variety of low-temperature abiotic and biological reactions during diagenesis [147, 148], whereas black carbon acquires its ESC entirely through the thermal transformation of its constituent biopolymers. It is, therefore, possible that the structural moieties that constitute the ESC of biochar and NOM, as well as the E_h distributions of their ESC, are different. The E_h distributions of several humic acids

128

have been reported [35], but that of black carbon has not been fully delineated. In addition, it is still unclear which functional group(s) are contributing to the ESC of black carbon. Further studies are necessary to understand the formation mechanism of ESC of black carbon on the molecular level and how the formation mechanisms influence the E_h distribution. This information will be useful for predicting the availability of the ESC and its reactivity toward pollutants and for guiding the production of biochar with optimal ESC.

1.19 Surveying Black Carbon as a Global Electron Reservoir

The preliminary data in this dissertation show that black carbon generated from wildfires also possesses sizable, highly reversible, and potentially long-lasting ESC. Each year, wildfires affect about 4.5 million km^2 of the Earth's surface [90] and produce 117–389 million tons of black carbon through biomass burning [1]. These numbers are expected to magnify in the future with the increase in wildfires worldwide due to climate change. Like biochar, this pool of black carbon is derived thermally from lignocellulosic biomass, albeit under highly variable conditions. If ESC is shown to be common to all black carbon produced from wildfires and forest clearing, it would represent a large, yet previously unrecognized reservoir of rechargeable electrons and electron vacancies — a reservoir that may be an integral part of the biogeochemistry influencing the dynamics of the carbon cycle and the fate of redox-labile elements in the anaerobic subsurface. Therefore, it is important to survey the ESC of black carbon produced from wildfires, deforestation, and other thermal processes to evaluate the significance of black carbon as a global ESC reservoir. The methods developed in this dissertation will be an essential tool for such investigations.

1.20 Investigating the role of ESC in microbial redox processes

While this dissertation focuses on the chemical aspect of the ESC, previous research has shown that the ESC of black carbon is also accessible to microbes [6, 10, 25, 28]. For example, soil bacteria such as *Geobacter* and *Shewanella* species can utilize oxidized and reduced biochar as an electron acceptor and electron donor, respectively, for the oxidation of organic substrates such as acetate and lactate and for the reduction of nitrate [6, 28]. This is important because, through microbial access of the stored electrons in black carbon, many pollutants that cannot be abiotically degraded or adsorbed by black carbon (e.g., nitrate [44]) can be microbially degraded using biochar as an electron donor.

An important microbial process that may have a significant climate impact is the respiration of black carbon for anaerobic organic degradation. In anaerobic environments, the final step of organic degradation is methanogenesis, which converts compounds such as acetate into methane (CH_4) and carbon dioxide (CO_2), two major greenhouse gases. In the presence of an electron acceptor, however, acetate is oxidized to CO_2 via microbial respiration, suppressing fermentation and CH_4 production [72, 74]. On a per molecule basis, CH_4 is 25-fold more potent as a greenhouse gas than CO_2 over a 100-year horizon. By serving as an electron acceptor, black carbon may alter the biodegradation pathways and divert electron flow from fermentation to respiration in anaerobic ecosystems, resulting in markedly lower CH_4-to-CO_2 ratios. This altered greenhouse gas composition would decrease the radiative forcing by 92% per acetate molecule. Given the rechargeability and longevity of ESC of black carbon, black carbon may be an enormous regenerable electron acceptor for supporting organic oxidation and preventing CH_4 production in intermittently oxic/anoxic environments.

REFERENCES

1. Coppola, A. I.; Wiedemeier, D. B.; Hanke, U. M.; Reisser, M.; Abiven, S.; Schmidt, M. W. I.; Galy, V.; Voss, B.; Peucker-Ehrenbrink, B.; Eglinton, T. I.; Haghipour, N.; Nascimento, G. S.; Usman, M.; Blattmann, T. M.; Freymond, C. V.; Wacker, L.; Zhao, M.; Schefuss, E., Global-scale evidence for the refractory nature of riverine black carbon. *Nature Geoscience* **2018,** *11*, (8), 584-588.

2. Reisser, M.; Purves, R. S.; Schmidt, M. W. I.; Abiven, S., Pyrogenic carbon in soils: A literature-based inventory and a global estimation of its content in soil organic carbon and stocks. *Frontiers in Earth Science* **2016,** *4*, (80), pp.14.

3. Dominic, W.; James, E. A.; Street-Perrott, F. A.; Johannes, L.; Stephen, J., Sustainable biochar to mitigate global climate change. *Nature Communications* **2010**, pp. 9.

4. Lehmann, J.; Rillig, M. C.; Thies, J.; Masiello, C. A.; Hockaday, W. C.; Crowley, D., Biochar effects on soil biota - A review. *Soil Biology & Biochemistry* **2011,** *43*, (9), 1812-1836.

5. Klüpfel, L.; Keiluweit, M.; Kleber, M.; Sander, M., Redox properties of plant biomass-derived black carbon (biochar). *Environmental Science & Technology* **2014,** *48*, (10), 5601-5611.

6. Saquing, J. M.; Yu, Y. H.; Chiu, P. C., Wood-derived black carbon (biochar) as a microbial electron donor and acceptor. *Environmental Science & Technology Letters* **2016,** *3*, (2), 62-66.

7. Xu, W. Q.; Dana, K. E.; Mitch, W. A., Black carbon-mediated destruction of nitroglycerin and RDX by hydrogen sulfide. *Environmental Science & Technology* **2010,** *44*, (16), 6409-6415.

8. Li, J.; Li, Q.; Steinberg, C. E.; Zhao, Q.; Pan, B.; Pignatello, J. J.; Xing, B., Reaction of substituted phenols with lignin char: Dual oxidative and reductive pathways depending on substituents and conditions. *Environmental Science & Technology* **2020,** *54*, 15811-15820.

9.   Liang, Z.; Min, W.; Guo-juan, W., Electron exchange capacity of rice biochar at different preparation temperatures. *China Environmental Science* **2019,** *39*, (10), 4329-4336.

10.   Zhang, X. Q.; Xia, J.; Pu, J. Y.; Cai, C.; Tyson, G. W.; Yuan, Z. G.; Hu, S. H., Biochar-mediated anaerobic oxidation of methane. *Environmental Science & Technology* **2019,** *53*, (12), 6660-6668.

11.   Zhang, Y.; Xu, X. Y.; Cao, L. Z.; Ok, Y. S.; Cao, X. D., Characterization and quantification of electron donating capacity and its structure dependence in biochar derived from three waste biomasses. *Chemosphere* **2018,** *211*, 1073-1081.

12.   Zhang, Y.; Xu, X. Y.; Zhang, P. Y.; Zhao, L.; Qiu, H.; Cao, X. D., Pyrolysis-temperature depended quinone and carbonyl groups as the electron accepting sites in barley grass derived biochar. *Chemosphere* **2019,** *232*, 273-280.

13.   Chacón, F. J.; Sanchez-Monedero, M. A.; Cayuela, M. L.; Lezama, L., Enhancing biochar redox properties through feedstock selection, metal preloading and post-pyrolysis treatments. *Chemical Engineering Journal* **2020,** *395*, 125100.

14.   Li, S.; Shao, L.; Zhang, H.; He, P.; Lu, F., Quantifying the contributions of surface area and redox-active moieties to electron exchange capacities of biochar. *Journal of Hazardous Materials* **2020,** *394*, 122541.

15.   Rowell, R. M., In *The Chemistry of Solid Wood*, American Chemical Society: Washington D.C., United States, 1984.

16.   Cornelissen, G.; Gustafsson, Ö.; Bucheli, T. D.; Jonker, M. T.; Koelmans, A. A.; van Noort, P. C., Extensive sorption of organic compounds to black carbon, coal, and kerogen in sediments and soils: mechanisms and consequences for distribution, bioaccumulation, and biodegradation. *Environmental Science & Technology* **2005,** *39*, (18), 6881-6895.

17.   Plata, D. L.; Hemingway, J. D.; Gschwend, P. M., Polyparameter linear free energy relationship for wood char–water sorption coefficients of organic sorbates. *Environmental Toxicology & Chemistry* **2015,** *34*, (7), 1464-1471.

18.   Oh, S. Y.; Cha, D. K.; Chiu, P. C., Graphite-mediated reduction of 2,4-dinitrotoluene with elemental iron. *Environmental Science & Technology* **2002,** *36*, (10), 2178-2184.

19. Ye, J. C.; Chiu, P. C., Transport of atomic hydrogen through graphite and its reaction with azoaromatic compounds. *Environmental Science & Technology* **2006,** *40*, (12), 3959-3964.

20. Kemper, J. M.; Ammar, E.; Mitch, W. A., Abiotic degradation of hexahydro-1,3,5-trinitro-1,3,5-triazine in the presence of hydrogen sulfide and black carbon. *Environmental Science & Technology* **2008,** *42*, (6), 2118-2123.

21. Oh, S. Y.; Chiu, P. C., Graphite- and soot-mediated reduction of 2,4-dinitrotoluene and hexahydro-1,3,5-trinitro-1,3,5-triazine. *Environmental Science & Technology* **2009,** *43*, (18), 6983-6988.

22. Oh, S. Y.; Son, J. G.; Hur, S. H.; Chung, J. S.; Chiu, P. C., Black carbon-mediated reduction of 2,4-dinitrotoluene by dithiothreitol. *Journal of Environmental Quality* **2013,** *42*, (3), 815-821.

23. Oh, S. Y.; Son, J. G.; Chiu, P. C., Biochar-mediated reductive transformation of nitro herbicides and explosives. *Environmental Toxicology & Chemistry* **2013,** *32*, (3), 501-508.

24. Klüepfel, L.; Keiluweit, M.; Kleber, M.; Sander, M., Redox properties of plant biomass-derived black carbon (biochar). *Environ Sci Technol* **2014,** *48*, (10), 5601-5611.

25. Chen, S. S.; Rotaru, A. E.; Shrestha, P. M.; Malvankar, N. S.; Liu, F. H.; Fan, W.; Nevin, K. P.; Lovley, D. R., Promoting interspecies electron transfer with biochar. *Scientific Reports* **2014,** *4*, (5019), pp.7.

26. Yu, L. P.; Yuan, Y.; Tang, J.; Wang, Y. Q.; Zhou, S. G., Biochar as an electron shuttle for reductive dechlorination of pentachlorophenol by *Geobacter sulfurreducens*. *Scientific Reports* **2015,** *5*, (16221), pp.10.

27. Pignatello, J. J.; Mitch, W. A.; Xu, W. Q., Activity and reactivity of pyrogenic carbonaceous matter toward organic compounds. *Environmental Science & Technology* **2017,** *51*, (16), 8893-8908.

28. Kappler, A.; Wuestner, M. L.; Ruecker, A.; Harter, J.; Halama, M.; Behrens, S., Biochar as an electron shuttle between bacteria and Fe (III) minerals. *Environmental Science & Technology Letters* **2014,** *1*, (8), 339-344.

29. Xu, S.; Adhikari, D.; Huang, R.; Zhang, H.; Tang, Y.; Roden, E.; Yang, Y., Biochar-facilitated microbial reduction of hematite. *Environmental Science & Technology* **2016,** *50*, (5), 2389-2395.

30. Oh, S.-Y.; Cha, D. K.; Kim, B. J.; Chiu, P. C., Reduction of nitroglycerin with elemental iron: pathway, kinetics, and mechanisms. *Environmental Science & Technology* **2004,** *38*, (13), 3723-3730.

31. Sun, T. R.; Levin, B. D. A.; Guzman, J. J. L.; Enders, A.; Muller, D. A.; Angenent, L. T.; Lehmann, J., Rapid electron transfer by the carbon matrix in natural pyrogenic carbon. *Nature Communications* **2017,** *8*, (14873), pp.12.

32. Xiao, X.; Chen, B., A direct observation of the fine aromatic clusters and molecular structures of biochars. *Environmental Science & Technology* **2017,** *51*, (10), 5473-5482.

33. Sander, M.; Hofstetter, T. B.; Gorski, C. A., Electrochemical analyses of redox-active iron minerals: A review of nonmediated and mediated approaches. *Environmental Science & Technology* **2015,** *49*, (10), 5862-5878.

34. Aeschbacher, M.; Sander, M.; Schwarzenbach, R. P., Novel electrochemical approach to assess the redox properties of humic substances. *Environmental Science & Technology* **2010,** *44*, (1), 87-93.

35. Aeschbacher, M.; Vergari, D.; Schwarzenbach, R. P.; Sander, M., Electrochemical analysis of proton and electron transfer equilibria of the reducible moieties in humic acids. *Environmental Science & Technology* **2011,** *45*, (19), 8385-8394.

36. Aeschbacher, M.; Graf, C.; Schwarzenbach, R. P.; Sander, M., Antioxidant properties of humic substances. *Environmental Science & Technology* **2012,** *46*, (9), 4916-4925.

37. Gorski, C. A.; Aeschbacher, M.; Soltermann, D.; Voegelin, A.; Baeyens, B.; Marques Fernandes, M.; Hofstetter, T. B.; Sander, M., Redox properties of structural fe in clay minerals. 1. Electrochemical quantification of electron-donating and -accepting capacities of smectites. *Environmental Science & Technology* **2012,** *46*, (17), 9360-9368.

38. Gorski, C. A.; Klüpfel, L. E.; Voegelin, A.; Sander, M.; Hofstetter, T. B., Redox properties of structural Fe in clay minerals: 3. Relationships between smectite redox and structural properties. *Environmental Science & Technology* **2013,** *47*, (23), 13477-13485.

39. Gorski, C. A.; Klüpfel, L.; Voegelin, A.; Sander, M.; Hofstetter, T. B., Redox properties of structural Fe in clay minerals. 2. Electrochemical and spectroscopic characterization of electron transfer irreversibility in ferruginous smectite, SWa-1. *Environmental Science & Technology* **2012,** *46*, (17), 9369-9377.

40. Aeppli, M.; Voegelin, A.; Gorski, C. A.; Hofstetter, T. B.; Sander, M., Mediated electrochemical reduction of iron (oxyhydr-)oxides under defined thermodynamic boundary conditions. *Environmental Science & Technology* **2018,** *52*, (2), 560-570.

41. Wang, H.; Zhao, H.; Zhu, L., Role of pyrogenic carbon in parallel microbial reduction of nitrobenzene in the liquid and sorbed phases. *Environmental Science & Technology* **2020,** *54*, 8760-8769.

42. Walpen, N.; Schroth, M. H.; Sander, M., Quantification of phenolic antioxidant moieties in dissolved organic matter by flow-injection analysis with electrochemical detection. *Environmental Science & Technology* **2016,** *50*, (12), 6423-6432.

43. Prévoteau, A.; Ronsse, F.; Cid, I.; Boeckx, P.; Rabaey, K., The electron donating capacity of biochar is dramatically underestimated. *Scientific Reports* **2016,** *6* (32870), pp.11.

44. Tian, J.; Jin, J.; Chiu, P. C.; Cha, D. K.; Guo, M. X.; Imhoff, P. T., A pilot-scale, bi-layer bioretention system with biochar and zero-valent iron for enhanced nitrate removal from stormwater. *Water Research* **2019,** *148*, 378-387.

45. Zehnder, A.; Wuhrmann, K., Titanium (III) citrate as a nontoxic oxidation-reduction buffering system for the culture of obligate anaerobes. *Science* **1976,** *194*, (4270), 1165-1166.

46. Mayhew, S. G., The redox potential of dithionite and SO_2^- from equilibrium reactions with flavodoxins, methyl viologen and hydrogen plus hydrogenase. *European Journal of Biochemistry* **1978,** *85*, (2), 535-547.

47. O'Reilly, J. E., Oxidation-reduction potential of the ferro-ferricyanide system in buffer solutions. *Biochimica et Biophysica Acta-Bioenergetics* **1973,** *292*, (3), 509-515.

48. Wood, P. M., The potential diagram for oxygen at pH 7. *Biochemical Journal* **1988,** *253*, (1), 287.

49. Hirschman, D. J.; Seipp, B.; Schueler, T., Performance enhancing devices for stormwater best management practices. **2017**, pp.38.

50. Yi, S. The impact of biochar surface properties on sand and sandy loam regarding water repellency, water retention, and gas transmissivity. Ph.D. Dissertation, University of Delaware, Newark, DE, 2018.

51. Hoving, A. L.; Sander, M.; Bruggeman, C.; Behrends, T., Redox properties of clay-rich sediments as assessed by mediated electrochemical analysis: separating pyrite, siderite and structural Fe in clay minerals. *Chemical Geology* **2017,** *457*, 149-161.

52. Amonette, J.; Szecsody, J.; Schaef, H.; Gorby, Y.; Fruchter, J.; Templeton, J. *Abiotic reduction of aquifer materials by dithionite: a promising in-situ remediation technology*; Pacific Northwest Lab., Richland, WA, United States: 1994.

53. Nakhli, S. A. A. Biochar for stormwater runoff and nitrate load reduction: Models, tools, and data. Ph.D. Dissertation, University of Delaware, Newark, DE, 2020.

54. Nakhli, S. A. A.; Panta, S.; Brown, J. D.; Tian, J.; Imhoff, P. T., Quantifying biochar content in a field soil with varying organic matter content using a two-temperature loss on ignition method. *Science of The Total Environment* **2019,** *658*, 1106-1116.

55. Gomez-Eyles, J. L.; Yupanqui, C.; Beckingham, B.; Riedel, G.; Gilmour, C.; Ghosh, U., Evaluation of biochars and activated carbons for in situ remediation of sediments impacted with organics, mercury, and methylmercury. *Environmental Science & Technology* **2013,** *47*, (23), 13721-13729.

56. The California Department of Forestry and Fire Protection (CAL FIRE). https://www.fire.ca.gov/incidents/2019/

57. Arnold, W. A.; Ball, W. P.; Roberts, A. L., Polychlorinated ethane reaction with zero-valent zinc: pathways and rate control. *Journal of Contaminant Hydrology* **1999,** *40*, (2), 183-200.

58. Wen, C. Y., Noncatalytic heterogeneous solid fluid reaction models. *Industrial and Engineering Chemistry* **1968,** *60*, (9), 34-54.

59. Xin, D.; Xian, M.; Chiu, P. C., New methods for assessing electron storage capacity and redox reversibility of biochar. *Chemosphere* **2019,** *215*, 827-834.

60.   Lawrinenko, M. Anion exchange capacity of biochar. Master Thesis, Iowa State University, Ames, IA, 2014.

61.   Michelson, K.; Sanford, R. A.; Valocchi, A. J.; Werth, C. J., Nanowires of *Geobacter sulfurreducens* require redox cofactors to reduce metals in pore spaces too small for cell passage. *Environmental Science & Technology* **2017,** *51*, (20), 11660-11668.

62.   Lovley, D. R.; Ueki, T.; Zhang, T.; Malvankar, N. S.; Shrestha, P. M.; Flanagan, K. A.; Aklujkar, M.; Butler, J. E.; Giloteaux, L.; Rotaru, A.-E., Geobacter: the microbe electric's physiology, ecology, and practical applications. *Advances in Microbial Physiology* **2011,** *59*, 1-100.

63.   Maurer, F.; Christl, I.; Kretzschmar, R. J. E. s.; technology, Reduction and reoxidation of humic acid: Influence on spectroscopic properties and proton binding. **2010,** *44*, (15), 5787-5792.

64.   Lau, M. P.; Sander, M.; Gelbrecht, J.; Hupfer, M., Solid phases as important electron acceptors in freshwater organic sediments. *Biogeochemistry* **2015,** *123*, (1), 49-61.

65.   Bird, M. I., Wynn, J. G., Saiz, G., Wurster, C. M., & McBeath, A. The pyrogenic carbon cycle. Annual Review of Earth and Planetary Sciences. *The pyrogenic carbon cycle: Annual Review of Earth and Planetary Sciences*; 2015; pp 273-298.

66.   Inyang, M.; Dickenson, E., The potential role of biochar in the removal of organic and microbial contaminants from potable and reuse water: A Review. *Chemosphere* **2015,** *134*, 232-240.

67.   Joseph, S.; Husson, O.; Graber, E. R.; van Zwieten, L.; Taherymoosavi, S.; Thomas, T.; Nielsen, S.; Ye, J.; Pan, G. X.; Chia, C.; Munroe, P.; Allen, J.; Lin, Y.; Fan, X. R.; Donne, S., The electrochemical properties of biochars and how they affect soil redox properties and processes. *Agronomy-Basel* **2015,** *5*, (3), 322-340.

68.   Yuan, Y.; Bolan, N.; Prevoteau, A.; Vithanage, M.; Biswas, J. K.; Ok, Y. S.; Wang, H. L., Applications of biochar in redox-mediated reactions. *Bioresource Technology* **2017,** *246*, 271-281.

69.   Cao, X. Y.; Pignatello, J. J.; Li, Y.; Lattao, C.; Chappell, M. A.; Chen, N.; Miller, L. F.; Mao, J. D., Characterization of wood chars produced at different temperatures using advanced solid-state C-13 NMR spectroscopic techniques. *Energy & Fuels* **2012,** *26*, (9), 5983-5991.

70. Xin, D. H.; Xian, M. H.; Chiu, P. C., New methods for assessing electron storage capacity and redox reversibility of biochar. *Chemosphere* **2019,** *215*, 827-834.

71. Xin, D.; Xian, M.; Chiu, P. C., Chemical methods for determining the electron storage capacity of black carbon. *MethodsX* **2018,** *5*, 1515-1520.

72. Klüpfel, L.; Piepenbrock, A.; Kappler, A.; Sander, M., Humic substances as fully regenerable electron acceptors in recurrently anoxic environments. *Nature Geoscience* **2014,** *7*, (3), 195-200.

73. Walpen, N.; Getzinger, G. J.; Schroth, M. H.; Sander, M., Electron-donating phenolic and electron-accepting quinone moieties in peat dissolved organic matter: Quantities and redox transformations in the context of peat biogeochemistry. *Environmental Science & Technology* **2018,** *52*, (9), 5236-5245.

74. Gao, C. Y.; Sander, M.; Agethen, S.; Knorr, K. H., Electron accepting capacity of dissolved and particulate organic matter control CO_2 and CH_4 formation in peat soils. *Geochimica Et Cosmochimica Acta* **2019,** *245*, 266-277.

75. Michelson, K.; Alcalde, R. E.; Sanford, R. A.; Valocchi, A. J.; Werth, C. J., Diffusion-based recycling of flavins allows *Shewanella oneidensis* MR-1 to yield energy from metal reduction across physical separations. *Environmental Science & Technology* **2019,** *53*, (7), 3480-3487.

76. Zhou, Y. Y.; Liu, X. C.; Xiang, Y. J.; Wang, P.; Zhang, J. C.; Zhang, F. F.; Wei, J. H.; Luo, L.; Lei, M.; Tang, L., Modification of biochar derived from sawdust and its application in removal of tetracycline and copper from aqueous solution: Adsorption mechanism and modelling. *Bioresource Technology* **2017,** *245*, 266-273.

77. Mukherjee, A.; Zimmerman, A. R.; Harris, W., Surface chemistry variations among a series of laboratory-produced biochars. *Geoderma* **2011,** *163*, (3-4), 247-255.

78. Gebru, H.; Cui, S. D.; Li, Z. J.; Wang, X.; Pan, X. F.; Liu, J. J.; Guo, K., Facile pH-dependent synthesis and characterization of catechol stabilized silver nanoparticles for catalytic reduction of 4-nitrophenol. *Catalysis Letters* **2017,** *147*, (8), 2134-2143.

79. James, T. H., The reduction of silver ions by hydroquinone. *Journal of the American Chemical Society* **1939,** *61*, 648-652.

80.   Jacob, J. A.; Mahal, H. S.; Biswas, N.; Mukherjee, T.; Kapoor, S., Role of phenol derivatives in the formation of silver nanoparticles. *Langmuir* **2008,** *24*, (2), 528-533.

81.   Yao, Y.; Gao, B.; Wu, F.; Zhang, C. Z.; Yang, L. Y., Engineered biochar from biofuel residue: Characterization and its silver removal potential. *ACS Applied Materials & Interfaces* **2015,** *7*, (19), 10634-10640.

82.   Schwarzenbach, R. P.; Gschwend, P. M.; Imboden, D. M., *Environmental Organic Chemistry, 2nd ed.* John Wiley& Sons: Hoboken: NJ, 2003.

83.   Lin, Q. Q.; Li, Q.; Batchelor-McAuley, C.; Compton, R. G., Two-electron, two-proton oxidation of catechol: Kinetics and apparent catalysis. *Journal of Physical Chemistry C* **2015,** *119*, (3), 1489-1495.

84.   Nakhli, S. A. A.; Imhoff, P. T., Models for predicting water retention in pyrogenic carbon (biochar) and biochar-amended soil at low water contents. *Water Resources Research* **2020,** *56*, (11), e2020WR027726.

85.   Ling, L.; Tang, C. L.; Zhang, W. X., Visualization of silver nanoparticle formation on nanoscale zero-valent iron. *Environmental Science & Technology Letters* **2018,** *5*, (8), 520-525.

86.   Sun, Y. G.; Yin, Y. D.; Mayers, B. T.; Herricks, T.; Xia, Y. N., Uniform silver nanowires synthesis by reducing $AgNO_3$ with ethylene glycol in the presence of seeds and poly(vinyl pyrrolidone). *Chemistry of Materials* **2002,** *14*, (11), 4736-4745.

87.   Silva, L. P.; Silveira, A. P.; Bonatto, C. C.; Reis, I. G.; Milreu, P. V., Silver nanoparticles as antimicrobial agents: Past, present, and future. *Nanostructures for Antimicrobial Therapy* **2017**, 577-596.

88.   Bird, M. I.; Wynn, J. G.; Saiz, G.; Wurster, C. M.; McBeath, A., The pyrogenic carbon cycle. *Annual Review of Earth and Planetary Sciences*. **2015,** *43*, 273-298.

89.   Landry, J. S.; Matthews, H. D., The global pyrogenic carbon cycle and its impact on the level of atmospheric CO_2 over past and future centuries. *Global Change Biology* **2017,** *23*, (8), 3205-3218.

90.   Santin, C.; Doerr, S. H.; Preston, C. M.; Gonzalez-Rodriguez, G., Pyrogenic organic matter production from wildfires: a missing sink in the global carbon cycle. *Global Change Biology* **2015,** *21*, (4), 1621-1633.

91. Manya, J. J., Pyrolysis for biochar purposes: A review to establish current knowledge gaps and research needs. *Environmental Science & Technology* **2012,** *46*, (15), 7939-7954.

92. Xie, T.; Reddy, K. R.; Wang, C. W.; Yargicoglu, E.; Spokas, K., Characteristics and applications of biochar for environmental remediation: A review. *Crit Rev Env Sci Tec* **2015,** *45*, (9), 939-969.

93. Inyang, M. I.; Gao, B.; Yao, Y.; Xue, Y. W.; Zimmerman, A.; Mosa, A.; Pullammanappallil, P.; Ok, Y. S.; Cao, X. D., A review of biochar as a low-cost adsorbent for aqueous heavy metal removal. *Crit Rev Env Sci Tec* **2016,** *46*, (4), 406-433.

94. Zhong, D. L.; Jiang, Y.; Zhao, Z. Z.; Wang, L. L.; Chen, J.; Ren, S. P.; Liu, Z. H.; Zhang, Y. R.; Tsang, D. C. W.; Crittenden, J. C., pH dependence of arsenic oxidation by rice-husk-derived biochar: Roles of redox-active moieties. *Environmental Science & Technology* **2019,** *53*, (15), 9034-9044.

95. Liu, P.; Ptacek, C. J.; Blowes, D. W.; Finfrock, Y. Z.; Liu, Y. Y., Characterization of chromium species and distribution during Cr(VI) removal by biochar using confocal micro-X-ray fluorescence redox mapping and X-ray absorption spectroscopy. *Environment International* **2020,** *134*, 105216.

96. Xin, D.; Barkley, T.; Chiu, P. C., Visualizing electron storage capacity distribution in biochar through silver tagging. *Chemosphere* **2020,** *248*, 125952.

97. Xin, D.; Chiu, P. C., Visualizing the distribution of black carbon's electron storage capacity using silver. *MethodsX* **2020,** *7*.

98. Ho, S. H.; Zhu, S. S.; Chang, J. S., Recent advances in nanoscale-metal assisted biochar derived from waste biomass used for heavy metals removal. *Bioresource Technology* **2017,** *246*, 123-134.

99. Mian, M. M.; Liu, G. J., Recent progress in biochar-supported photocatalysts: synthesis, role of biochar, and applications. *RSC Advances* **2018,** *8*, (26), 14237-14248.

100. Saha, N.; Xin, D.; Chiu, P. C.; Reza, M. T., Effect of pyrolysis temperature on acidic oxygen-containing functional groups and electron storage capacities of pyrolyzed hydrochars. *ACS Sustainable Chemistry & Engineering* **2019,** *7*, (9), 8387-8396.

101. Yu, J.; Paterson, N.; Blamey, J.; Millan, M., Cellulose, xylan and lignin interactions during pyrolysis of lignocellulosic biomass. *Fuel* **2017,** *191*, 140-149.

102. Zhao, C. X.; Jiang, E. C.; Chen, A. H., Volatile production from pyrolysis of cellulose, hemicellulose and lignin. *Journal of the Energy Institute* **2017,** *90*, (6), 902-913.

103. Yeo, J. Y.; Chin, B. L. F.; Tan, J. K.; Loh, Y. S., Comparative studies on the pyrolysis of cellulose, hemicellulose, and lignin based on combined kinetics. *Journal of the Energy Institute* **2019,** *92*, (1), 27-37.

104. Lu, Q.; Yang, X. C.; Dong, C. Q.; Zhang, Z. F.; Zhang, X. M.; Zhu, X. F., Influence of pyrolysis temperature and time on the cellulose fast pyrolysis products: Analytical Py-GC/MS study. *Journal of Analytical and Applied Pyrolysis* **2011,** *92*, (2), 430-438.

105. Peng, Y. Y.; Wu, S. B., The structural and thermal characteristics of wheat straw hemicellulose. *Journal of Analytical and Applied Pyrolysis* **2010,** *88*, (2), 134-139.

106. Liu, C.; Hu, J.; Zhang, H. Y.; Xiao, R., Thermal conversion of lignin to phenols: Relevance between chemical structure and pyrolysis behaviors. *Fuel* **2016,** *182*, 864-870.

107. Pang, C. H.; Gaddipatti, S.; Tucker, G.; Lester, E.; Wu, T., Relationship between thermal behaviour of lignocellulosic components and properties of biomass. *Bioresource Technology* **2014,** *172*, 312-320.

108. Yang, H. P.; Yan, R.; Chen, H. P.; Zheng, C. G.; Lee, D. H.; Liang, D. T., In-depth investigation of biomass pyrolysis based on three major components: Hemicellulose, cellulose and lignin. *Energy & Fuels* **2006,** *20*, (1), 388-393.

109. Reza, M. T. Upgrading biomass by hydrothermal and chemical conditioning. Ph.D. Dissertation, University of Nevada, Reno, Reno, NV, 2013.

110. Koch, B. P.; Dittmar, T., From mass to structure: an aromaticity index for high-resolution mass data of natural organic matter. *Rapid Communications in Mass Spectrometry* **2006,** *20*, (1), 926-936.

111. Mao, J. D.; Cao, X. Y.; Olk, D. C.; Chu, W. Y.; Schmidt-Rohr, K., Advanced solid-state NMR spectroscopy of natural organic matter. *Progress in Nuclear Magnetic Resonance Spectroscopy* **2017,** *100*, 17-51.

112. Johnson, R. L.; Schmidt-Rohr, K., Quantitative solid-state C-13 NMR with signal enhancement by multiple cross polarization. *Journal of Magnetic Resonance* **2014,** *239*, 44-49.

113. Bostick, K. W.; Zimmerman, A. R.; Wozniak, A. S.; Mitra, S.; Hatcher, P. G., Production and composition of pyrogenic dissolved organic matter from a logical series of laboratory-generated chars. *Frontiers in Earth Science* **2018,** *6*, pp. 14.

114. Song, Y.; Jiang, J.; Ma, J.; Pang, S. Y.; Liu, Y. Z.; Yang, Y.; Luo, C. W.; Zhang, J. Q.; Gu, J.; Qin, W., ABTS as an electron shuttle to enhance the oxidation kinetics of substituted phenols by aqueous permanganate. *Environmental Science & Technology* **2015,** *49*, (19), 11764-11771.

115. Song, Y.; Jiang, J.; Qin, W.; Li, J.; Zhou, Y.; Gao, Y., Enhanced transformation of organic pollutants by mild oxidants in the presence of synthetic or natural redox mediators: A review. *Water Research* **2020**, 116667.

116. Maurer, F.; Christl, I.; Kretzschmar, R., Reduction and reoxidation of humic acid: Influence on spectroscopic properties and proton binding. *Environmental Science & Technology* **2010,** *44*, (15), 5787-5792.

117. Afsar, M. Z.; Goodwin, C.; Beebe, T. P., Jr.; Jaisi, D. P.; Jin, Y., Quantification and molecular characterization of organo-mineral associations as influenced by redox oscillations. *Science of The Total Environment* **2020,** *704*, 135454.

118. Williams, C. L.; Emerson, R. M.; Tumuluru, J. S., Biomass compositional analysis for conversion to renewable fuels and chemicals. In *Biomass Volume Estimation and Valorization for Energy*, 2017; pp 251-270.

119. Walsh, M. R.; Walsh, M. E.; Ramsey, C. A.; Thiboutot, S.; Ampleman, G.; Diaz, E.; Zufelt, J. E., Energetic residues from the detonation of IMX-104 insensitive munitions. *Propellants, Explosives, Pyrotechnics* **2014,** *39*, (2), 243-250.

120. Dontsova, K.; Taylor, S.; Pesce-Rodriguez, R. *Dissolution of NTO, DNAN and insensitive munitions formulations and their fates in soils*; University of Arizona Tuscon, United States, 2018.

121. Le Campion, L.; Vandais, A.; Ouazzani, J. J. F. m. l., Microbial remediation of NTO in aqueous industrial wastes. **1999,** *176*, (1), 197-203.

122. Johnson, M. S.; Eck, W. S.; Lent, E. M., Toxicity of insensitive munition (IMX) formulations and components. *Propellants, Explosives, Pyrotechnics* **2017,** *42*, (1), 9-16.

123. Halasz, A.; Hawari, J.; Perreault, N. N., New insights into the photochemical degradation of the insensitive munition formulation IMX-101 in water. *Environmental Science & Technology* **2018,** *52*, (2), 589-596.

124. Mašek, O. e.; Buss, W.; Sohi, S., Standard biochar materials. *Environmental Science & Technology* **2018,** *52*, (17), 9543-9544.

125. Oh, S. Y.; Seo, Y. D., Sorptive removal of nitro explosives and metals using biochar. *Journal of Environmental Quality* **2014,** *43*, (5), 1663-1671.

126. Oh, S. Y.; Seo, Y. D., Factors affecting sorption of nitro explosives to biochar: Pyrolysis temperature, surface treatment, competition, and dissolved metals. *Journal of Environmental Quality* **2015,** *44*, (3), 833-840.

127. Lee, K.-Y.; Chapman, L. B.; Cobura, M. D., 3-Nitro-1, 2, 4-triazol-5-one, a less sensitive explosive. *Journal of Energetic Materials* **1987,** *5*, (1), 27-33.

128. Cárdenas-Hernández, P. A.; Anderson, K. A.; Murillo-Gelvez, J.; Di Toro, D. M.; Allen, H. E.; Carbonaro, R. F.; Chiu, P. C., Reduction of 3-nitro-1, 2, 4-triazol-5-one (NTO) by the hematite–aqueous Fe (II) redox couple. *Environmental Science & Technology* **2020,** *54*, (19), 12191-12201.

129. Xin, D.; Saha, N.; Reza, M. T.; Hudson, J.; Chiu, P. C., Pyrolysis creates electron storage capacity of black carbon (biochar) from lignocellulosic biomass. *ACS Sustainable Chemistry & Engineering* **2021** *9*, (19), 6821-6831.

130. Temple, T.; Cipullo, S.; Galante, E.; Ladyman, M.; Mai, N.; Parry, T.; Coulon, F., The effect of soil type on the extraction of insensitive high explosive constituents using four conventional methods. *Science of The Total Environment* **2019,** *668*, 184-192.

131. Liang, J.; Olivares, C.; Field, J. A.; Sierra-Alvarez, R., Microbial toxicity of the insensitive munitions compound, 2, 4-dinitroanisole (DNAN), and its aromatic amine metabolites. *Journal of Hazardous Materials* **2013,** *262*, 281-287.

132. Bernstein, A.; Ronen, Z.; Gelman, F., Insight on RDX degradation mechanism by Rhodococcus strains using ^{13}C and ^{15}N kinetic isotope effects. *Environmental Science & Technology* **2013,** *47*, (1), 479-484.

133. Tong, Y.; Berens, M. J.; Ulrich, B. A.; Bolotin, J.; Strehlau, J. H.; Hofstetter, T. B.; Arnold, W. A., Exploring the utility of compound-specific isotope analysis for assessing ferrous iron-mediated reduction of RDX in the subsurface. *Environmental Science & Technology* **2021,** *55*, (10), 6752-6763.

134. Linker, B. R.; Khatiwada, R.; Perdrial, N.; Abrell, L.; Sierra-Alvarez, R.; Field, J. A.; Chorover, J., Adsorption of novel insensitive munitions compounds at clay mineral and metal oxide surfaces. *Environmental Chemistry* **2015,** *12*, (1), 74-84.

135. Khatiwada, R.; Abrell, L.; Li, G.; Root, R. A.; Sierra-Alvarez, R.; Field, J. A.; Chorover, J., Adsorption and oxidation of 3-nitro-1, 2, 4-triazole-5-one (NTO) and its transformation product (3-amino-1, 2, 4-triazole-5-one, ATO) at ferrihydrite and birnessite surfaces. *Environmental Pollution* **2018,** *240*, 200-208.

136. Krzmarzick, M. J.; Khatiwada, R.; Olivares, C. I.; Abrell, L.; Sierra-Alvarez, R.; Chorover, J.; Field, J. A., Biotransformation and degradation of the insensitive munitions compound, 3-nitro-1,2,4-triazol-5-one, by soil bacterial communities. *Environmental Science & Technology* **2015,** *49*, (9), 5681-5688.

137. Madeira, C. L.; Speet, S. A.; Nieto, C. A.; Abrell, L.; Chorover, J.; Sierra-Alvarez, R.; Field, J. A., Sequential anaerobic-aerobic biodegradation of emerging insensitive munitions compound 3-nitro-1, 2, 4-triazol-5-one (NTO). *Chemosphere* **2017,** *167*, 478-484.

138. Mark, N.; Arthur, J.; Dontsova, K.; Brusseau, M.; Taylor, S., Adsorption and attenuation behavior of 3-nitro-1,2,4-triazol-5-one (NTO) in eleven soils. *Chemosphere* **2016,** *144*, 1249-1255.

139. Madeira, C. L.; Jog, K. V.; Vanover, E. T.; Brooks, M. D.; Taylor, D. K.; Sierra-Alvarez, R.; Waidner, L. A.; Spain, J. C.; Krzmarzick, M. J.; Field, J. A., Microbial enrichment culture responsible for the complete oxidative biodegradation of 3-amino-1, 2, 4-triazol-5-one (ATO), the reduced daughter product of the insensitive munitions compound 3-nitro-1, 2, 4-triazol-5-one (NTO). *Environmental Science & Technology* **2019,** *53*, (21), 12648-12656.

140. Haag, W. R.; Spanggord, R.; Mill, T.; Podoll, R. T.; Chou, T. W.; Tse, D. S.; Harper, J. C., Aquatic environmental fate of nitroguanidine. *Environmental Toxicology & Chemistry* **1990,** *9*, (11), 1359-1367.

141. Koutsospyros, A.; Pavlov, J.; Fawcett, J.; Strickland, D.; Smolinski, B.; Braida, W., Degradation of high energetic and insensitive munitions compounds by Fe/Cu bimetal reduction. *Journal of Hazardous Materials* **2012,** *219*, 75-81.

142. Oh, S. Y.; Cha, D. K.; Kim, B. J.; Chiu, P. C., Reductive transformation of hexahydro-1, 3, 5-trinitro-1, 3, 5-triazine, octahydro-1, 3, 5, 7-tetranitro-1, 3, 5, 7-tetrazocine, and methylenedinitramine with elemental iron. *Environmental Toxicology & Chemistry: An International Journal* **2005,** *24*, (11), 2812-2819.

143. Liu, P. Stabilization of mercury in river water and sediment using biochars. University of Waterloo, Ontario, Canada, 2016.

144. Peterson, M. J.; Mayes, M. A.; Brooks, S. C.; Mathews, T. J.; Johs, A.; Rodriguez, L. G.; DeRolph, C. R.; Pierce, E. M.; Watson, D. B.; Muller, K. A. *Mercury remediation technology development for Lower East Fork Poplar Creek—FY 2017 Progress Report* Oak Ridge National Lab.(ORNL), Oak Ridge, TN (United States): 2018.

145. Scott, D. T.; McKnight, D. M.; Blunt-Harris, E. L.; Kolesar, S. E.; Lovley, D. R., Quinone moieties act as electron acceptors in the reduction of humic substances by humics-reducing microorganisms. *Environmental Science & Technology* **1998,** *32*, (19), 2984-2989.

146. Wallace, G. C.; Sander, M.; Chin, Y. P.; Arnold, W. A., Quantifying the electron donating capacities of sulfide and dissolved organic matter in sediment pore waters of wetlands. *Environmental Science: Processes & Impacts* **2017,** *19*, (5), 758-767.

147. Adani, F.; Spagnol, M.; Genevini, P., Biochemical origin and refractory properties of humic acid extracted from the maize plant. *Biogeochemistry* **2006,** *78*, (1), 85-96.

148. Mostofa, K. M.; Liu, C.; Mottaleb, M. A.; Wan, G.; Ogawa, H.; Vione, D.; Yoshioka, T.; Wu, F., Photobiogeochemistry of organic matter In *Dissolved Organic Matter in Natural Waters*, Springer: Berlin, Heidelberg, 2013; pp 1-137.

149. Stumm, W. M., J. J., Aquatic chemistry: chemical equilibria and rates in natural waters. 3rd ed.; Wiley: New York: 1996.

150. Nurchi, V. M.; Pivetta, T.; Lachowicz, J. I.; Crisponi, G., Effect of substituents on complex stability aimed at designing new iron(III) and aluminum(III) chelators. *Journal of Inorganic Biochemistry* **2009,** *103*, (2), 227-236.

151. Quan, M.; Sanchez, D.; Wasylkiw, M. F.; Smith, D. K., Voltammetry of quinones in unbuffered aqueous solution: Reassessing the roles of proton transfer and hydrogen bonding in the aqueous electrochemistry of quinones. *Journal of the American Chemical Society* **2007,** *129*, (42), 12847-12856.

152. Ollinger, K.; Brunmark, A., Effect of hydroxy substituent position on 1,4-naphthoquinone toxicity to rat hepatocytes. *Journal of Biological Chemistry* **1991,** *266*, (32), 21496-21503.

153. Murillo-Gelvez, J.; Hickey, K. P.; Di Toro, D. M.; Allen, H. E.; Carbonaro, R. F.; Chiu, P. C., Experimental validation of hydrogen atom transfer Gibbs free energy as a predictor of nitroaromatic reduction rate constants. *Environmental Science & Technology* **2019,** *53*, (10), 5816-5827.

154. Selwyn, L.; Tse, S., The chemistry of sodium dithionite and its use in conservation. *Studies in Conservation* **2008,** *53(sup2)*, 61-73.

155. Falandysz, J.; Chudziński, K.; Kojta, A. K.; Jarzyńska, G.; Drewnowska, M., Comparison of two acid extraction methods for determination of minerals in soils beneath to Larch Bolete (*Suillus grevillei*) and aimed to estimate minerals sequestration potential in fruiting bodies. *Journal of Environmental Science and Health. Part A, Toxic/Hazardous Substances & Environmental Engineering* **2012,** *47*, (11), 1607-1613.

156. Dondi, D.; Zeffiro, A.; Speltini, A.; Tomasi, C.; Vadivel, D.; Buttafava, A., The role of inorganic sulfur compounds in the pyrolysis of Kraft lignin. *Journal of Analytical and Applied Pyrolysis* **2014,** *107*, 53-58.

157. Evdokimov, A. N.; Kurzin, A. V.; Fedorova, O. V.; Lukanin, P. V.; Kazakov, V. G.; Trifonova, A. D., Desulfurization of kraft lignin. *Wood Science and Technology : Journal of the International Academy of Wood Science* **2018,** *52*, (4), 1165-1174.

158. Shen, D. K.; Gu, S., The mechanism for thermal decomposition of cellulose and its main products. *Bioresource Technology* **2009,** *100*, (24), 6496-6504.

159. Gran, G., Determination of the equivalence point in potentiometric titrations. Part II. *Analyst* **1952,** *77*, (920), 661-671.

Appendix A

SUPPORTING INFORMATION

A.1   Thermodynamics of Ag$^+$ and Hydroquinones and Their Redox Reaction
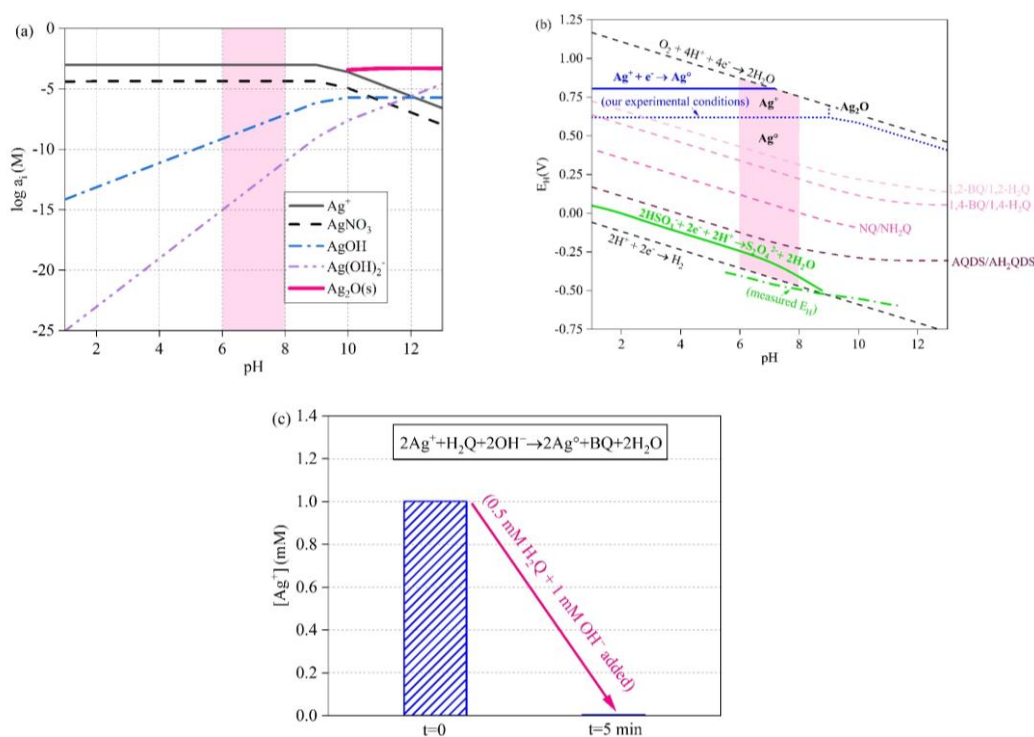
Figure A.1   Thermodynamics of Ag$^+$ and hydroquinones and their redox reaction

Figure A.1(a) is the Ag$^+$ speciation diagram, where [AgNO$_3$] = 1 mM in 0.1 M NaNO$_3$, and a$_i$ is the activity of ionic species or the amount of Ag$_2$O$_{(s)}$ in M.
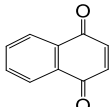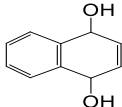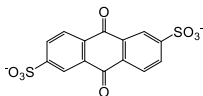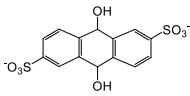
Calculations were performed using Visual MINTEQ 3.1. Ag^+ was the predominant species at pH 6–8, and precipitation would occur at pH ≥ 9 under our experimental conditions. Figure A.1(b) is the pH-E_h diagram of Ag^+/Ag^0, sulfite/dithionite, and four quinone/hydroquinone redox couples obtained using the Nernst equation. The midpoint potentials, at which the total concentrations of the fully oxidized and reduced species are equal, were calculated for the quinone/hydroquinone pairs using Equation A.1 and for sulfite/dithionite using Equation A.2, and were shown as a function of pH. The blue dotted line represents the calculated reduction potential of Ag^+/Ag^0 under our experimental conditions, and the green dashed line represents the measured reduction potential (vs. SHE) of the dithionite solution used. The pH range studied (6–8) is shaded in pink. The names and structures of the chemicals are listed in Table A.1. It is clear that the reduction of the quinones by dithionite and oxidation of the hydroquinones by Ag^+ are both thermodynamically favorable under our experimental conditions.

$$E_h^{'} = E_h^0 + 2.303 \frac{RT}{2F} \log([H^+]^2 + K_{a1RED}[H^+] + K_{a1RED}K_{a2RED}) \tag{A.1}$$

$$E_h^{'} = E_h^0 + 2.303 \frac{RT}{2F} \log \left(\frac{([H^+]^2 + K_{a1RED}[H^+] + K_{a1RED}K_{a2RED})[H^+]^4}{([H^+]^2 + K_{a1OX}[H^+] + K_{a1OX}K_{a2OX})^2} \right) \tag{A.2}$$

Figure A.1(c) is the result of Ag^+ reduction with 1,4-hydroquinones (H_2Q) at pH = 7.0±0.3. When stoichiometric amounts of H_2Q (H_2Q/Ag^+ = 1:2) and NaOH (OH^-/Ag^+ = 1:1) were added to 50 mL of 1 mM Ag^+ in 0.1 M $NaNO_3$, instant changes in solution color and in Ag^+ concentration were observed. Due to the rapid and continuous decrease in Ag^+ concentration, the first stable Ag^+ concentration reading was obtained at 5 min, after aqueous Ag^+ had been largely depleted. The result suggests that Ag^+ reduction by H_2Q, and likely by other hydroquinones, is fast at circumneutral pH.

Table A.1　Names, structures, standard or midpoint reduction potentials vs. SHE at 25 °C, and pK$_a$ values of Ag$^+$/Ag^0, quinone/hydroquinone, and sulfite/dithionite redox pairs.

Oxidized Form[a]	Reduced Form[a]	E$_h$° (V)	E$_h$°'[b] (V)	pK$_{a1OX}$	pK$_{a2OX}$	pK$_{a1RED}$	pK$_{a2RED}$
Ag$^+$	Ag$^0_{(s)}$	0.80 [149]	0.80	–	–	–	–
1,2-benzoquinone (1,2-BQ)	1,2-hydroquinone (1,2-H$_2$Q)	0.78	0.37 [34]	–	–	9.14 [150]	13.08 [150]
1,4-benzoquinone (1,4-BQ)	1,4-hydroquinone (1,4-H$_2$Q)	0.69	0.28 [34]	–	–	9.85 [151]	11.84 [151]
1,4-naphthoquinone (NQ)	1,4-dihydroxynapht halene (NH$_2$Q)	0.47	0.06 [34]	–	–	9.3 [152]	N.A.
9,10-anthraquinone-2,6-disulfonate (AQDS)	9,10-anthrahydroquin one-2,6-disulfonate (AH$_2$QDS)	0.23 [153]	–0.18 [34, 153]	–	–	7.6 [153]	10.5 [35, 153]
HSO$_3^-$	S$_2$O$_4^{2-}$	0.09[c]	–0.32	1.76 [154]	7.19 [154]	0.34 [154]	2.46 [154]

N.A. = not available. [a]Formula and structures shown are predominant species at pH 7; [b] E$_h$°' is the E$_h$° at pH 7; [c]Calculated from the midpoint redox potential of sulfite/dithionite pair at pH 14.

A.2　Iron Contents of Samples Containing Lignin

Given an ash content of 11.5% in the commercial lignin (Table A.2), inorganic elements such as redox-active metals may be present in samples containing lignin and

thus contribute to the observed electron accepting capacity (EAC) and/or electron donating capacity (EDC). To identify redox-active elements in those samples, elements from oxygen (O) through uranium (U) were scanned using a wavelength dispersive X-ray fluorescence spectrometry (WDXRF, Rigaku Supermini 200, Tokyo, Japan). Analyses using WDXRF identified the presence of two redox-active elements, iron and sulfur, in lignin.

Table A.2   Proximate analysis of feedstocks

	Volatile Matter (%)	Fixed Carbon (%)	Ash (%)
Cellulose	97.8 ± 0.1	2.2 ± 0.1	BD
Xylan	88.1 ± 0.4	11.9 ± 0.4	BD
Lignin	48.7 ± 1.5	39.9 ± 0.0	11.5 ± 1.5
Wood	88.5 ± 0.2	11.5 ± 0.2	BD

BD: below detection. Errors show the range of values from duplicates.

Iron contents of samples containing lignin (listed in Table A.3) were further quantified by extraction with 1:1 HNO_3 (~35%). [155] Specifically, 0.05 g of sample was shaken in 5 mL of HNO_3 (1:100 w/v) at 100 rpm for 72 h, and then diluted in a 25-mL volumetric flask with deionized water. The diluted sample extracts were filtered with PVDF syringe filters prior to analysis using an inductively coupled plasma-mass spectrometry (ICP-MS). Results from ICP-MS following acid-digestion confirmed that the iron contents of lignin and biopolymer mixture were less than 0.03 mmol/g, showing the contribution of iron to the electron storage capacity (ESC) of samples containing lignin was negligible.

Table A.3   Acid-extractable iron (mmol/g) in samples containing lignin

L	0.0173 ± 0.0014	M	0.0113 ± 0.005
L350	0.0119 ± 0.007	M350	0.0049 ± 0.0010
L450	0.0285 ± 0.011	M450	0.0076 ± 0.0007
L550	0.0167 ± 0.0011	M550	0.0073 ± 0.004
L650	0.0209 ± 0.002	M650	0.0061 ± 0.0016

Errors show the range of values from duplicates.

We also prepared a Na^+-exchanged lignin sample to eliminate the effect of redox-active metal cations on ESC. Specifically, 1 g of Amberlite (Alfa Aesar, Haverhill, MA) was added to a solution containing 0.05 g of lignin, 24 h prior to the experiment, and the solution was filtered with a cation exchange cartridge (Waters, Milford, MA) right before mediated electrochemical analyses (MEA). MEA results confirmed that the ESC (EDC and EAC) of Na^+-exchanged lignin were the same as untreated lignin.

A.3   Characterization Results

A.3.1   Sulfur contents of samples containing lignin

Ultimate analysis showed that the commercial lignin contained 3.36% (1.05 mmol/g) sulfur (Table A.4), which was presumably incorporated through pulping (with Na_2S) and acid precipitation (with H_2SO_4) during lignin extraction. Sulfate can make up about 45% of sulfur in lignin [156] but would not contribute to EDC or EAC. Other inorganic (e.g., elemental sulfur and (poly)sulfides) and organic (e.g., sulfides) sulfur species, if present [157] and reactive toward the oxidized form of ABTS (i.e., the radical $ABTS^{\cdot +}$), could have contributed to the observed EDC of lignin.

Table A.4   Sulfur content (mmol/g) in biochar samples containing lignin

L	1.05 ± 0.01	M	0.33 ± 0.02
L350	0.76 ± 0.03	M350	0.31 ± 0.00
L450	0.60 ± 0.01	M450	0.29 ± 0.01
L550	0.67 ± 0.02	M550	0.27 ± 0.01
L650	0.68 ± 0.01	M650	0.29 ± 0.02

Errors show the range of values from duplicates. Sulfur contents were calculated based on the results from the ultimate analysis.

A.3.2 Results on ultimate analysis
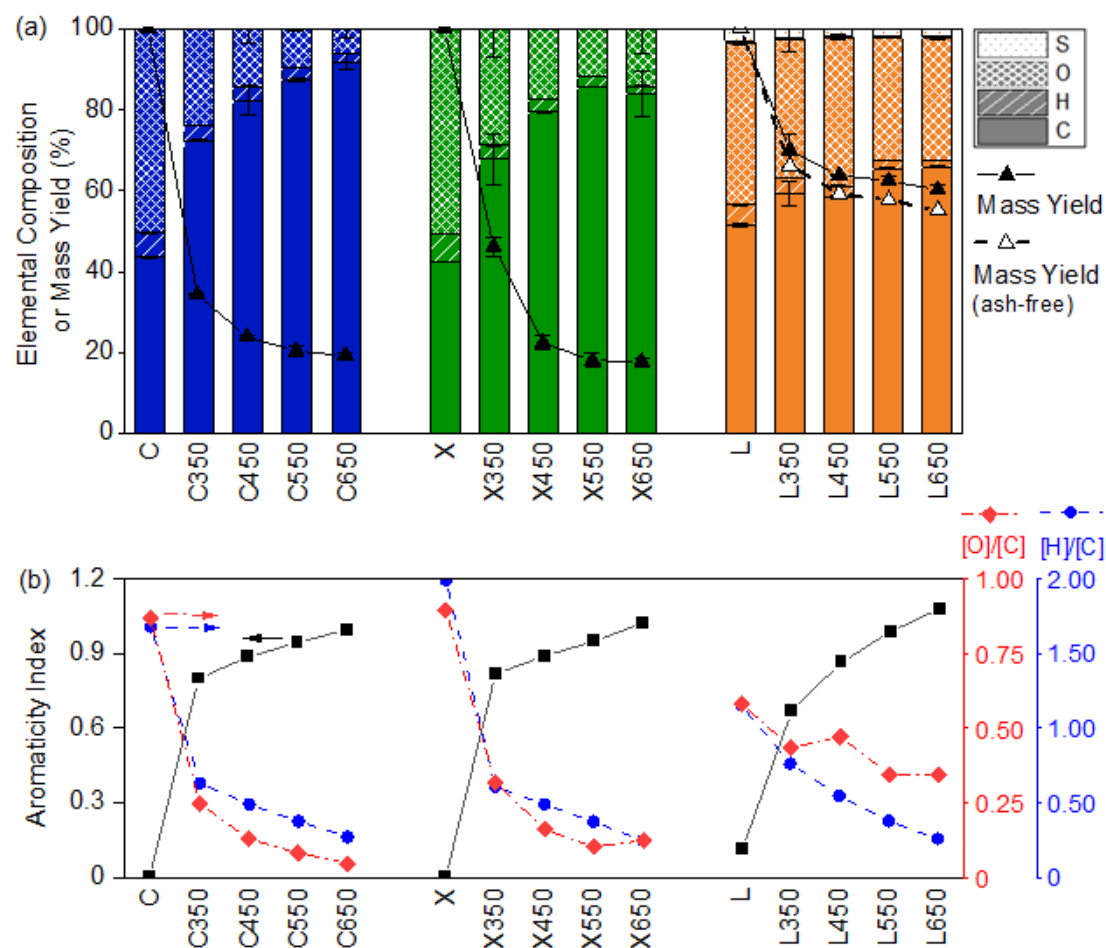
Figure A.2   Characterization of three biopolymers and corresponding biochars from individual biopolymer pyrolysis. (a) Elemental composition (stacked columns) and mass-based yield. Open diamonds represent the yields on an ash-free mass basis. (b) Aromaticity index and mole ratios of O/C and H/C. Error bars represent the range of results from duplicates.
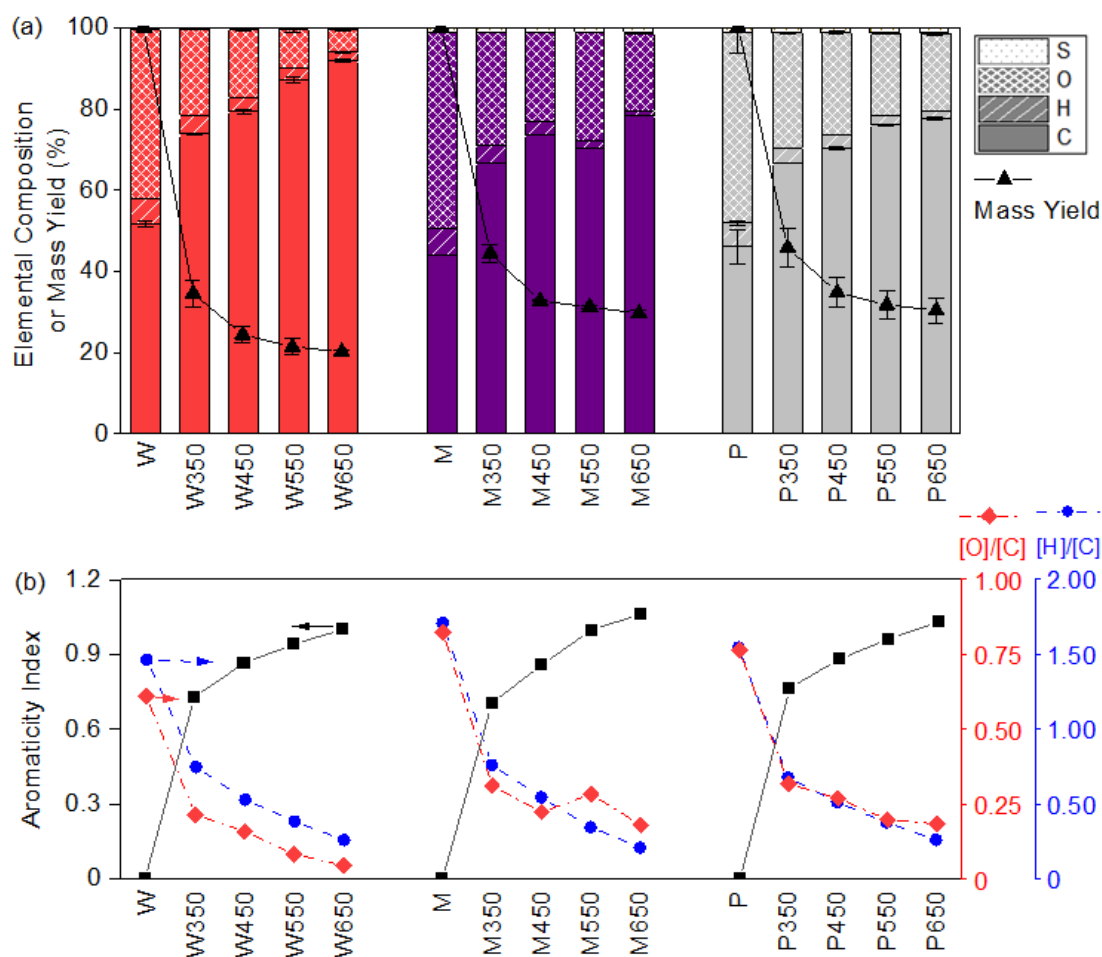
Figure A.3   Characterization of wood, biopolymer mixture, and corresponding
             biochars from wood or biopolymer mixture pyrolysis. (a) Elemental
             composition (stacked columns) and mass-based yield. (b) Aromaticity
             index and mole ratios of O/C and H/C. P stands for "predicted", showing
             values calculated based on the yield and characterization results of
             biochars made from individual biopolymers (Figure A.2). Error bars
             represent the range of results from duplicates.

A.3.3   Temperature dependency of ESC

The ESC of biochar has been attributed to (hydro)quinone groups, the creation

of which is favorable at medium pyrolysis temperatures (around 500 °C), as suggested

by K-edge near-edge X-ray absorption fine structure (NEXAFS) spectra. [5, 14] Interestingly, the temperature dependency of ESC was different for different biopolymers. While xylan biochars exhibited the highest ESC at 550 °C, the temperature dependencies of cellulose and lignin biochars are less clear. Cellulose is a linear polysaccharide that decomposes in a narrow temperature range (325–450 °C) under nitrogen, [158] whereas xylan and lignin are a branched polysaccharide and three-dimensional cross-linked phenylpropane units, respectively, that exhibit a wider decomposition temperature range of 200–500 °C [101]. As pyrolysis temperature increases, hemicellulose generally decomposes first, followed by cellulose, and then lignin, which decomposes over a wide temperature range. [101, 102] These biopolymers may undergo dehydration, bond-cleavage, vaporization and condensation, cracking, cross-linkage, repolymerization and/or rearrangement, all of which might take place at different temperatures for different biopolymers and affect the molecular mechanism for ESC creation. The temperature dependency of wood was similar to those of cellulose and lignin. This similarity is due to the fact that cellulose and lignin exhibited a similar temperature dependence when pyrolyzed separately and together comprised more than 85% of the wood (Figure A.4).
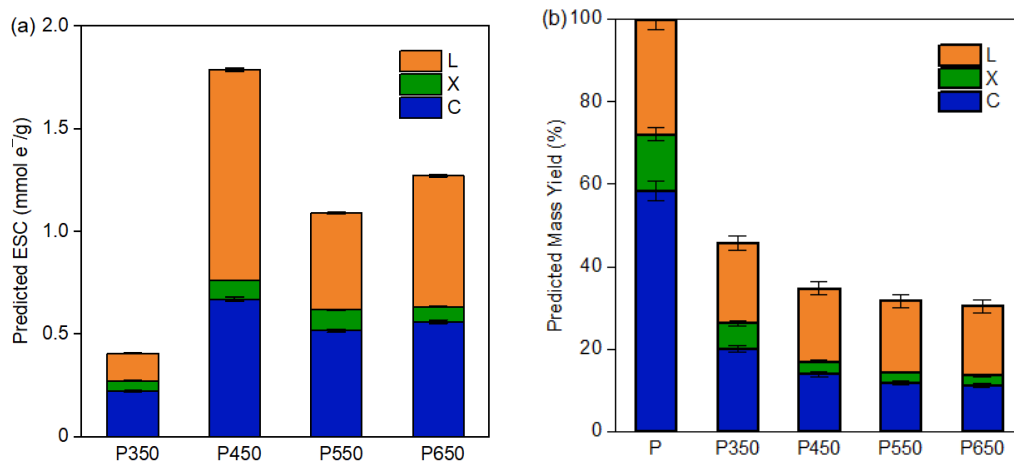
Figure A.4   The contribution of each biopolymer to predicted (a) first cycle ESC and (b) mass yields. Note that panels (a) and (b) are calculated based on Equation 4.3 and Equation 4.5, equivalent to the third group (i.e., bars in gray) in Figure 4.6(a) and Figure A.3(a), respectively. Error bars represent the range of results from duplicates.

A.4   Characterization of Soil Reef and Rogue Biochars

The properties of the biochar that are being measured include elemental composition (CHNS), ash content, pH, BET surface area, cation exchange capacity (CEC), and ESC. Prior to characterization, each biochar was sifted to obtain a size fraction of 250–500 µm and washed with deionized water, dried at 65 °C for 24 h, and stored in a desiccator.

Carbon, hydrogen, nitrogen, sulfur contents were determined using a vario MACRO cube (Elementar, Langenselbold, Germany). Fully dried samples (5-20 mg) were combusted at ca. 960 °C in ultra-high-purity oxygen, and passed through copper oxide pellets and then electrolytic copper with helium as carrier gas. The gases were quantified by a thermal conductivity detector (TCD). The oxygen content was

estimated by subtracting carbon, hydrogen, nitrogen, sulfur, and ash contents from 100%. Ash contents were measured by combusting a biochar sample (5-10 mg) in the air at 900 °C for 5 min using a Discovery thermogravimetric analyzer (TA Instruments, New Castle, DE). Ash contents were taken to be the mass remaining after the combustion.

For pH measurement, 0.5 g of biochar was placed in 10 mL of deionized water (1:20 w/v) and equilibrated for 24 h. Solution pH was measured using an Oakton 11 series pH/mV/°C meter and an Oakton pH electrode (Vernon Hills, IL), calibrated against pH 4, 7, and 10 standards. The specific surface area was measured using a Micromeritics BET surface area analyzer (Norcross, GA) through N_2 adsorption to a biochar sample of known mass at 77.382 K. CEC was measured by NH_4^+ saturation using EPA Method 9080. NH_4^+ concentration was determined using a Metrohm 850 Professional IC AnCat unit equipped with a conductivity detector (Herisau, Switzerland). ESC was measured earlier in Chapter 2 through chemical redox titration [59] using dissolved O_2 (DO, +0.80 V vs. SHE at pH 7, $P_{O_2} = 0.21$ atm) and Ti(III) citrate (–0.36 V vs. SHE at pH 6.4) as oxidant and reductant, respectively. In addition, part of the electrons stored in dithionite-reduced biochar was retrieved using 10 mM ferricyanide in 20 mM phosphate buffer according to the method published in our previous study [59].

Table A.5   Physical-chemical properties of biochar

		SRB	Rogue
Vendor		The Biochar Company (PA)[a]	Oregon Biochar Solutions
Source Material		Southern Yellow Pine	Douglas Fir + Ponderosa Pine
Pyrolysis Temperature (°C)		550	900 (fast pyrolysis)
Elemental composition (%)	C	72.01±5	68.47±10
	H	1.96±0.02	1.50±0.2
	N	0.36±0.08	0.28±0.07
	S	0.26±0.03	0.24±0.15
	O	20.82±5	16.99±10
Ash (%)		4.59±1.3	12.52±0.5
pH (S. U.)		7.53±0.05	8.88±0.08
BET (m^2/g)		158.39±3	407.22±9
CEC (mmol/g)		0.42±0.02	0.12±0.03
ESC measured with Ti(III) citrate and DO (mmol/g)[b]		3.54±0.13 (2.43±0.0)[b]	7.07±0.15 (6.78±0.2)[b]

Errors represent the range of results from duplicates.
[a] The company has discontinued production.
[b] Values in parentheses represent the reversible ESC.

A.5   The pK$_a$ of ATO

0.8 g/L of SRB$_{RED}$ was added to reactors containing 3-amino-1,2,4-triazol-5-one (ATO) to determine the sorption of ATO to SRB$_{RED}$ at different pH. As shown in Figure A.5, the amount of ATO sorbed to SRB$_{RED}$ at the end of the experiment was 11.80±4.79 and 17.45±1.55 µmol/g at pH 6 and 8, respectively. In contrast, the sorption of ATO to SRB$_{RED}$ was negligible at pH 10.
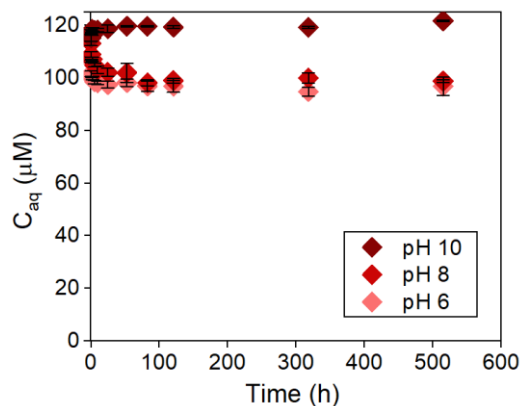
Figure A.5   Sorption of ATO to 0.8 g/L of SRB$_{RED}$ at pH 6, pH 8, and pH 10.

Since an experimentally determined pK$_a$ was not available for ATO in literature, we performed an acid-base titration using NaOH. As 10 mM NaOH solution was added drop by drop to 25 mL of 10 mM ATO (in 100 mM KCl), the volume of NaOH added and pH were recorded. This process can be treated as a weak acid (i.e., ATO) titration by a strong base (i.e., NaOH), in which the Gran method can be applied to obtain the K$_a$ (and pK$_a$) of ATO. Based on the Gran plot shown in Figure A.6, the K$_a$ of $1.95\times10^{-9}\pm6.53\times10^{-11}$ was obtained through linear regression of data before the equivalence point, which corresponds to the pK$_a$ of 8.71±0.02.
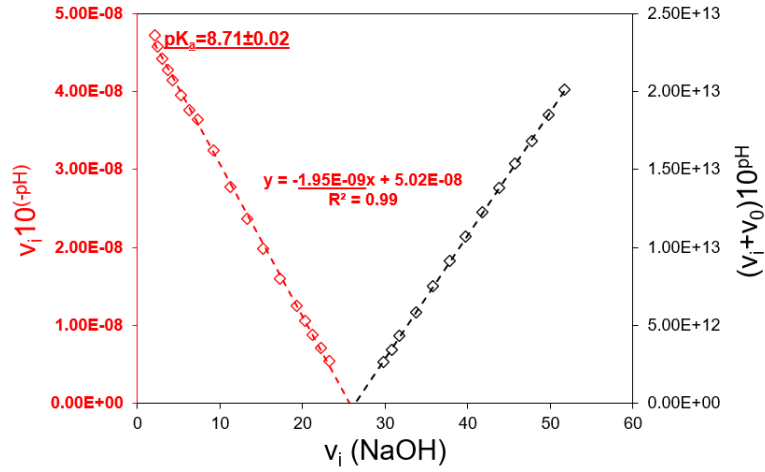
Figure A.6 Gran plots using data from ATO titration with NaOH. The X-axis is the total volume of NaOH (v_i) added to the ATO solution up to the ith point. The left-Y and right-Y axes are calculated values of $v_i 10^{(-pH)}$ and $(v_i+v_0)10^{pH}$, respectively, where v_0 is the initial ATO volume. Titration data before and after the equivalence point are plotted in red diamonds on the left-Y axis and in black diamonds on the right-Y axis, respectively.

Below is a description of the Gran method [159]:

At any point:

$$K_a = \frac{[H^+]_i[ATO^-]_i}{[HATO]_i} \qquad \text{(Equation A.3)}$$

where protonated and deprotonated forms of ATO were denoted as HATO and ATO⁻, respectively.

Before the equivalence point, approximations below can be made:

$$[HATO]_i \approx \frac{v_0[HATO]_0 - v_i[OH^-]_0}{v_0+v_i} \qquad \text{(Equation A.4)}$$

$$[ATO^-]_i \approx \frac{v_i[OH^-]_0}{v_0+v_i} \qquad \text{(Equation A.5)}$$

Where v_0 and v_i denote the initial ATO volume (25 mL) and the total volume of NaOH added up to the ith point, respectively; $[HATO]_0$ is the initial concentration of ATO (10 mM) and $[OH^-]_0$ is the concentration of titrant (10 mM).

Substitute $[HATO]_i$ and $[ATO^-]_i$ in Equation A.3 with Equations A.4 and A.5, respectively:

$$K_a \approx \frac{[H^+]_i v_i [OH^-]_0}{v_0 [HATO]_0 - v_i [OH^-]_0} \qquad \text{(Equation A.6)}$$

To further simplify:

$$[H^+]_i v_i = 10^{-pH_i} v_i \approx -K_a \left(v_i - v_0 \frac{[HATO]_0}{[OH^-]_0} \right) \qquad \text{(Equation A.7)}$$

Therefore, before the equivalence point, when $10^{-pH_i} v_i$ is plotted against v_i, the slope is $-K_a$, and the equivalence point (the intercept of X-axis) is $v_0 \frac{[HATO]_0}{[OH^-]_0}$.

At any point:

$$[OH^-]_i \approx \frac{v_i [OH^-]_0 - v_0 [HATO]_0}{v_0 + v_i} \qquad \text{(Equation A.8)}$$

To further simplify:

$$\frac{[OH^-]_i (v_0 + v_i)}{K_w} = 10^{pH_i}(v_0 + v_i) \approx \frac{[OH^-]_0}{K_w} \left(v_i - v_0 \frac{[HATO]_0}{[OH^-]_0} \right) \qquad \text{(Equation A.9)}$$

After the equivalence point, when $10^{pH_i}(v_0 + v_i)$ is plotted against v_i, the equivalence point is $v_0 \frac{[HATO]_0}{[OH^-]_0}$, meaning the two curves should cross the X-axis at the same point.

A.6   Mass Balance of Munitions Constituents in Batch Reactor Experiments

Table A.6   Mass balance of 3-nitro-1,2,4-triazol-5-one (NTO) reduction by biochar in buffered solutions

Figure 5.1(a): pH 6 in 50 mM MES buffer				
	SRB_{OX}		SRB_{RED}	
Biochar mass	0.8 g/L		0.8 g/L	
(µmol/g)	AVE	STD	AVE	STD
NTO_{total}	138	0.07	138	0.07
NTO_{aq}	114	1.6	26.0	8
ATO_{aq}	–	–	85.6	5
NTO_s	16.2	2	0.0	0
ATO_s	–	–	14.0	2
Mass balance (%)	94±3%		91±10%	
NTO_{total}−NTO_{aq} (µmol/g)	24.0±0.07		112±8	
ATO_{total} (µmol/g)	–		99.6±7	

Figure 5.1(b): pH 8 in 50 mM Tris buffer				
	SRB_{OX}		SRB_{RED}	
Biochar mass	0.8 g/L		0.8 g/L	
(µmol/g)	AVE	STD	AVE	STD
NTO_{total}	134	0.07	134	0.07
NTO_{aq}	124	0.2	39.5	7
ATO_{aq}	–	–	68.0	6
NTO_s	10.6	0	0.0	0
ATO_s	–	–	13.6	2
Mass balance (%)	101±0%		91±12%	
NTO_{total}−NTO_{aq} (µmol/g)	9.51±0.3		94.0±7	
ATO_{total} (µmol/g)			81.6±8	

Figure 5.1(c) and Figure 5.2(a): pH 10 in 50 mM CAPSO buffer								
	SRB_{OX}				SRB_{RED}			
Biochar mass	0.8 g/L		0.4 g/L		0.8 g/L		0.4 g/L	
(µmol/g)	AVE	STD	AVE	STD	AVE	STD	AVE	STD
NTO_{total}	129	0.4	258	0.9	129	0.4	258	0.9
NTO_{aq}	127	0.15	255	0.6	45.3	8	172	12
ATO_{aq}	–	–	–	–	83.9	4	86.5	12
NTO_s	–	–	–	–	–	–	–	–
ATO_s	–	–	–	–	–	–	–	–
Mass balance (%)	98±0%		99±0%		100±9%		101±10%	
NTO_{total}−NTO_{aq} (µmol/g)	2.14±0.3		2.74±0.4		83.5±8		85.2±13	
ATO_{total} (µmol/g)					83.9±4		86.5±12	

Table A.7   Mass balance of MC reduction by biochar in ASR at pH 6

	Figures 5.9(a) and (b)	SRB_{OX}		SRB_{RED}	
	(μmol/g)	AVE	STD	AVE	STD
	NTO_{total}	135	2	135	2
	NTO_{aq}	120	0.8	31.7	7
	ATO_{aq}	−	−	77.0	5
	NTO_s	15.8	0.5	1.20	0.6
	ATO_s	−	−	14.5	5
	Mass balance (%)	100±1%		94±4%	
	$NTO_{total}-NTO_{aq}$ (μmol/g)	15.6±2		104±8	
NTO	ATO_{total} (μmol/g)	−		91.6±6	
	Figures 5.9(a) and (b)	$Rogue_{OX}$		$Rogue_{RED}$	
	(μmol/g)	AVE	STD	AVE	STD
	NTO_{total}	138	0.4	138	0.4
	NTO_{aq}	93.7	5	26.1	1.6
	ATO_{aq}	−	−	73.3	1.2
	NTO_s	28.7	2	2.10	0.2
	ATO_s	−	−	21.0	1.2
	Mass balance (%)	88±5%		89±3%	
	$NTO_{total}-NTO_{aq}$ (μmol/g)	44.7±6		112±2	
	ATO_{total} (μmol/g)	−		94.3±2	
	Figures 5.9(c) and (d)	$Rogue_{OX}$		$Rogue_{RED}$	
	(μmol/g)	AVE	STD	AVE	STD
	$DNAN_{total}$	911	5	911	5
	$DNAN_{aq}$	397	11	281	30
	$2ANAN_{aq}$	−	−	24.3	3
DNAN	$4ANAN_{aq}$	−	−	1.30	0
	$DNAN_s$	444	14	454	30
	$2ANAN_s$	−	−	42.0	11
	$4ANAN_s$	−	−	0.600	0.8
	Mass balance (%)	92±3%		88±9%	
	$DNAN_{total}-DNAN_{aq}$ (μmol/g)	518±5		634±20	
	$2ANAN_{total}+4ANAN_{total}$ (μmol/g)	−		68.1±7	
	Figures 5.9(e) and (f)	$Rogue_{OX}$		$Rogue_{RED}$	
	(μmol/g)	AVE	STD	AVE	STD
	RDX_{total}	452	20	434	20
	RDX_{aq}	220	1.5	102	6
	RDX_s	212	11	162	11
RDX and HMX	Mass balance (%)	92±3%		61±4%	
	$RDX_{total}-RDX_{aq}$ (μmol/g)	232±20		332±19	
	Figures A.7(a) and (b)	$Rogue_{OX}$		$Rogue_{RED}$	
	(μmol/g)	AVE	STD	AVE	STD
	HMX_{total}	13.3	0.7	12.8	0.8
	HMX_{aq}	2.40	0.03	1.20	0.11
	HMX_s	10.8	0.4	10.4	0.8
	Mass balance (%)	99±2%		90±1%	
	$HMX_{total}-HMX_{aq}$ (μmol/g)	11.0±0.7		11.6±0.7	

Nitroguanidine (NQ), 2,4-dinitroanisole (DNAN), hexahydro-1,3,5-trinitro-1,3,5-triazinane (RDX), octahydro-1,3,5,7-tetranitro-1,3,5,7-tetrazocine (HMX), 2-amino-4-nitroanisole (2-ANAN), and 4-amino-2-nitroanisole (4-ANAN)
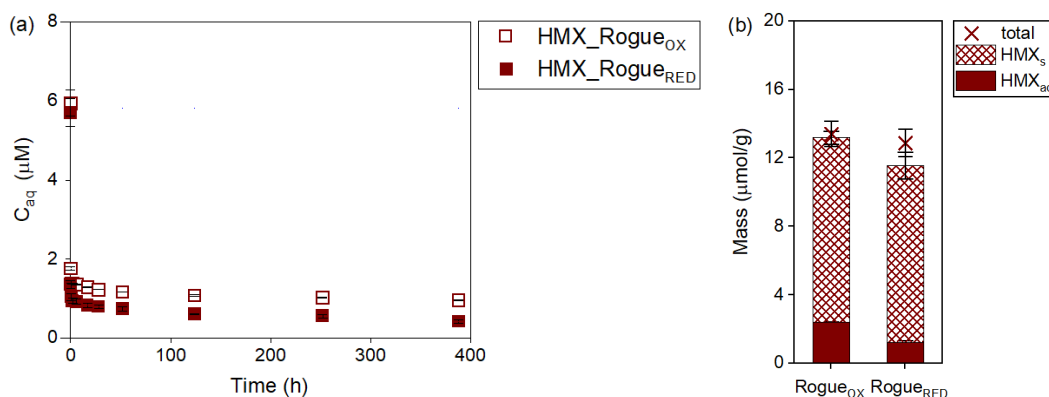
Figure A.7   (a) Aqueous concentration (C_{aq}) of HMX over time with 0.44 g/L of Rogue biochar in the presence of RDX in artificial stormwater runoff (ASR) at pH6. (d) HMX mass balance. "total" is the total mass of HMX added at the beginning of the experiment. HMX_{aq} and HMX_s are the masses in the aqueous phase at the end of the experiment (ca. 400 h) and the extracted mass from the solid phase, respectively.

A.7   NQ Sorption to Biochar

Parallel sorption experiments for NQ were first conducted inside and outside of the glovebox. The results in Figure A.8(a) confirmed that the sorption of NQ is not influenced by the atmosphere. Thus, all other sorption experiments were conducted outside of an anaerobic glovebox. As NQ is a neutral compound under circumneutral pH conditions, a similar amount of NQ was removed at pH 6 and 8 (Figure A.8(b)). We chose pH 8 to further assess the sorption of NQ to SRB for obtaining its Langmuir isotherm (Figure A.9).
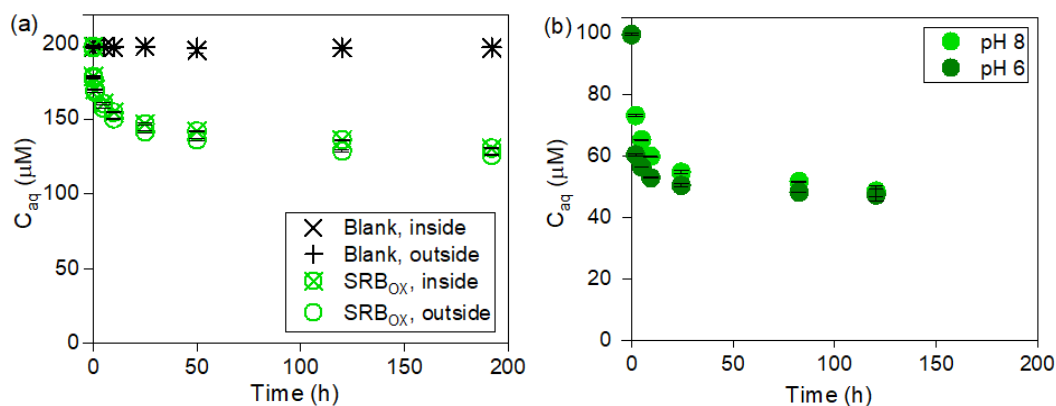
Figure A.8   (a) Sorption of NQ to 0.80 g/L of SRB$_{OX}$ inside vs. outside of the glovebox in 50 mM Tris buffer at pH 8. (b) Sorption of NQ to 1.33 g/L of SRB$_{RED}$ at pH 6 (50 mM MES buffer) vs. pH 8 (50 mM Tris buffer) in the glovebox.
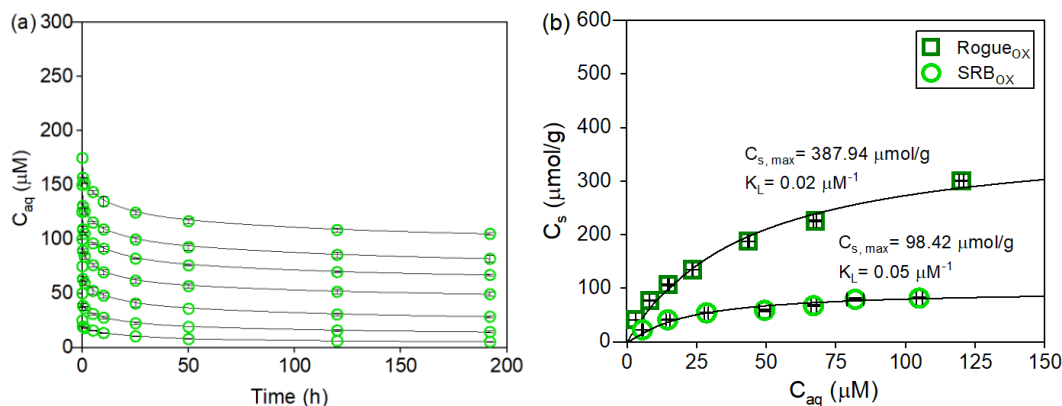
Figure A.9   (a) Sorption of NQ to 0.80 g/L of SRB$_{OX}$ at pH 8. (b) Comparison of NQ sorption to 0.80 g/L SRB$_{OX}$ in 50 mM Tris buffer at pH 8 and to 0.44 g/L of Rogue$_{OX}$ in ASR at pH 6, and their fitted Langmuir isotherms. The regression R^2 of the measured and predicted sorption capacities of SRB$_{OX}$ and of Rogue$_{OX}$ for NQ based on the fitted Langmuir isotherms were 0.98 and 0.96, respectively.

165
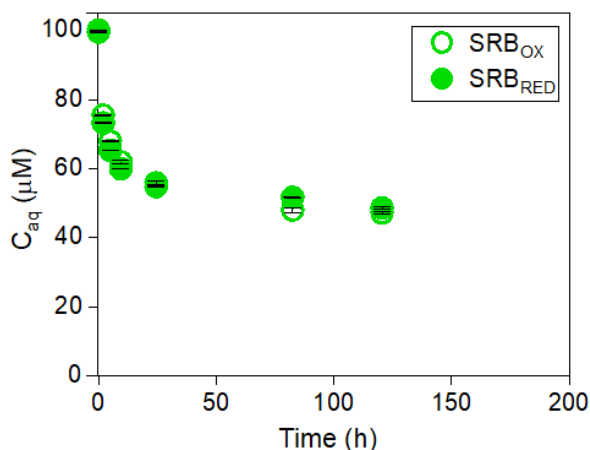
Figure A.10 Aqueous concentration (C_{aq}) of NQ over time with 1.33 g/L of SRB_{OX} or SRB_{RED} at pH 8.

A.8 NO_2^- Production from the Abiotic Transformation of RDX by $Rogue_{RED}$

To verify the production of NO_2^- from the abiotic reduction of RDX by $Rogue_{RED}$, batch reactors containing 1 g of either $Rogue_{OX}$ or $Rogue_{RED}$ were prepared in duplicates. Each reactor contained 0.2 L of ca. 140 µM RDX (corresponding to 28 µmol of RDX). Solutions were buffered with 25 mM HEPES at pH 7 instead of ASR because the Cl^- in ASR interfered with ion chromatographic (IC) detection of NO_2^-. Due to the low solubility of RDX (270 µM), four additional aliquots of RDX stock solution (6 mL per aliquot, each containing 9.32 µmol RDX) were added to the reactor at later times. NO_2^- was measured using a Metrohm 850 Professional IC.

As shown in Figure A.10, in contrast to reactors containing $Rogue_{OX}$ where no NO_2^- was detected, about 5.5 µmol of NO_2^- was produced within 1 h. As more RDX was added in four additional doses, 6 and 7 µmol of NO_2^- were formed after the first and second doses, respectively, while further NO_2^- formation was minimal following

166

the third and fourth doses. The total amount of NO_2^- produced per gram of $Rogue_{RED}$ was 22 µmol, clearly indicating the ESC of Rogue biochar was accessible to and reactive toward RDX.
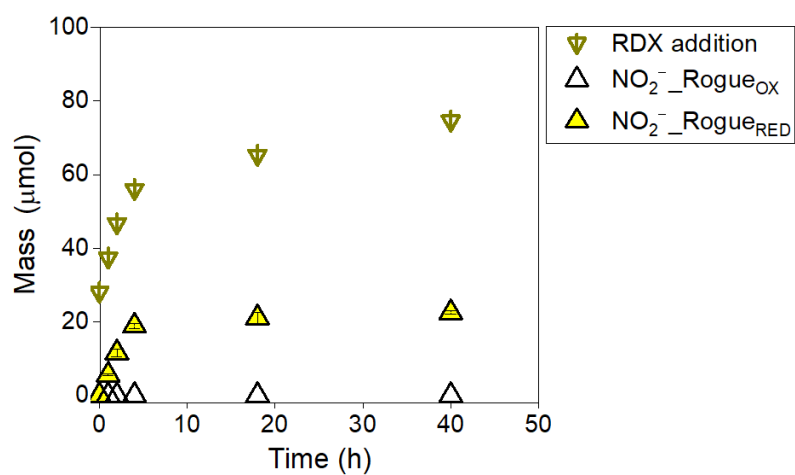
Figure A.11 NO_2^- formation upon RDX addition to reactors containing 5 g/L of Rogue biochar

Appendix B

PRINTED DATA FOR GENERATING THE FIGURES

Table B.1   Data for generating Figure 2.5 (a)

| Time(h) | Electrons transferred (mmol) | | | | | | | | | |
| | 0.94 g | | 0.66 g | | 0.47 g | | 0.28 g | | control | |
	AVE	STD	AVE	STD	AVE	STD	AVE	STD	AVE	STD
1	1.38	0.10	1.54	0.06	1.20	0.02	0.46	0.05	0.01	0.13
2	1.74	0.10	1.68	0.10	1.20	0.10	0.59	0.06	0.04	0.15
8			2.17	0.09	1.69	0.04	0.75	0.08	0.01	0.07
16	2.72	0.27	2.61	0.08	2.02	0.04	1.04	0.08	0.02	0.00
24	2.89	0.18	2.63	0.09	2.04	0.01	0.97	0.05	0.02	0.10
36	3.13	0.30							0.05	0.08
48	3.52	0.23							0.05	0.11
72	3.56	0.26							0.04	0.08

Table B.2   Data for generating Figure 2.7 (a)

Time(h)	Electrons transferred (mmol) based on absorbances							
	0.69 g		0.49 g		0.29 g		control	
	AVE	STD	AVE	STD	AVE	STD	AVE	STD
0	0.00		0.00	0.00	0.00	0.00	0.00	0.00
1	0.70		0.52	0.03	0.36	0.00	-0.02	0.01
2	0.87		0.74	0.07	0.42	0.01	-0.02	0.01
4	1.02		0.90	0.07	0.47	0.00	-0.01	0.01
6	1.11		1.00	0.00	0.51	0.01	0.00	0.02
10					0.53	0.01	-0.01	0.02
12	1.24		1.02	0.03			-0.02	0.01
18	1.36						0.00	0.05
24	1.38							

Time(h)	Electrons transferred (mmol) based on reduction potentials							
	0.69 g		0.49 g		0.29 g		control	
	AVE	STD	AVE	STD	AVE	STD	AVE	STD
0	0.00		0.00	0.00	0.00	0.00	0.00	0.00
1	0.96		0.56	0.01	0.36	0.03	0.00	0.00
2	0.98		0.78	0.03	0.40	0.00	0.00	0.00
4	1.08		0.91	0.03	0.50	0.00	0.00	0.00
6	1.15		0.99	0.02	0.50	0.00	0.00	0.00
					0.55	0.00	0.00	0.00
12	1.26		1.07	0.03			0.00	0.00
18	1.40						0.00	0.00
24	1.40						0.00	0.00

Table B.3   Data for generating Figure 2.11

| Time (h) | Electrons transferred (mmol) | | | |
| | 0.47 g | | control | |
	AVE	STD	AVE	STD
0	0.00	0.00	0.00	
1	0.66	0.05	-0.13	
2	1.13	0.17	0.00	
3	1.57	0.05	-0.10	
4	1.84	0.12	-0.03	
6	2.24	0.22	0.08	
8	2.37	0.23	0.05	
12	2.43	0.19	0.05	

Table B.4   Data for generating Figure 3.1(a)

	Ag loading (mmol/g)							
Time (h)	Reduced SRB (<100 µm)		Time (h)	Oxidized SRB (<100 µm)		Time (h)	Reduced (SRB 250-500 µm)	
	AVE	STD		AVE	STD		AVE	STD
0.2	0.496	0.000	0.2	0.034	0.006	0.2	0.142	
0.3	0.847	0.058	0.3	0.018	0.009	0.3	0.241	
0.5	1.172	0.183	0.5	0.014	0.008	0.5	0.328	
0.7	1.327	0.065	0.7	0.024	0.013	0.6	0.359	
0.8	1.494	0.083	0.8	0.023	0.011	0.8	0.485	
1.0	1.613	0.064	1.0	0.031	0.025	1.0	0.549	
1.2	1.788	0.012	1.2	0.030	0.027	1.3	0.617	
1.5	2.051	0.003	1.5	0.028	0.019	1.5	0.673	
3	2.011	0.025	2	0.047	0.016	2	0.743	
5	2.070	0.026	3	0.068	0.010	2.5	0.771	
7	2.104	0.028	5	0.070	0.014	6	0.991	
9	2.102	0.025	7	0.099	0.026	11	1.126	
15	2.165	0.024	9	0.085	0.011	21	1.281	
27	2.204	0.021	15	0.099	0.000	29	1.349	
45	2.261	0.090	27	0.127	0.011	45	1.577	
59	2.281	0.065	45	0.246	0.005	66	1.778	
70	2.272	0.073	59	0.268	0.003	118	2.057	
94	2.289	0.065	70	0.265	0.002	148	2.098	
			94	0.267	0.006	173	2.161	
						196	2.226	
						243	2.275	
						346	2.324	

Table B.5 Data for generating Figure 5.1(a)

Time (h)	C_{aq} (µM)									
	NTO_blank		NTO_SRB$_{OX}$		NTO_SRB$_{RED}$		ATO_SRB$_{RED}$		NTO+ATO_SRB$_{RED}$	
	AVE	STD	AVE	STD	AVE	STD	AVE	STD	AVE	STD
0	109.5	0.1	109.5	0.1	109.5	0.1	0.0	0.0	109.5	0.1
0.3	108.9	0.1	105.9	0.2	83.4	2.4	5.8	0.3	89.1	2.2
1	109.8	0.1	104.5	0.2	79.4	2.7	8.8	0.8	88.1	2.0
2	109.6	0.1	103.6	0.1	74.7	2.9	10.8	0.9	85.6	2.0
5	109.4	0.3	101.8	0.4	65.8	2.4	20.2	0.0	86.1	2.4
8	109.2	0.5	100.8	0.1	61.4	3.8	26.7	2.9	88.1	1.1
16.5	109.7	0.2	99.3	0.2	53.6	4.2	35.3	3.1	88.9	1.2
26	111.4	0.4	100.0	0.2	48.6	4.5	43.7	3.4	92.3	1.4
41.5	111.1	0.4	99.1	0.1	43.0	5.0	47.9	3.2	90.9	1.9
65	110.3	0.6	97.1	0.2	35.7	6.4	48.9	3.2	84.6	3.2
89	110.2	0.8	96.4	0.2	33.9	5.5	50.5	2.8	84.4	2.8
190	109.9	0.1	94.0	0.3	26.9	6.0	55.5	2.3	82.4	3.8
383	109.8	0.7	93.6	0.5	17.5	0.6	69.3	1.1	86.8	0.5
524	110.8	0.1	91.0	1.3	18.4	6.2	70.9	3.8	89.3	2.4

Table B.6   Data for generating Figure 5.1(b)

Time (h)	C_{aq} (µM)									
	NTO_blank		NTO_SRB$_{OX}$		NTO_SRB$_{RED}$		ATO_SRB$_{RED}$		NTO+ATO_SRB$_{RED}$	
	AVE	STD	AVE	STD	AVE	STD	AVE	STD	AVE	STD
0	105.3	0.2	105.3	0.2	105.3	0.2	0.0	0.0	105.3	0.2
0.3	106.4	0.1	103.7	0.2	97.1	1.3	7.1	0.9	104.2	0.7
1	106.6	0.1	102.9	0.3	92.8	1.5	11.3	0.4	104.1	1.5
2	107.8	0.4	103.1	0.1	90.5	0.8	14.0	0.8	104.5	0.7
5	107.3	0.3	102.6	0.3	82.6	1.5	19.4	1.2	102.0	0.3
8	108.1	0.3	101.9	0.5	77.3	1.8	23.8	1.7	101.0	1.6
18	107.6	0.6	101.7	0.1	66.9	2.7	31.0	1.9	97.9	1.2
26	107.5	0.2	101.3	0.1	63.2	3.0	34.4	2.3	97.6	1.2
45.5	107.6	0.2	101.4	0.2	56.9	2.8	39.3	2.1	96.2	0.8
72	106.7	0.1	98.6	2.0	51.3	2.5	43.4	2.6	94.7	1.1
120	106.8	0.1	100.0	0.5	46.3	2.7	47.5	1.6	93.8	1.3
288	105.5	2.5	98.5	1.1	37.6	4.2	56.9	2.9	94.5	2.0
429	106.7	0.4	99.4	0.2	32.8	5.3	61.7	4.5	94.5	0.8
597	106.9	0.0	99.1	0.2	29.0	6.1	56.1	5.5	85.1	0.6

Table B.7   Data for generating Figure 5.1(c)

Time (h)	C_{aq} (µM)									
	NTO_blank		NTO_SRB$_{OX}$		NTO_SRB$_{RED}$		ATO_SRB$_{RED}$		NTO+ATO_SRB$_{RED}$	
	AVE	STD	AVE	STD	AVE	STD	AVE	STD	AVE	STD
0	104.0	0.1	104.0	0.1	104.0	0.1	0.0	0.0	104.0	0.1
0.3	104.3	0.2	104.1	0.1	100.8	1.0	2.7	0.3	103.5	0.9
1	104.6	0.2	103.7	0.2	97.4	0.2	6.5	0.7	103.9	0.6
2	104.4	0.4	104.2	0.1	92.7	0.1	12.5	1.0	105.2	1.0
5	104.5	0.2	103.9	0.4	86.7	0.4	19.1	0.5	105.8	0.8
8	104.3	0.2	103.9	0.0	82.4	0.8	24.5	0.9	106.9	0.1
12	104.5	0.0	104.1	0.0	77.4	0.5	30.1	0.7	107.5	0.4
25	104.3	0.2	103.5	0.2	69.3	1.0	38.3	1.9	107.7	1.4
47	103.6	0.1	102.8	0.2	62.7	1.4	44.5	1.8	107.2	0.5
73	103.9	0.0	103.1	0.1	58.6	1.5	48.9	1.7	107.4	0.2
127.5	102.4	0.3	102.4	0.2	52.7	1.7	54.1	2.3	106.8	1.3
265.5	102.1	0.1	101.0	0.2	45.9	2.7	56.1	0.9	101.9	1.8
441	102.3	0.1	101.2	0.1	36.4	5.5	67.3	4.5	103.7	1.7
562	103.0	0.4	101.2	0.2	33.6	6.6	69.6	3.7	103.2	3.0

Table B.8   Data for generating Figure 5.2(a)

	C_{aq} (µM)													
	NTO blank		NTO_SRB$_{OX}$ (0.8 g/L)		NTO_SRB$_{RED}$ (0.8 g/L)		ATO_SRB$_{RED}$ (0.8 g/L)		NTO_SRB$_{OX}$ (0.4 g/L)		NTO_SRB$_{RED}$ (0.4 g/L)		ATO_SRB$_{RED}$ (0.4 g/L)	
Time (h)	AVE	STD	AVE	STD	AVE	STD	AVE	STD	AVE	STD	AVE	STD	AVE	STD
0	104.0	0.1	104.0	0.1	104.0	0.1	0.0	0.0	104.0	0.1	104.0	0.1	0.0	0.0
0.3	104.3	0.2	104.1	0.1	100.8	1.0	2.7	0.3	104.1	0.1	102.2	0.7	1.1	0.1
1	104.6	0.2	103.7	0.2	97.4	0.2	6.5	0.7	103.7	0.2	100.8	0.4	2.5	0.7
2	104.4	0.4	104.2	0.1	92.7	0.1	12.5	1.0	104.2	0.1	98.1	1.1	5.7	1.1
5	104.5	0.2	103.9	0.4	86.7	0.4	19.1	0.5	103.9	0.4	94.7	1.2	10.6	2.1
8	104.3	0.2	103.9	0.0	82.4	0.8	24.5	0.9	103.9	0.0	92.5	1.6	12.6	1.5
12	104.5	0.0	104.1	0.0	77.4	0.5	30.1	0.7	104.1	0.0	90.6	2.1	14.5	2.0
25	104.3	0.2	103.5	0.2	69.3	1.0	38.3	1.9	103.5	0.2	86.4	2.3	19.4	1.9
47	103.6	0.1	102.8	0.2	62.7	1.4	44.5	1.8	102.8	0.2	82.5	2.7	22.3	2.7
73	103.9	0.0	103.1	0.1	58.6	1.5	48.9	1.7	103.1	0.1	80.2	3.0	27.9	2.9
127.5	102.4	0.3	102.4	0.2	52.7	1.7	54.1	2.3	102.4	0.2	76.1	3.6	27.6	3.2
265.5	102.1	0.1	101.0	0.2	45.9	2.7	56.1	0.9	101.0	0.2	68.2	6.1	29.5	4.6
441	102.3	0.1	101.2	0.1	36.4	5.5	67.3	4.5	101.2	0.1	68.6	4.5	33.9	4.4
562	103.0	0.4	101.2	0.2	33.6	6.6	69.6	3.7	101.2	0.2	67.6	5.1	35.9	5.2

Table B.9 Data for generating Figure 5.6 (a—c)

(a)	C_{aq} (µM) (NTO)													
Time (h)	AVE	STD	AVE	STD	AVE	STD	AVE	STD	AVE	STD	AVE	STD	AVE	STD
0	5.00	0.03	9.96	0.02	25.07	0.04	53.92	0.02	76.85	0.11	101.78	0.17	125.31	0.68
2	4.14	0.04	8.51	0.04	22.57	0.08	48.78	0.02	69.02	0.11	89.71	0.46	110.43	0.25
24	1.85	0.08	6.04	0.29	17.41	0.01	42.00	0.13	61.01	0.02	81.77	0.55	103.87	0.21
72	1.55	0.08	4.84	0.23	16.23	0.10	40.97	0.19	59.89	0.00	80.61	0.56	103.03	0.21
120	1.22	0.10	3.90	0.15	15.14	0.13	39.85	0.13	58.57	0.08	79.44	0.65	102.05	0.22
240	0.80	0.08	2.10	0.13	12.58	1.19	35.38	0.42	52.16	0.11	74.63	0.86	98.05	0.31
336	0.76	0.04	2.15	0.12	12.56	1.28	35.27	0.02	50.37	2.01	75.11	0.70	98.43	0.34

(b)	C_{aq} (µM) (NQ)													
Time (h)	AVE	STD	AVE	STD	AVE	STD	AVE	STD	AVE	STD	AVE	STD	AVE	STD
0	21.61	0.09	42.80	0.29	62.60	0.41	83.93	0.14	127.54	0.03	168.47	0.11	254.73	0.52
2	4.80	0.03	12.46	0.00	21.13	0.01	32.38	0.06	56.74	0.42	84.17	0.66	143.67	1.09
6	4.38	0.00	11.40	0.01	19.89	0.29	29.17	1.20	54.53	0.77	80.47	0.35	138.60	1.25
24	4.05	0.43	9.65	0.01	17.24	0.31	27.31	0.16	47.76	0.66	72.88	0.69	129.29	1.04
72	3.20	0.03	8.56	0.00	15.50	0.26	24.70	0.18	45.30	0.40	68.65	0.42	122.71	0.98
168	2.96	0.03	8.02	0.02	14.76	0.16	23.48	0.09	43.51	0.24	67.41	0.53	119.90	0.89

(c)	C_{aq} (µM) (DNAN)													
Time (h)	AVE	STD	AVE	STD	AVE	STD	AVE	STD	AVE	STD	AVE	STD	AVE	STD
0	27.21	1.95	48.41	4.11	101.21	6.02	162.04	4.73	190.49	0.00	232.55	5.27	304.80	3.71
3	0.14	0.20	0.14	0.05	7.18	2.03	32.38	2.83	73.85	5.98	107.66	16.41	196.38	1.69
9	0.00	0.00	0.09	0.13	4.94	1.55	25.59	2.11	67.78	4.68	89.32	0.00	188.68	0.43
25	0.00	0.00	0.06	0.08	2.60	0.77	19.83	2.22	61.01	6.33	87.14	8.90	176.13	0.32
80	0.00	0.00	0.00	0.00	1.27	0.60	13.32	1.41	51.27	5.68	83.49	14.35	167.45	1.16
176	0.00	0.00	0.00	0.00	0.70	0.24	9.14	0.88	43.66	6.14	65.75	0.46	146.66	6.03
320	0.00	0.00	0.00	0.00	0.60	0.23	7.13	0.84	39.68	5.58	61.52	0.11	141.46	6.04

Table B.10   Data for generating Figure 5.6(d)

(d)	C_{aq} (µM) (RDX)												
Time (h)	AVE	STD	AVE	STD	AVE	STD	AVE	STD	AVE	STD	AVE	STD	AVE	STD
0	4.92	0.00	10.00	0.00	25.00	0.00	50.00	0.00	75.00	0.00	100.00	0.00	125.00	0.00
2	0.77	0.13	3.89	0.29	15.30	0.76	39.94	0.78	63.58	0.05	88.36	2.03	110.58	0.32
24	0.54	0.00	2.82	0.38	12.80	0.36	35.33	0.35	59.41	0.64	86.81	2.89	107.67	0.50
72	0.43	0.08	2.01	0.46	11.61	0.25	33.65	0.98	57.88	0.08	81.63	1.90	106.79	0.55
120	0.45	0.09	1.85	0.33	11.08	0.12	33.27	0.79	57.67	0.49	81.23	1.62	106.56	0.78
150	0.43	0.09	1.84	0.27	10.82	0.15	32.89	1.02	57.07	0.62	80.61	2.07	105.87	0.28

Table B.11 Data for generating Figure 5.7

(a) NTO				(b) NQ			
C_{aq} (μM)		C_s (μmol/g)		C_{aq} (μM)		C_s (μmol/g)	
AVE	STD	AVE	STD	AVE	STD	AVE	STD
0.76	0.04	20.82	0.37	2.96	0.03	41.77	0.14
2.15	0.12	38.11	0.69	8.02	0.02	77.85	0.63
12.56	1.28	61.25	5.96	14.76	0.16	107.07	1.29
35.27	0.02	91.31	0.02	23.48	0.09	135.28	0.52
50.37	2.01	129.38	8.99	43.51	0.24	188.01	0.59
75.11	0.70	131.03	2.63	67.41	0.53	226.12	1.43
98.43	0.34	132.32	1.70	119.90	0.89	301.61	0.83
(c) DNAN				(d) RDX			
C_{aq} (μM)		C_s (μmol/g)		C_{aq} (μM)		C_s (μmol/g)	
AVE	STD	AVE	STD	AVE	STD	AVE	STD
0.00	0.00	80.52	5.75	0.43	0.09	50.32	1.26
0.00	0.00	143.28	12.14	1.84	0.27	91.32	3.01
0.60	0.23	297.25	16.98	10.82	0.15	158.63	1.68
7.13	0.84	455.94	11.29	32.89	1.02	191.33	11.31
39.68	5.58	442.42	16.54	57.07	0.62	200.60	6.77
61.52	0.11	501.23	13.74	80.61	2.07	216.79	22.81
141.46	6.04	476.77	8.19	105.87	0.28	214.12	3.10

Table B.12   Data for generating Figure 5.8

(a)	C_{aq} (µM) (HMX)											
Time (h)	AVE	STD	AVE	STD	AVE	STD	AVE	STD	AVE	STD	AVE	STD
0	0.38	0.02	0.95	0.00	1.96	0.04	3.03	0.00	4.41	0.00	5.54	0.00
2	0.06	0.01	0.26	0.01	1.00	0.03	1.81	0.05	2.61	0.06	3.49	0.03
24	0.00	0.00	0.19	0.00	0.77	0.00	1.54	0.08	2.49	0.15	3.21	0.03
72	0.00	0.00	0.16	0.01	0.67	0.00	1.43	0.07	2.19	0.02	3.12	0.05
120	0.02	0.02	0.15	0.02	0.64	0.01	1.37	0.05	2.16	0.02	3.09	0.05
150	0.00	0.00	0.11	0.00	0.60	0.03	1.35	0.02	2.12	0.07	3.03	0.02

(b) HMX			
C_{aq} (µM)		C_s (µmol/g)	
AVE	STD	AVE	STD
0.00	0.00	4.28	0.22
0.11	0.00	9.36	0.01
0.60	0.03	15.25	0.80
1.35	0.02	18.81	0.21
2.12	0.07	25.71	0.75
3.03	0.02	28.05	0.22

Table B.13   Data for generating Figure 5.9 (a)

Time (h)	C_{aq} (µM)															
	NTO_blank		NTO_SRB$_{OX}$		NTO_SRB$_{RED}$		ATO_SRB$_{RED}$		NTO_blank		NTO_Rogue$_{OX}$		NTO_Rogue$_{RED}$		ATO_Rogue$_{RED}$	
	AVE	STD	AVE	STD	AVE	STD	AVE	STD	AVE	STD	AVE	STD	AVE	STD	AVE	STD
0	108.1	0.1	107.8	1.3	108.7	0.3	0.0	0.0	110.8	0.1	111.2	0.0	111.2	0.0	0.0	0.0
0.3	108.4	0.6	105.3	0.1	94.3	1.5	9.5	0.8	111.2	0.0	102.3	0.4	86.0	1.6	11.3	2.4
1	108.7	0.1	104.6	0.2	90.1	1.0	14.4	0.6	111.3	0.0	102.2	0.7	84.2	1.2	8.8	0.8
3	108.9	0.2	101.3	0.0	78.6	0.7	19.4	0.4	110.8	0.3	102.1	7.5	71.9	4.7	18.1	2.6
6	108.2	0.8	100.1	0.6	71.7	1.5	23.7	0.4	111.0	0.2	100.9	5.5	67.8	5.1	20.0	1.9
8	108.0	0.4	99.8	0.2	69.1	1.5	27.2	0.1	111.1	0.6	100.5	4.9	63.0	3.9	26.6	0.4
24	108.4	0.2	99.2	0.2	59.3	1.7	35.4	1.5	110.8	0.8	100.3	5.2	59.4	3.4	29.9	1.6
54	107.4	0.3	96.1	0.5	44.5	5.9	44.8	2.7	111.1	0.1	100.3	9.8	54.8	4.3	32.3	3.9
96	107.2	0.3	95.4	0.6	38.6	6.7	50.5	3.3	111.3	0.6	84.0	4.7	42.8	3.1	42.0	0.7
123	107.3	1.8	92.9	4.1	37.1	6.1	51.7	1.8	111.0	0.3	84.8	4.2	38.8	1.7	48.0	2.9
240	107.1	0.5	95.1	0.6	31.1	6.3	57.1	1.7	110.8	0.2	85.1	4.3	34.1	0.8	47.0	0.2
480	107.9	0.9	95.4	0.6	24.8	7.8	66.0	5.0	110.5	0.3	70.5	1.5	28.0	0.5	58.9	0.4
600	108.2	1.3	95.4	0.6	22.3	5.9	64.0	4.6	109.8	2.3	75.7	4.2	22.2	0.5	57.8	1.2

Table B.14 Data for generating Figure 5.9 (c)

	C_{aq} (μM)									
Time (h)	DNAN_blank		DNAN_Rogue$_{OX}$		DNAN_Rogue$_{RED}$		2ANAN_Rogue$_{RED}$		4ANAN_Rogue$_{RED}$	
	AVE	STD	AVE	STD	AVE	STD	AVE	STD	AVE	STD
0	408.9	1.0	408.9	0.0	0.0	0.0	0.0	0.0	0.0	0.0
0.5	405.7	0.1	255.2	2.0	0.0	0.4	0.5	0.0	0.0	0.0
1	406.5	0.1	249.5	4.2	0.0	2.9	0.7	0.1	0.0	0.0
2	407.0	1.0	243.7	2.0	0.1	5.3	1.1	0.2	0.1	0.0
4	409.7	0.3	235.6	3.9	0.2	6.3	1.8	0.3	0.2	0.0
8	412.6	2.8	225.7	3.8	0.3	7.2	3.1	0.3	0.3	0.0
24	408.6	1.4	211.7	5.1	0.4	8.8	5.9	0.3	0.4	0.0
48	412.9	4.8	202.3	5.4	0.4	8.7	7.8	0.4	0.4	0.0
72	401.3	0.0	196.8	6.3	0.5	9.2	8.6	0.4	0.5	0.0
120	408.7	0.7	190.2	6.0	0.5	9.9	9.3	0.5	0.5	0.0
192	402.2	3.5	186.1	6.9	0.5	8.7	9.8	0.6	0.5	0.0
264	410.4	0.8	180.9	6.4	0.5	9.2	10.3	0.7	0.5	0.1
360	404.9	0.0	175.7	4.9	0.5	9.2	10.5	1.0	0.5	0.1
384	405.1	1.6	176.6	3.6	0.6	10.7	10.8	1.2	0.6	0.0

Table B.15   Data for generating Figure 5.9 (e)

Time (h)	C_{aq} (μM)							
	RDX_Rogue$_{OX}$		RDX_Rogue$_{RED}$		NO$_2^-$_Rogue$_{RED}$		MNX_Rogue$_{RED}$	
	AVE	STD	AVE	STD	AVE	STD	AVE	STD
0	200.8	10.6	192.9	11.4	0.0			
0.3	130.7	2.2	111.6	7.5	0.4	0.2		
1	119.7	2.5	98.0	6.9	0.7	0.2		
2	118.2	2.8	92.9	5.9	1.0	0.3		
6	116.0	2.4	91.2	5.8	1.5	0.6		
17	110.4	2.3	84.6	4.6	2.9	0.2		
28	106.6	2.4	80.5	4.9	3.3	0.2		
52	104.2	2.2	73.8	3.7	4.0	0.0	0.2	0.0
124	99.2	1.3	56.0	3.2	4.0	0.5	0.5	0.1
252	94.5	1.2	38.3	2.5	4.0	1.1	0.6	0.0
388	94.5	1.2	37.9	2.3	4.1	3.1	0.7	0.1

Table B.16   Data for generating Figure A.7(a)

Time (h)	C_{aq} (μM)			
	HMX_Rogue$_{OX}$		HMX_Rogue$_{RED}$	
	AVE	STD	AVE	STD
0	5.9	0.3	5.7	0.4
0.3	1.8	0.0	1.4	0.1
1	1.4	0.0	1.0	0.1
2	1.4	0.0	0.9	0.1
6	1.4	0.0	0.9	0.1
17	1.3	0.0	0.8	0.1
28	1.2	0.0	0.8	0.1
52	1.2	0.0	0.7	0.0
124	1.1	0.0	0.6	0.0
252	1.0	0.0	0.6	0.0
388	1.0	0.0	0.4	0.0

Table B.17   Data for generating Figure A.8

(a)	C_{aq} (µM) (NQ)							
Time (h)	Blank, inside		Blank, outside		SRB$_{OX}$, inside		SRB$_{OX}$, outside	
	AVE	STD	AVE	STD	AVE	STD	AVE	STD
0	198.4	0.4	197.7	0.3	198.4	0.5	197.7	0.2
0.2	198.2	0.2	198.0	0.2	178.4	0.3	177.1	0.1
1	198.3	0.1	198.1	0.2	169.6	0.2	168.0	0.1
5	198.1	0.1	198.0	0.1	160.3	0.8	157.3	0.2
10	197.8	0.5	198.0	0.2	154.4	0.3	150.2	0.3
25	198.4	0.1	198.1	0.2	146.7	0.6	141.5	0.4
50	195.9	1.9	197.7	0.2	141.7	0.6	136.1	0.6
120	197.6	0.1	197.7	0.1	136.1	0.4	128.6	0.7
192	197.5	0.0	197.9	0.2	130.5	0.4	125.8	0.4
(b)	C_{aq} (µM) (NQ)							
Time (h)	pH 6		pH 8					
	AVE	STD	AVE	STD				
0	99.6	0.4	99.6	0.4				
2.0	60.4	0.2	73.2	0.2				
5	56.5	0.1	65.3	0.1				
9.5	53.0	0.1	60.0	0.1				
24.5	50.5	0.5	54.8	0.5				
82.5	48.3	0.1	51.7	0.1				
120.5	47.4	1.9	48.6	1.9				
515	49.9	0.1	49.9	0.1				

Table B.18   Data for generating Figure A.9

(a)	C_{aq} (μM) (NQ)												
Time (h)	AVE	STD	AVE	STD	AVE	STD	AVE	STD	AVE	STD	AVE	STD	AVE	STD
0	25.00	0.00	50.00	0.00	75.00	0.00	100.00	0.00	125.00	0.00	150.00	0.00	175.00	0.00
0.2	19.34	0.09	38.62	1.85	63.23	2.05	89.35	1.34	109.14	2.74	130.70	2.22	156.87	0.58
1	18.04	0.10	36.46	1.75	59.69	2.59	84.20	2.73	105.11	1.41	125.66	2.88	151.73	0.48
5	15.68	0.33	31.00	1.00	52.27	3.13	76.05	1.37	96.07	0.88	115.45	1.22	143.50	1.80
10	13.42	0.16	27.54	0.99	47.88	2.30	69.42	2.18	91.22	2.31	109.00	2.21	134.82	4.18
25	10.45	0.54	22.43	1.05	40.63	3.00	61.76	2.19	82.06	0.22	99.61	2.31	124.47	2.34
50	7.86	0.24	19.08	0.00	35.87	0.00	56.73	2.03	75.88	0.61	92.82	2.83	116.60	2.21
120	6.07	0.20	15.78	0.75	30.64	1.08	51.61	2.00	69.70	0.96	85.54	2.42	108.54	1.77
192	5.36	0.19	14.47	0.67	28.42	0.68	49.33	1.93	66.95	1.00	81.97	2.99	104.96	1.09

(b) NQ_SRB			
C_{aq} (μM)		C_s (μmol/g)	
AVE	STD	AVE	STD
5.36	0.19	23.11	0.22
14.47	0.67	41.86	0.82
28.42	0.68	54.78	0.88
49.33	1.93	59.59	2.31
66.95	1.00	68.30	1.20
81.97	2.99	80.05	3.54
104.96	1.09	82.35	1.32

Table B.19   Data for generating Figure A.10

Time (h)	C_{aq} (μM) (NQ)			
	SRB_{OX}		SRB_{RED}	
	AVE	STD	AVE	STD
0	100.1	0.1	99.6	0.3
2.0	75.5	0.2	73.2	0.2
5	67.9	0.3	65.3	0.2
9.5	62.0	0.4	60.0	0.1
24.5	55.9	0.6	54.8	0.2
82.5	48.0	0.7	51.7	0.2
120.5	47.1	0.4	48.6	0.2
515	46.7	0.1	49.9	0.1

Appendix C

LIST OF PUBLICATIONS AND PRESENTATIONS FROM THE DISSERTATION

C.1   Publication List

Chapter 2:

Xin, D., Xian, M., Chiu[*], P. C., New methods for assessing electron storage capacity and redox reversibility of biochar, Chemosphere, 2019, 215(01): 827-834. https://doi.org/10.1016/j.chemosphere.2018.10.080

Chapter 3:

Xin, D., Barkley, T. and Chiu[*], P. C., Visualizing electron storage capacity distribution in biochar through silver tagging, *Chemosphere*, 2020, 248, 125952. https://doi.org/10.1016/j.chemosphere.2020.125952

Chapter 4:

Xin, D., Nepu, S., Reza, M. T., Hudson, J., Chiu[*], P. C., Pyrolysis creates electron storage capacity of black carbon (biochar) from lignocellulosic biomass*, ACS Sustainable Chemistry & Engineering*, 2021, 9(19), 6821-6831. https://doi.org/10.1021/acssuschemeng.1c01251

Chapter 5:

Xin, D., Girón, J., Fuller, M. E., Chiu[*], P. C., Abiotic reduction of 3-nitro-1,2,4-triazol-5-one (NTO) and other munitions constituents by wood-derived biochar through its electron storage capacity. For submission to the *Environmental Science: Processes & Impacts*.

Other publications from this dissertation:

Xin, D., Xian, M., Chiu[*], P. C., Chemical methods for determining the electron storage capacity of black carbon, MethodsX, 2018, 5: 1515-1520. https://doi.org/10.1016/j.mex.2018.11.007

Xin, D. and Chiu[*], P. C., Visualizing the distribution of black carbon's electron storage capacity using silver, *MethodsX*, 2020, 7, 100838. https://doi.org/10.1016/j.mex.2020.100838

Nepu, S., Xin, D., Chiu, P. C., Reza[*], M. T., Effect of pyrolysis temperature on acidic oxygen-containing functional groups and electron storage capacities of pyrolyzed hydrochars, *ACS Sustainable Chemistry & Engineering*, 2019, 7(09): 8387-8396. https://doi.org/10.1021/acssuschemeng.9b00024

C.2   Presentation List

1. April 2021 *Spring 2021 ACS National Meeting*, Oral Presentation (virtual), "Reductive transformation of 3-nitro-1,2,4-triazole-5-one (NTO) by biochar through its electron storage capacity (ESC)".

2. April 2021 *Spring 2021 ACS National Meeting*, Poster Presentation (virtual), "Comparison of mediated electrochemical analysis and chemical redox titration for measuring the electron storage capacity of biochar".

3. December 2020, *SERDP and ESTCP Symposium 2020*, Poster Presentation (virtual), "Sorption and reductive degradation of munitions constituents by biochar".

4. March 2020, *Spring 2020 ACS National Meeting*, ACS SciMeeting (virtual), "Quantifying and visualizing the spatial distribution of black carbon's electron storage capacity". https://doi.org/10.1021/scimeetings.0c03420.

5. August 2019, *Fall 2019 ACS National Meeting*, San Diego, CA, Oral Presentation, "Biochar as a nanosilver support medium for water disinfection".

6. August 2019, *Fall 2019 ACS National Meeting*, San Diego, CA, Oral Presentation, "Assessing the reversibility of electron storage capacity of biochar by chemical methods".

7. June 2019, *Human and Climate Series III: Water Management and Policy*, Dover, DE, Poster Presentation, "Chemical methods for determining the electron storage capacity of black carbon (biochar)".

8. August 2018, *US Biochar Initiative (USBI) Biochar 2018*, Wilmington, DE, Oral Presentation, "Electron storage capacities (ESC) of biochar and other black carbon materials".

9. July 2018, *CONSERVE Annual Meeting*, College Park, MD, Poster Presentation, "Biochar as a silver nanoparticle support for irrigation water treatment".

Appendix D

PERMISSIONS FROM THE PUBLISHERS

Chapter 2 is an adapted and combined version of articles published in Chemosphere by Elsevier and ACS Sustainable Chemistry & Engineering by the American Chemical Society (ACS). Chapter 3 is a reprinted version of an article published also in Chemosphere by Elsevier. Chapter 4 is a shortened version of an article published in ACS Sustainable Chemistry & Engineering by ACS.

According to the copyright policies of Elsevier, the authors can include their articles in a dissertation (provided this is not published commercially). For further information on the copyright policies of Elsevier, please see the link: https://www.elsevier.com/about/policies/copyright

According to ACS's Policy on Theses and Dissertation, the authors may reuse all or part of the Published Work in a dissertation that the author writes and is required to satisfy to submit to satisfy the criteria of degree-granting institutions, with appropriate citation of the Published Work. The permission of the article used in Chapters 2 and 4 is obtained through the RightsLink permission system and shown below.

Pyrolysis Creates Electron Storage Capacity of Black Carbon (Biochar) from Lignocellulosic Biomass

ACS Publications
Most Trusted. Most Cited. Most Read.

Author: Danhui Xin, Nepu Saha, M. Toufiq Reza, et al

Publication: ACS Sustainable Chemistry & Engineering

Publisher: American Chemical Society

Date: May 1, 2021

Copyright © 2021, American Chemical Society

PERMISSION/LICENSE IS GRANTED FOR YOUR ORDER AT NO CHARGE

This type of permission/license, instead of the standard Terms and Conditions, is sent to you because no fee is being charged for your order. Please note the following:

- Permission is granted for your request in both print and electronic formats, and translations.
- If figures and/or tables were requested, they may be adapted or used in part.
- Please print this page for your records and send a copy of it to your publisher/graduate school.
- Appropriate credit for the requested material should be given as follows: "Reprinted (adapted) with permission from {COMPLETE REFERENCE CITATION}. Copyright {YEAR} American Chemical Society." Insert appropriate information in place of the capitalized words.
- One-time permission is granted only for the use specified in your RightsLink request. No additional uses are granted (such as derivative works or other editions). For any uses, please submit a new request.

If credit is given to another source for the material you requested from RightsLink, permission must be obtained from that source.

BACK   CLOSE WINDOW